

# **Directed Nanoparticle Organization via Chemically Selective Microcontact Printing**

**THÈSE N° 2747 (2003)**

PRÉSENTÉE au DÉPARTEMENT de SCIENCE de BASE

**ÉCOLE POLYTECHNIQUE FÉDÉRALE DE LAUSANNE**

POUR L'OBTENTION DU GRADE DE DOCTEUR ÈS SCIENCES

**PAR**

**Xiaochun WU**

Scientifique diplômé de l'Université de Jilin, Chine  
de nationalité Chinoise

acceptée sur proposition du jury:

Prof. K. Kern, directeur de thèse

Dr. A. Bietsch, corapporteur

Prof. K. Severin, corapporteur

Prof. M. Textor, corapporteur

Lausanne, EPFL

2003



## Abstract

In this thesis, the strategy of assembling nanoparticles at surfaces in a patterned way using a simple, general and mild method is addressed. This is realized using the combination of microcontact printing ( $\mu$ CP) and wet chemical synthesis. Poly(amidoamine) (PAMAM) dendrimers are used both for the stabilization of nanoparticles and for their binding on the surface. The thesis can be divided into two parts: printing of pure dendrimers on the surface and direct synthesis of nanoparticles on the printed dendrimer parts (part I) and direct printing of dendrimer-stabilized nanoparticles that are synthesized from solution (part II).

OH-terminated generation 4 PAMAM dendrimers (here referred as G4OH) have been shown to be good nanotemplates for the synthesis of some transition metal nanoparticles (Cu, Pd, Pt). For these metals, nanoparticles are formed inside the G4OH (internal type). They can be considered as a model system. In addition, G4OH can form layers on OH-terminated surfaces via hydrogen bonds. Therefore, in part I, the capability of G4OH dendrimers as inks is explored. They are proven to be good inks down to sub-micrometer sizes on Si wafers. After the optimization of printing conditions,  $\text{Pd}^{2+}$  ions are bound to internal tertiary nitrogen of printed G4OH dendrimers via strong complexation upon solution adsorption. After reduction, Pd nanoparticles are formed. They are catalytically active and can guide the electroless deposition (ELD) of cobalt on the printed regions. Dimension of cobalt patterns down to several-hundred-nanometer line width can be produced.

In Part I, G4OH molecules are first printed on the surface; metal ions are then bound to them. This means that the morphology of the printed dendrimers will influence

the growth of metal nanoparticles in a subsequent reduction step. The morphology of printed dendrimers is much more difficult to control than their morphology in solution. The size distribution of metal nanoparticles from the former is therefore larger than that from solution synthesis. This might not influence ELD processes much since the size distribution does not play a critical role in this process. But it may play a very important role in other processes. For example, photoluminescence (PL) from semiconductor nanoparticles is highly sensitive to the size distribution. Large size distribution implies a low degree of color purity.

Is it possible to directly print dendrimer-stabilized nanoparticles that are synthesized in solution with good control of experimental conditions? Considering that the printing procedures of “internal type” nanocomposites should be similar to printing dendrimers themselves, we explore another possibility in part II: printing nanoparticles that are located at the surface of dendrimers (external type). This should also allow patterning of other nanoparticles. For example, metal and semiconductor nanoparticles with high quality have been synthesized using other stabilizers. Binding nanoparticles to the surfaces of dendrimers can be achieved via ligand exchange of these stabilizers with dendrimers. These nanoparticles then can be printed to the surface using the chemical properties of the dendrimers.

NH<sub>2</sub>-terminated generation 8 PAMAM dendrimers (G8NH<sub>2</sub>) are selected based on the following two considerations: (1) NH<sub>2</sub> groups can supply binding sites for metal ions and guide the formation of nanoparticles on the surface of the dendrimer. In addition, NH<sub>2</sub>-terminated linear chain molecules have been used to passivate the surface of II-VI semiconductor nanoparticles. (2) G8NH<sub>2</sub> dendrimers can form layers on quite a lot of

different surfaces via hydrogen bonds, multidentate metal-ligand interactions, electrostatic forces, or covalently bind to the surface via a simple amidation reaction. Therefore, in part II, we first synthesize CdS nanoparticles in solution using G8NH<sub>2</sub> as stabilizers. Host-guest interactions between primary nitrogen and Cd<sup>2+</sup> ions are explored. Preparation parameters, particle growth behavior and PL mechanism are studied. After that, CdS/G8NH<sub>2</sub> nanocomposites are used as inks and directly printed on various surfaces. The effects of printing conditions are discussed. The successful printing of “external type” nanocomposites points to a simple, general, and mild way to produce patterns made up from nanoparticles.

## Zusammenfassung

Thema dieser Arbeit ist das gezielte Anbinden von Nanopartikeln auf Oberflächen in vordefinierten Mustern mit einer einfachen, generell anwendbaren und chemisch milden Methode. Dies wurde durch die Kombination von Mikrokontaktdruck (microcontact printing,  $\mu$ CP) und nasschemischen Synthesen erreicht. Poly(amidoamin)- (PAMAM) Dendrimere dienten dabei sowohl zur Stabilisierung der Nanopartikel als auch zum Binden derselben an die Oberfläche. Die Arbeit teilt sich in zwei Bereiche: Druck reiner Dendrimere auf die Oberfläche, gefolgt von Synthese von Nanopartikeln auf den Dendrimer-bedruckten Flächen (Teil I) und direkter Druck von Dendrimer-stabilisierten Nanopartikeln, die in Lösung synthetisiert wurden (Teil II).

Es wurde gezeigt, dass OH-terminierte PAMAM-Dendrimere der Generation 4 (hier G4OH genannt) gute Nanotemplate für die Synthese einiger Übergangsmetall-Nanopartikel (Cu, Pd, Pt) sind. Nanopartikel dieser Metalle bilden sich im Innern des G4OH ("innen-Typ"). Sie können als Modellsystem fungieren. Zusätzlich kann G4OH mittels Wasserstoffbrücken Schichten auf OH-terminierten Oberflächen bilden. Davon ausgehend beschreibt Teil I, wie man G4OH-Dendrimere als "Drucktinte" für  $\mu$ CP benutzen kann. Es wird gezeigt, dass sie tatsächlich bis zum Submikrometer-Bereich auf Siliziumwafern gute "Tinten" sind. Nach dem Optimieren des Druckprozesses wurden  $\text{Pd}^{2+}$ -Ionen aus der Lösung an innere tertiäre Stickstoffatome des gedruckten G4OH gebunden, wobei sich stabile Komplexe bildeten. Die nach Reduktion erhaltenen Pd Nanopartikel waren katalytisch aktiv und konnten die stromlose Abscheidung (electroless deposition, ELD) von Kobalt gezielt auf die bedruckten Flächen steuern.

Kobaltstrukturen bis in den Bereich von einigen hundert Nanometern Linienbreite konnten erzeugt werden.

Teil I zeigt, wie zunächst G4OH-Moleküle auf die Oberfläche gedruckt wurden; Metallionen wurden dann an sie gebunden. Dies bedeutet, dass die Morphologie der gedruckten Dendrimere das Wachstum von metallischen Nanopartikeln im darauf folgenden Reduktionsschritt beeinflusst. Die Morphologie gedruckter Dendrimere ist allerdings viel schwieriger zu kontrollieren als die Morphologie in Lösung. Die Grössenverteilung der metallischen Nanopartikel ist daher im ersten Fall breiter als bei Synthese in Lösung. ELD wird davon nicht stark beeinflusst, da die Grössenverteilung in diesem Prozess keine grosse Rolle spielt. In anderen Prozessen kann sie hingegen eine enorm wichtige Rolle spielen. Z.B. reagiert die Photolumineszenz (PL) von Halbleiter-Nanopartikeln hochempfindlich auf deren Grössenverteilung: Eine breite Verteilung impliziert eine geringe Farbreinheit.

Ist es möglich, Dendrimer-stabilisierte Nanopartikel direkt zu drucken, welche – unter guter Kontrolle der experimentellen Bedingungen – in Lösung synthetisiert wurden? Das Drucken der "innen-Typ"-Nanokomposite sollte analog zu dem der reinen Dendrimere verlaufen; in Teil II wird dagegen eine weitere Möglichkeit erforscht: Drucken von Nanopartikeln, die sich auf der Aussenfläche von Dendrimeren befinden ("ausser-Typ"). Dies ist auch für andere Nanopartikel denkbar. Z.B. wurden Metall- und Halbleiter-Nanopartikel hoher Qualität mit anderen Stabilisatoren synthetisiert. Diese Nanopartikel könnten durch Ligandenaustausch der Stabilisatoren an Dendrimere gebunden werden. So erzeugte Nanokomposite könnten dann auf die Oberfläche gedruckt werden, indem man die chemischen Eigenschaften der Dendrimere ausnutzt.

Hierzu wurden  $\text{NH}_2$ -terminierte PAMAM-Dendrimere der Generation 8 ( $\text{G8NH}_2$ ) gewählt, denn (1) können  $\text{NH}_2$ -Gruppen Anbindestellen für Metallionen sein und die Bildung von Nanopartikeln auf die Oberfläche des Dendrimers dirigieren. Z.B. wurden  $\text{NH}_2$ -terminierte Kettenmoleküle bereits eingesetzt, um die Oberfläche von II-VI-Halbleiter-Nanopartikeln zu passivieren. (2)  $\text{G8NH}_2$ -Dendrimere können auf einer Vielfalt von Oberflächen Schichten bilden, und zwar mittels Wasserstoffbrücken, mittels Metall-Ligand-Wechselwirkungen oder elektrostatisch; alternativ können sie durch eine einfache Amidierung kovalent an die Oberfläche binden. Teil II präsentiert zunächst die Synthese von CdS-Nanopartikeln in Lösung mit  $\text{G8NH}_2$  als Stabilisator. Wirt-Gast-Wechselwirkungen zwischen primären Stickstoffatomen und  $\text{Cd}^{2+}$  wurden untersucht, und Parameter der Synthese, Wachstumsverhalten der Partikel und PL-Mechanismen studiert. Schliesslich wurden CdS/ $\text{G8NH}_2$ -Nanokomposite als "Drucktinte" benutzt und auf verschiedene Oberflächen direkt gedruckt. Der Einfluss der Druckparameter wird diskutiert. Das erfolgreiche Drucken von Nanokompositen des "ausser-Typs" verweist auf einen einfachen, generell anwendbaren und milden Weg, Strukturen aus Nanopartikeln zu erzeugen.



# Contents

## Abstract

## Zusammenfassung

<b>1 Introduction</b>	<b>1</b>
<b>2 Background</b>	<b>7</b>
2.1 Atomic force microscope	7
2.2 Microcontact printing	17
2.3 Dendrimers	22
2.4 Design of Patterned Functionality on Surfaces	39
<b>3 Spatially Selective Electroless Deposition of Cobalt on Oxide Surfaces Directed by Microcontact Printing of Dendrimers</b>	<b>45</b>
3.1 Introduction	45
3.2 Experimental part	47
3.3 Printing of G4OH dendrimers	49
3.4 Binding of Pd <sup>2+</sup> ions and ELD of cobalt layers	56
3.5 Conclusions	60
<b>4 Synthesis, Structure and Optical Properties of CdS/ Dendrimer Nanocomposites</b>	<b>63</b>
4.1 Introduction	64
4.2 Experimental	65

4.3 Effects of $\text{Cd}^{2+}/\text{G8NH}_2$ and $\text{Cd}^{2+}/\text{S}^{2-}$ ratios on the formation of CdS nanoparticles	66
4.4 Room temperature growth of CdS/G8NH <sub>2</sub> nanocomposites	68
4.5 Effects of adding organic additives to CdS/G8NH <sub>2</sub> nanocomposites	73
4.6 Effects of adding inorganic ions and the formation of a core-shell structure	74
4.7 The mechanism of blue PL	80
4.8 The location of CdS nanoparticles and the morphology of CdS/G8NH <sub>2</sub> nanocomposites	87
4.9 Conclusions	96
<b>5 Adsorption and Patterning of CdS/dendrimer Nanocomposites on Substrates</b>	<b>99</b>
5.1 Introduction	99
5.2 Experimental	100
5.3 Effects of substrates on the morphology of CdS/G8NH <sub>2</sub> nanocomposites	102
5.4 Effects of aging on the morphology of CdS/G8NH <sub>2</sub> nanocomposites	107
5.5 $\mu\text{CP}$ of pure G8NH <sub>2</sub> host molecules	110
5.6 Effects of morphology variation of CdS/G8NH <sub>2</sub> nanocomposites on printed patterns	113
5.7 Photoluminescent patterns of CdS/G8NH <sub>2</sub> nanocomposites	118
5.8 Comparison of direct printing and indirect patterning	120
5.9 Conclusions	123
<b>6 Conclusions and outlook</b>	<b>125</b>

# Chapter 1

## Introduction

Devices that are composed of functional molecules and nanoparticles in a regular array or in a designed arbitrary pattern are a very important direction of nanoscience and nanotechnology nowadays. In this way the interactions between nano-units can be controlled with high precision. Generally, the following three ways are used to form patterned structures:

A: Lithography techniques (UV light, e-beam, ion beam, x-ray etc.) [Schmuki98] and two recently developed techniques, nanoimprinting [Chou96] and soft lithography [Xia98].

B: Patterns formed by self-assembly phenomena and guided growth of nanostructures on patterned surfaces formed by a self-organization process [Kern91, Brune98, Repain02].

C: Scanning probe based techniques [Schoer97]. Two examples are that tips scan on modified surfaces (“constructive lithography”) [Maoz99, Maoz00] and that functionalized tips scan on non-modified or modified surfaces (dip-pen technique) [Piner99].

Each of the above-mentioned methods has advantages and disadvantages. Both nanoimprinting and soft lithography are top-down methods and the minimum feature size of the pattern is limited by the final size achieved by the lithography technique and by the properties of the polymer molds. Compared with traditional lithography techniques, they have the advantages of low-cost, high-throughput (parallel patterning process) and easy handling. In contrast, method B is a bottom-up method. The problem is that the morphology of patterns formed by a self-assembly process is not easily predictable and

that the patterns are limited to certain substrates for the guided growth. For method C, the final size of patterns is determined by the size of the scanning tips and therefore can be very small (close to the molecular level). More important, compared with method B, arbitrary patterns can be realized using C. However, C is a serial patterning process and is therefore intrinsically slow. With the development of multicantilever tools, e.g. “the millipede chip“ [Vettiger00], C can achieve parallel patterning and thus work very fast.

Nanoparticles, as a kind of novel functional material, might play an important role in future technologies such as photovoltaics, switches, phosphors, LEDs, electronic data storage systems, and sensors. Therefore, parallel schemes of positioning of these nanoparticles in fixed arrays are the basis of potential photonic and electronic devices. Over two decades of developments, great progress in the synthesis of high-quality nanoparticles via wet chemistry has been made [Schmid92, Murray00]. However, the direct patterning of these nanoparticles from solution using standard patterning techniques, such as laser ablation of the material and deposition through a shadow mask, do not work well since nanoparticles are often protected by organic surfactants (stabilizers) that tend to desorb at high temperature. Because the surfactants are usually necessary to stabilize the particles and to improve the functionality of the particles, any patterning approach must be carried out at low temperatures and in a chemically mild environment. Up to now, only a few methods for the preparation of thus patterned assemblies of nanoparticles have appeared. The most-often-used mild method is based on “selective“ adsorption of nanoparticles on a patterned surface. To achieve this, either the surface of nanoparticles or the surface of the substrates has to be modified with other materials that will guarantee a strong interaction between nanoparticles and the substrate

surface. Normally, the organic surfactants that are used to control the growth of nanoparticles are not good for binding nanoparticles to the surface. Another material is often needed to displace the original surfactants and to bind nanoparticles to a surface.

Could one material fulfill these two functions? Dendrimers are highly branched, spherically shaped functional molecules [Zeng97]. They are composed of three parts, core, repetitive unit and terminal groups. The repetitive unit and terminal group can exhibit different functionalities according to requirements. For example, in OH-terminated poly(amidoamine) (PAMAM) dendrimers, interior tertiary nitrogen groups provide binding sites for metal ions, whereas the terminal OH groups supply solubility in different solvents. Due to the fixed number of binding sites (by generations), the loading of metal ions can be accurately controlled. After reduction, metal nanoclusters with the numbers corresponding to the loaded metal ions can be produced. For example,  $\text{Cu}(0)_{10}$  and  $\text{Cu}(0)_{27}$  nanoclusters inside a dendrimer were prepared by a controlled loading with  $\text{Cu}^{2+}$  ions [Balogh98]. So far, dendrimers have been used as nanoreactors for the synthesis of various nanoparticles, such as metals, semiconductors and magnetic oxides [Sooklal98, Zhao98, Zhao99a, Zhao99b, Huang99, Tan99, Strable01, Zheng02]. For this, first the corresponding metal ions have to bind to the dendrimer, and then they react with other reactants to form corresponding products. For example, metals via reduction ( $\text{M}^{n+} + ne \rightarrow \text{M}^0$ ), compounds via combination reaction ( $b\text{M}^{n+} + n\text{A}^{b-} \rightarrow \text{M}_b\text{A}_n$ ). Due to the limited binding sites provided by the dendrimer, the dimension of products is in the nanometer range. Therefore, dendrimers are nanoreactors. Nanoparticles can be synthesized inside dendrimers (internal type) [Zhao98, Zhao99a, Zhao99b], outside dendrimers (external type) [Sooklal98, Huang99, Strable01, Zheng02], or as a mixture of

both types [Tan99, Torigoe01]. Which type is formed is controlled by the size and shape of the dendrimers, by the loading factor of the metal ions in dendrimers, and by interactions between metal ions and dendrimers. Therefore, similar to surfactants, dendrimers can be also used as stabilizers for nanoparticles. More important, through the control of terminal groups, dendrimers can form layers on various surfaces via electrostatic forces, hydrogen bonds, van der Waals interactions, multidentate metal-ligand interactions, or covalent bonds [Tsukruk97, Lackowski99, Zhang02, Fail02]. This makes the immobilization of dendrimers or nanoparticle/dendrimer composites on surfaces quite simple. Therefore, dendrimers themselves can act both as stabilizers for the synthesis of nanoparticles and as media for their immobilization on the surface.

We want to address the following question: Apart from solution adsorption, can nanoparticles be patterned on substrates using other simple, general and mild methods? As a patterning method, the microcontact printing technique ( $\mu$ CP, one type of soft lithography) has become quite popular due to its rapidity, simplicity, cheapness and the capability of high spatial resolution down to several hundred nanometers [Kind99, Kind00a, Gu01]. In addition, it is a mild method. In contrast to nanoimprinting, where patterns are formed in a polymer surface,  $\mu$ CP can be done on a variety of surfaces. This provides a possibility for manifold chemical modifications of the surface. Therefore it is selected here as the patterning method. For the  $\mu$ CP technique, we need a suitable ink. Due to the above-mentioned features of dendrimers, they are potential good inks. Thus bringing dendrimer-stabilized nanoparticles on surfaces would be simple in principle. In this work, we explore this feasibility. Various substrates such as OH-terminated surfaces (Si wafer, glass, etc.), Au and self assembled monolayer (SAM)-modified Au are used.

Host-guest interactions are explored to bind the functional nanoparticles. Guests are metal and semiconductor nanoparticles while hosts are dendrimers with different terminal groups and generations. The synthesis of nanoparticles is achieved with wet chemistry. Routine characterization techniques include atomic force microscopy (AFM), scanning tunneling microscopy (STM), ellipsometry, contact angle measurement, UV/visible absorption spectroscopy, and photoluminescence (PL) spectroscopy.

Chapter 2 describes background knowledge: principle and operation of AFM for topographic imaging, principle and development of the microcontact printing technique, structure and functionality of dendrimers, and the design of patterned functionality on surfaces.

In chapter 3, we use OH-terminated PAMAM dendrimers as inks and print them on OH-terminated Si surfaces. Pd<sup>2+</sup> ions are then specifically bound to the dendrimer pattern. After reduction, Pd nanoparticles form and can catalyze the formation of cobalt patterns on the printed regions. Dimensions down to several hundred nanometers are achieved. It is found that the ink concentration is a vital factor in guaranteeing the reproduction of the master pattern feature size and that the amount of Pd<sup>2+</sup> ions bound to dendrimers is a crucial element for the good quality of cobalt patterns.

In chapter 4, we concentrate on the solution synthesis of CdS nanoparticles using NH<sub>2</sub>- terminated PAMAM generation 8 dendrimers (G8NH<sub>2</sub>) as nanoreactors. Growth behavior of CdS nanoparticles is analyzed. The effects of various additives on the PL of nanoparticles are investigated. The PL mechanism is analyzed according to the energy level structure and with the help from PL decay measurements. The morphology of nanocomposites and its control are also discussed.

After the optimization of synthesis and of the properties of CdS/G8NH<sub>2</sub> nanocomposites in chapter 4, we use these nanocomposites as inks and print them on surfaces, as presented in chapter 5. First, we study the morphology of nanocomposites, prepared via solution adsorption, on various surfaces. The variation of morphology upon room temperature aging is then investigated using AFM. This change in the morphology of nanocomposites has a large effect on the obtained patterns when they are printed to the surfaces. Finally, direct printing of nanocomposites is compared with indirect patterning (combination of printing passivation SAMs and solution adsorption of nanocomposites).



## Chapter 2

### Background

#### **2.1 Atomic force microscope**

The atomic force microscope (AFM, one type of scanning probe microscopes) was invented by Binnig, Quate and Gerber in 1986 [Binnig86]. After nearly two decades of developments, it has become a routine characterization method for surfaces. It can provide many different properties of materials such as friction, adhesion, elastic modulus, and composition [Takano99]. Throughout this work, AFM is used as a main characterization technique for surface topography. Therefore a simple introduction of AFM principles and operations related to surface topographic imaging is given.

##### **2.1.1 Vertical forces between the cantilever and the surface of the sample**

In AFM, a very sharp tip, which is attached to a cantilever, is brought close to or in contact with the surface. While the tip is scanning the sample (or vice versa), the cantilever bends due to the interactions between the tip and the sample. The bending in vertical direction is used to generate topographic images of a sample surface. Fig. 2.1 (upper part) shows vertical forces acting on the cantilever. Attractive van der Waals forces between the tip and the sample pull the cantilever toward the surface while repulsive van der Waals forces between them deflect the cantilever away from the

surface. Capillary forces exerted on the tip by liquid layers on the sample surface pull the cantilever toward the surface. The total net force on cantilever is the sum of all the forces acting on the cantilever. Cantilever deflection away from the surface is the result of a net positive force on the cantilever ( $F_v > F_c$ ). Cantilever deflection toward the surface is the result of a net negative force on the cantilever ( $F_v < F_c$ ). The effects of positive and negative net forces on the cantilever bending are shown in the lower part of Fig. 2.1.

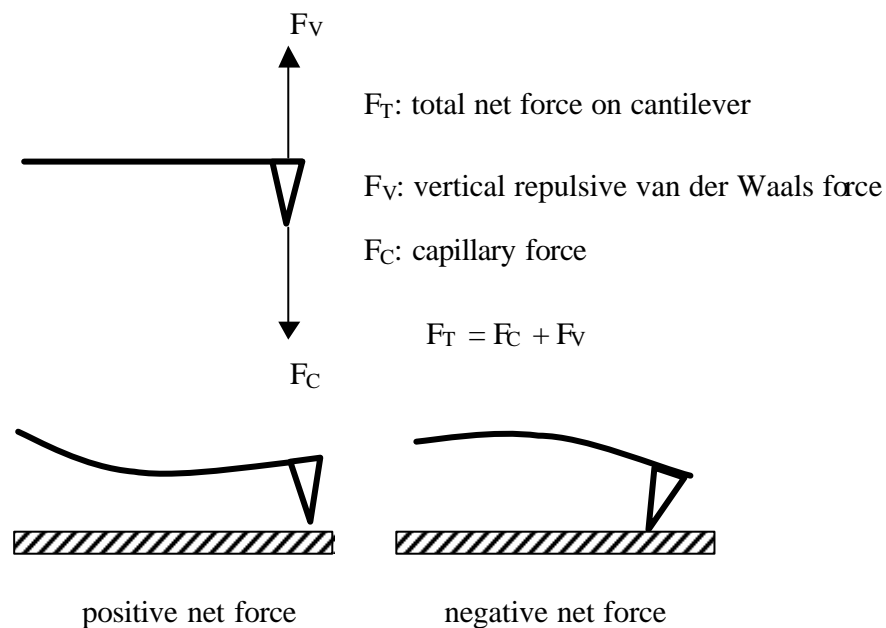


Figure 2.1 (upper part) Vertical forces acting on the cantilever.

Figure 2.1 (lower part) Bending of the cantilever under positive (negative) net force.

Fig. 2.2 shows an interatomic force vs. distance curve, which illustrates the force between atoms on a cantilever tip and atoms on a sample surface vs. the separation distance between the tip and the sample. It is similar to the Lennard-Jones curve of the potential energy between atoms as a function of distance. Two distance regimes are

labeled in the figure: 1) the contact regime, less than a few tenths of a nanometer, which represents the tip-to-sample spacing for the contact AFM, where the total net force on the cantilever is positive; and 2) the non-contact (NC) regime, ranging from a few nanometers to tens of nm, which represents the tip-to-sample spacing for NC-AFM, where the total net force on the cantilever is negative.

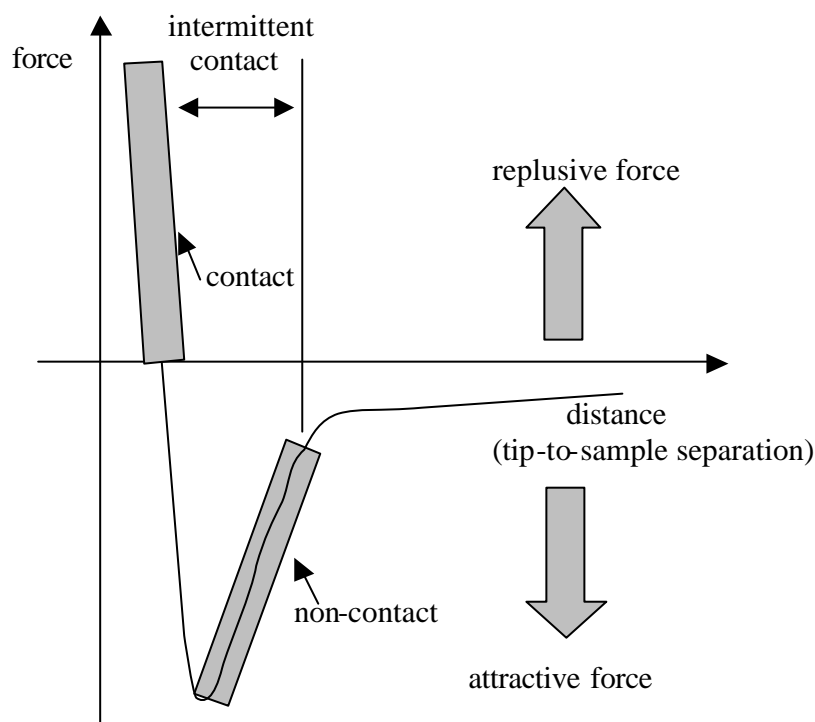


Figure 2.2 An interatomic force vs. distance curve

### 2.1.2 Contact AFM operation for surface topography

In contact mode AFM, a tip with a typical spring constant of  $1.0 - 0.1 \text{ N/m}$  is brought into contact with the surface. Contact AFM can operate in two modes: constant-height and constant-force mode. In constant-height mode, the spatial variation of the

cantilever deflection is used directly to generate the topographic data set (Fig. 2.3 left). In constant-force mode, a feedback loop operates to maintain a constant deflection of the cantilever by adjusting the probe height. A graphic representation of the adjustment of the tip height ( $z$ ) yields the surface topography of the sample (Fig. 2.3 right).

In contact AFM the magnitude of the total force exerted on the sample varies from  $10^9$  N to  $10^6$  N. This force range is often incompatible with soft or elastic samples. NC-AFM is desirable because the total force between the tip and the sample is very low, generally about  $10^{12}$  N. Therefore it provides a means for measuring sample topography with little or no contact between the tip and the sample. This is advantageous for soft materials.

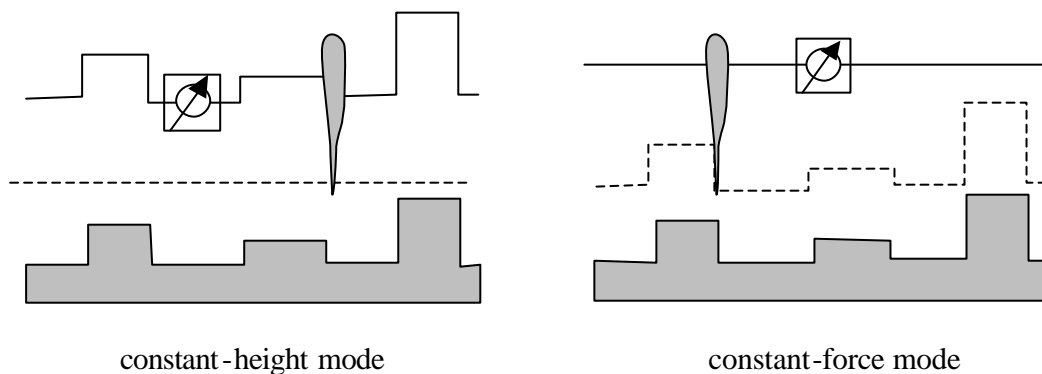


Figure 2.3 Comparison of constant-height (left) and constant-force mode (right). Dashed lines represent paths of tips while solid lines are cantilever deflections.

### 2.1.3 Principle of NC and intermittent contact (IC) AFM operation

In NC mode, the system vibrates a stiff cantilever near its resonant frequency (typically from 100 to 400 kHz) with amplitude of a few to tens of nm. The resonant frequency of a cantilever is related to its effective spring constant and its mass ( $\omega = (k_{\text{eff}} /$

$m)^{1/2}$ ).  $k_{\text{eff}}$  changes when the force between the tip and the sample has a spatial gradient ( $k_{\text{eff}} = k - f$ ), as it does in the non-contact regime.  $k$  is spring constant in free space.  $f$  is the force gradient. If the cantilever moves into a tip-to-sample spacing regime where the force gradient is positive and increasing, then  $k_{\text{eff}}$ , and therefore  $\omega$ , decreases. In the non-contact tip-to-sample regime the force gradient is positive, and it increases as the tip-to-sample spacing decreases. Thus, when an oscillating cantilever is brought near a sample surface, the force gradient experienced by the cantilever increases, and its resonance frequency decreases (see horizontal arrow in Fig. 2.4). The thick curve is the original response curve when the tip is far away from the sample surface while the thin curve is the response curve when the tip approaches the sample surface. If the resonance frequency of a cantilever shifts, the amplitude of the cantilever vibration at a given frequency changes. Near the cantilever's resonance frequency, this change is large.

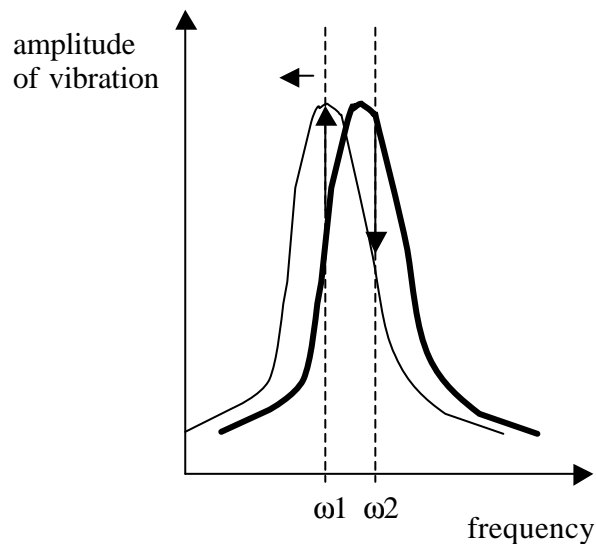


Figure 2.4 Vibration amplitude vs. frequency response for NC and IC modes.

In NC-AFM mode, a drive frequency ( $\omega_2$ ) close to, but greater than, the free-space resonance frequency of the cantilever is selected so that the vibration amplitude decreases significantly (see vertical arrow at  $\omega_2$ ) as the cantilever is brought closer to the sample surface. These amplitude changes reflect the change in the force gradient acting on the cantilever, which in turn reflects changes in the tip-to-sample spacing. A feedback mechanism operates to maintain constant cantilever vibration amplitude by adjusting and restoring the tip-to-sample spacing during a scan. The amount of scanner z movement necessary to maintain a constant force gradient is used to generate an image of the topography. For the IC-AFM mode, the cantilever is driven at a fixed frequency ( $\omega_1$ ) close to, but less than, its free-space resonance frequency. Because the drive frequency is just below the free-space frequency the vibration amplitude of the cantilever increases (see vertical arrow at  $\omega_1$ ) as the cantilever is brought closer to the sample surface, and intermittent contact is consequently achieved. In this case the tip touches the surface with the frequency of  $\omega_1$ .

### **2.1.3 Hardware components for topographic imaging**

The primary components labeled in Fig. 2.5 include piezoelectric scanner (xy scanner and z scanner), deflection sensor, cantilever and piezoelectric actuator, sine wave generator, lock-in amplifier, differential amplifier and z feedback loop and sample. Signal pathways are as follows: A sine wave generator sends an AC voltage signal, which drives the cantilever (via a piezoelectric transducer) to oscillate with a constant frequency. The AC signal is also input to the lock-in amplifier to provide the reference signal for lock-in detection. Motions of the oscillating cantilever are measured by the deflection sensor,

located in the scanning head. The deflection sensor includes a laser, a mirror that reflects the laser beam onto the back of the cantilever, and a position-sensitive photodetector (PSPD). Both the frequency and the amplitude of cantilever vibration are monitored as changes in the position of the laser spot incident on the PSPD. The lock-in amplifier detects the AC signal at the lock-in frequency and output a DC signal proportional to its amplitude.

This DC output signal is sent to a comparator, or differential amplifier. The comparator compares the vibration amplitude of the cantilever to a reference amplitude setting (setpoint). An error signal proportional to the difference between these signals is sent to the z feedback controller that operates to raise or lower the z position of the scanner in order to maintain constant amplitude of the cantilever vibration. The cantilever (plus tip) is mounted on the scanner, and it moves relative to the sample. During the scan, the system controls the force gradient by adjusting the tip-to-sample spacing. The z voltage applied to the scanner to maintain a constant force gradient is used to generate an image of surface topography (z voltage vs. scanner position).

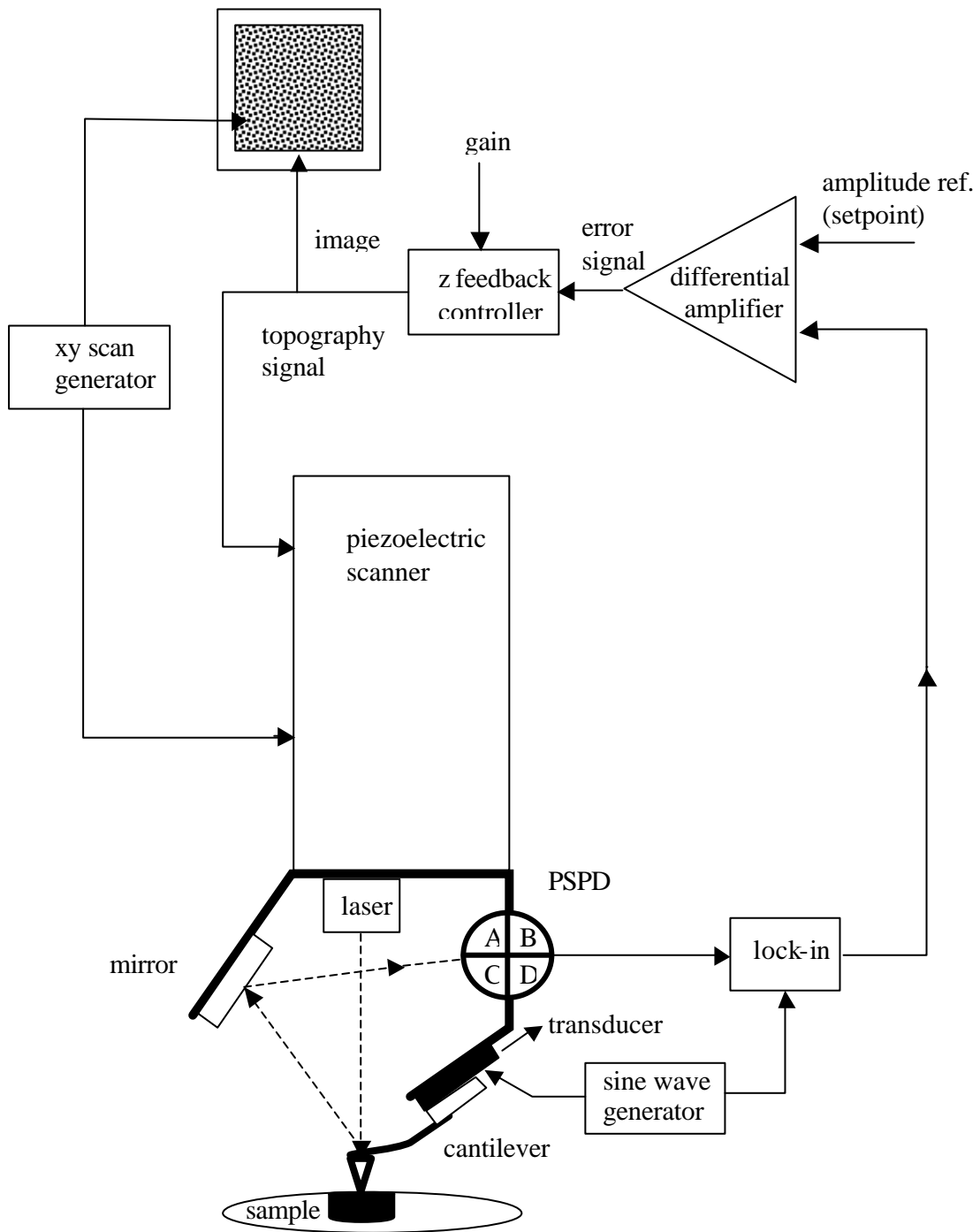


Figure 2.5 Diagram of hardware components and signal pathways for Autoprobe M5 operating in IC- and NC-AFM mode.



### 2.1.4 Resolution

The PSPD itself can measure displacements of light as small as 1 nm. The ratio of the path length between the cantilever and the detector to the length of the cantilever produces a mechanical amplification. As a result, the system can detect  $< 0.1$  nm vertical movement of the cantilever tip. Lateral resolution is determined by several factors, such as the scan size divided by the number of data points per scan line, the effective tip radius, the  $x$ - $y$  detector resolution, and the digitized step size of the scanner in the fast scan direction. Except the effective tip radius, other factors can be optimized through the selection of measurement conditions. In most cases, the largest limiting factor to the lateral resolution is the effective tip radius, or the interaction area between the tip and the sample. It is affected by both the physical radius of the curvature of the tip (tip sharpness) as well as other factors. Tip wear and deformation increase the interaction area for contact-AFM operation. The response of the measured signal to changes in tip-to-sample spacing affects the lateral resolution for non-contact AFM modes. Commercially available tips prepared from hard materials such as Si or  $\text{Si}_3\text{N}_4$  are normally with a radius of curvature on the order of 30-50 nm, tip shape and contact area remain problematic, for example, when scanning features with high aspect ratios or when attempting to detect single-molecule interactions. Two examples are shown in Fig. 2.6. In AFM topographic images, white parts are higher than black parts. Fig. 2.6 (left) is a topographic IC-AFM image of isolated single  $\text{G4NH}_2$  molecules on Au/mica. Grey flat region at the upper left part is an Au terrace. Some grey dots in the image are single  $\text{G4NH}_2$  molecules. The diameter of single  $\text{G4NH}_2$  in solution is 4.5 nm. Its height is  $\text{ca. } 1.3 \pm 0.3$  nm from the image. This is due to the deformation of  $\text{G4NH}_2$  on Au. It becomes oblate due to

multidentate Au-NH<sub>2</sub> interactions. Its diameter from our AFM image is 16 nm. This broadening is in part due to the tip convolution. Fig. 2.6 (right) shows the effect of aspect ratio on the lateral resolution. Due to a narrow distance between two features (marked by two lines), the tip cannot reach the bottom of these features. They are not well resolved. Features with large distance can be better resolved on the other hand.

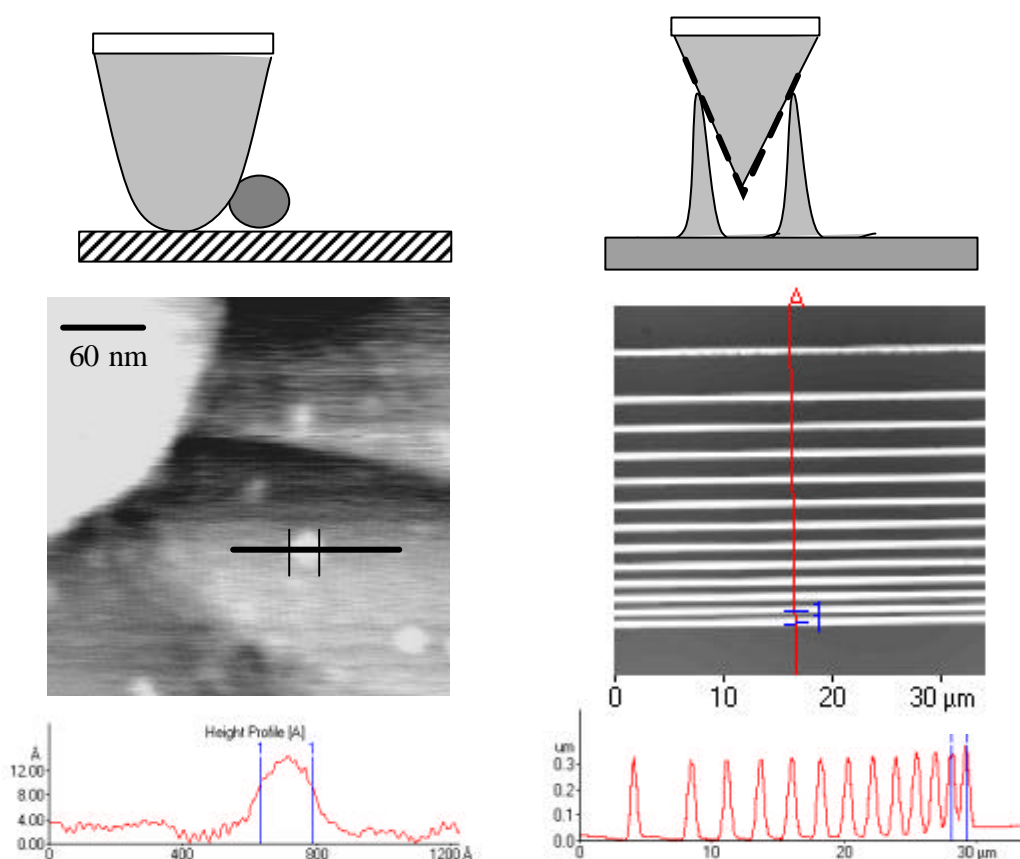


Figure 2.6 Topographic IC-AFM images of isolated single G4NH<sub>2</sub> molecules on Au/mica (left) and of a patterned stamp (right). Effects of tip convolution are schematically shown on the corresponding upper parts [Wu].

Developments aimed at reducing such problems are emerging. For example, carbon nanotubes (multi- or single-walled nanotubes) have been attached or grown at the

end of the AFM tip [Dai96, Wong98a]. Due to the decreased tip-sample contact area, the lateral resolution in tapping mode AFM can be reduced from 15 nm for conventional tips [Finot97] to 3 nm for single-walled nanotube-modified tips [Wong98b].

## **2.2 Microcontact printing (mCP)**

The  $\mu$ CP is a simple technique to obtain large-scale patterned structures within a short time. The realization of  $\mu$ CP needs four parts, i.e., master, stamp, ink and substrate. The master is a patterned structure made by various lithographic techniques. Stamps are made of elastomers and show the reverse pattern of the master since they are molded from the master. An often-used stamp material is polydimethylsiloxane (PDMS). Inks are the materials that are transferred from the stamp to the substrate. In principle, any material can be used as ink. However, the successful transfer of the ink from the stamp to the substrate is actually limited by many factors, such as solvent, interfacial properties of stamp and substrate, interaction between stamp and ink, and interaction between ink and substrate. Substrates can be “bare” or modified surfaces.  $\mu$ CP is the process of transferring ink molecules from the stamp to the substrate. It is comparable to stamping a postmark (equivalent to an inked stamp) on an envelope (equivalent to a substrate). Generally speaking,  $\mu$ CP is a very fast, cheap (multiple printing) and parallel technique to obtain patterned structures as opposed to sequential techniques such as scanning force lithography or e-beam lithography. In addition, apart from flat surfaces, curved surfaces can be also used. Due to these advantages,  $\mu$ CP has attracted much attention since its invention [Kumar93].

### 2.2.1 Types of the $\mu$ CP technique

Three types of  $\mu$ CP have been suggested so far. They are shown in Fig. 2.7.

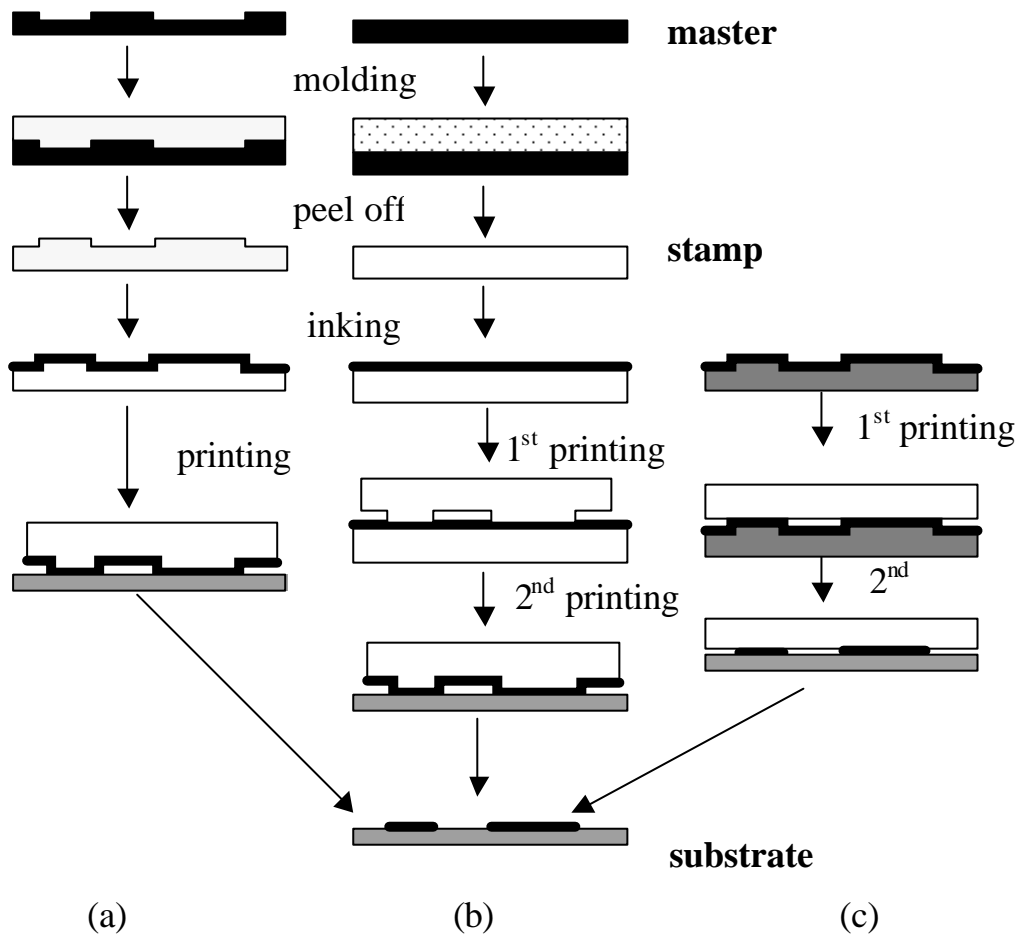


Figure 2.7 Schematic representations of three types of the  $\mu$ CP technique: (a) conventional, (b) contact-inking with flat inker pad, and (c) contact-inking with patterned inker pad.

Case (a) is conventional  $\mu$ CP and is widely used. A structured stamp is directly inked and then brought into conformal contact with the substrate. It is found that ink molecules are prone to accumulate at the edges of the structured stamp. This leads to more ink molecules at the edges of printed patterns and to the broadening of the printed

patterns. This disadvantage will be crucial for the case of very small pattern sizes. In order to reduce this effect, the procedure can be changed slightly to the so-called “contact-inking with flat inker pad” technique [Libiouille99, Pompe99] as shown in Fig. 2.7 case (b). Instead of inking a structured stamp, a flat stamp (“inker pad”) is inked first. Then the inked flat stamp is brought into conformal contact with the structured stamp. This obviously decreases the edge-accumulation effect during the inking step. During the contact period, the ink molecules move from the flat stamp to the protrusions of the structured stamp. After that, the structured stamp is brought into conformal contact with the substrate. This leads to the transfer of ink molecules to the substrate and completes the printing step. In case (b), two printing steps are involved. A comparison of case (a) and (b) is shown in Fig. 2.8 [Wu]. Figs 2.8 are topographic IC-AFM images of printed G8NH<sub>2</sub> dendrimers on Si wafers (throughout this work, Si wafer means Si wafer with an oxide layer). The cross-like protrusion (bright feature) is the printed G8NH<sub>2</sub> dendrimer pattern. As can be clearly seen, at the same ink concentration, we obtain 20 nm-high and 300 nm-wide stripes (white) at the edges of the pattern after conventional  $\mu$ CP, while after contact-inking  $\mu$ CP these stripes disappear. Some white dots on both images are due to large aggregates of dendrimers.

In case (c), a structured stamp is first inked and then contacted with the flat stamp (first printing). The printed flat stamp is brought into conformal contact with the substrate (second printing) [Geissler00]. Compared with case (a) and (b), case (c) has no advantages. First, it has the drawback of case (a) in the first printing step. Second, the fast diffusion of ink molecules on the flat stamp will obviously lead to broadening of the pattern during the first printing. Third, in the second printing, the height of the ink

molecules on the flat stamp is in the nanometer range. This requires utmost care for the second printing step. Therefore, under normal conditions, case (c) cannot compete with case (a) and (b). However, under special conditions, case (c) may benefit. When the inker pad is hard, for example, the patterns formed by microfluidic networks ( $\mu$ FN) on a Si wafer, the conformal contact between two hard surfaces is difficult to control. In this case, an elastomeric PDMS stamp, acting as an intermediate vehicle between the hard Si  $\mu$ FN and the hard substrate, can solve this problem. For case (c), the slow diffusion of ink molecules on both stamp and substrate is crucial for successful printing.

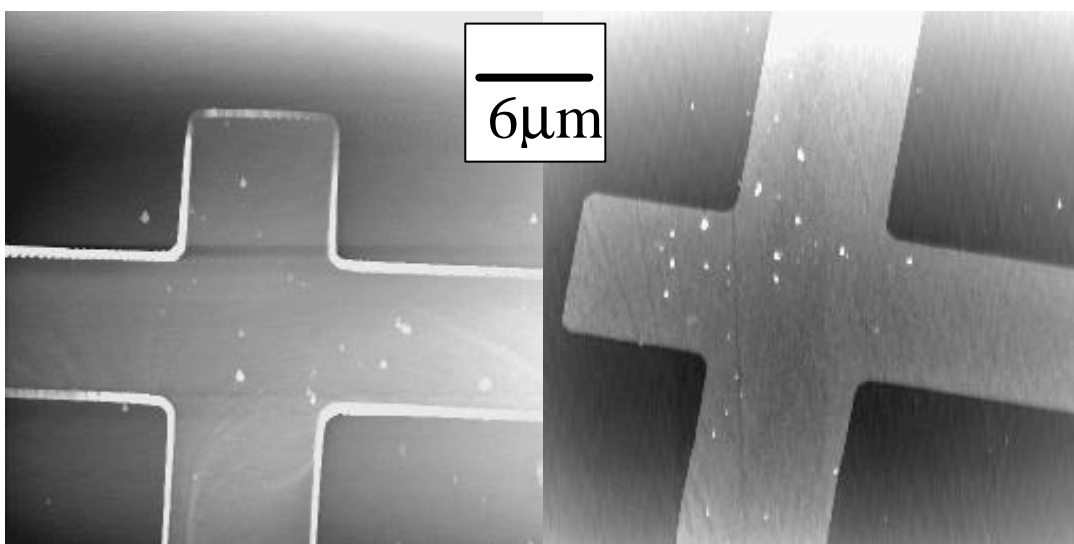


Figure 2.8 Topographic IC-AFM images of G8NH<sub>2</sub> dendrimers on Si wafers by (left) a conventional  $\mu$ CP and by (right) a contact inking with the flat inker pad technique. Ink: 5  $\mu$ M G8NH<sub>2</sub> in ethanol [Wu].

### 2.2.2 The development of the mCP technique

At the early stage of the development of the  $\mu$ CP technique, mainly long chain alkanethiols and alkylsilanes were used as ink molecules. They form passivation patterns

on Au substrates or Si wafers [Kumar93, Xia95]. Up to now, the realization of the patterning of functional materials via  $\mu$ CP is still mainly based on the direct printing of passivation SAMs [Ha00, Koide00, Harada01], rather than of functional materials themselves. For example, Koide et al. first printed an alkyltrichlorosilane on an indium-tin-oxide (ITO) glass substrate; then an organic light-emitting diode structure was deposited on the patterned substrate via a standard deposition technique [Koide00]. Since the printed SAM impeded hole injection into the hole transport layers, this rendered the stamped area essentially nonemissive. Although the whole substrate was covered with LED materials, only unpatterned regions exhibited effective emission. In this way, patterned LEDs were obtained. Harada et al. printed octadecyltrichlorosilane (OTS) on Si wafers. A Pt(0) complex was deposited preferentially in areas not covered by OTS and catalytically amplified the etching of the Si wafer underneath [Harada01]. Thus photoluminescent porous Si pixel arrays were obtained. The advantages for printing passivation SAM layers are that the system is relatively simple and that the interaction mechanisms among ink, substrate and stamp are well studied in these systems [Xia96, Delamarche98, Pompe99, Finnie00].

With the development of the  $\mu$ CP technique, much progress has also been made in direct printing of various functional materials [Yan98, Lahiri99, Kind99, Kind00b, Bernard00, Yang00, Hyun01, Wu02]. This can be further divided into two groups. One is the printing of carriers of actual functional materials, such as catalysts (or their precursors) [Kind99, Kind00b], guest molecules [Wu02], ligands etc. Among them, one representative example is the printing of reactive ligands on reactive SAMs or surfaces [Yan98, Lahiri99, Yang00, Hyun01]. For example, Yang et al printed  $\text{NH}_2$ -modified

biotin on an activated polymer surface. Biotin was covalently grafted to the activated polymer surface via an amidation reaction. The proteins were patterned via solution immersion and highly selective binding to the printed biotin molecules [Yang00]. This method has a certain generality and will find applications in biochemistry and cell biology. Another method is the printing of functional materials themselves. Although this is desirable, it is not straightforward since a compatible stamp-molecule-surface system is needed. The successful printing often requires detailed studies of various printing conditions such as ink species, concentration and time, printing time and surface properties of both stamp and substrate. Therefore, compared to the printing of passivation SAMs, the direct printing of various functional materials is more complicated. Recently, the transfer of self-assembled patterns of ink molecules formed on a stamp using the dewetting properties of the ink molecules has been reported [Erhardt01].

Considering the enormous range of variation in interfacial properties of stamp and substrate and in the species of ink molecules, we believe that the  $\mu$ CP technique is a very important tool for both basic research and for potential applications in building large-scale patterned structures.

## **2. 3 Dendrimers**

Since the first report of dendrimers [Buhleier78], two decades have passed. At the early stage, studies have been mainly focused on the synthesis of various kinds of dendrimers. Therefore, during the first ten years, their numbers remained low. With the progress in synthesis, especially the commercialization of PAMAM dendrimers and poly



(propylene imine) (PPI) dendrimers, publications involving applications of dendrimers boomed during the past ten years as shown in Fig. 2.9.

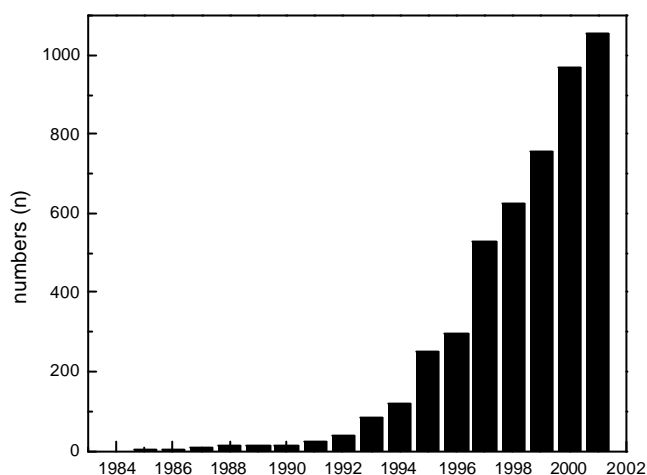


Figure 2.9 Number n of publications on dendrimers (Chemical Abstracts CAPLUS search).

Dendrimers are highly branched, monodisperse functional macromolecules [Zeng97, Fischer99]. From the structural point of view, as shown in Fig. 2.10 for PAMAM dendrimers, the morphology of the dendrimers changes from an open configuration to a globular one with increasing generations. This is due to the crowding of surface functional groups. Due to the increase in steric hindrance around the periphery with increasing the generations, access to the interior of dendrimers from outside becomes more difficult. In this way, the surface of dendrimers acts as a selective nanoscopic filter. For example, Zhao et al. found that catalytic properties of PAMAM dendrimer-encapsulated Pd nanoparticles for the hydrogenation of N-isopropyl acrylamide decreased from G4 to G8 dendrimers [Zhao99a]. On the other hand, the number of repetitive units and end groups shows an exponential increase with generation.

This could produce amplification of molecular effects due to the high density of functional units. From the viewpoint of chemical constituents, dendrimers are composed of three parts, i.e., core, repetitive units and terminal groups. By selecting different combinations of them, many interesting properties can be created [Fischer99, Cohen01]. For example, Gorman et al. used electroactive molecules as core and aromatic thiolates as repetitive units. With the change of the generation, the redox potential of the core molecules also changed [Gorman97].

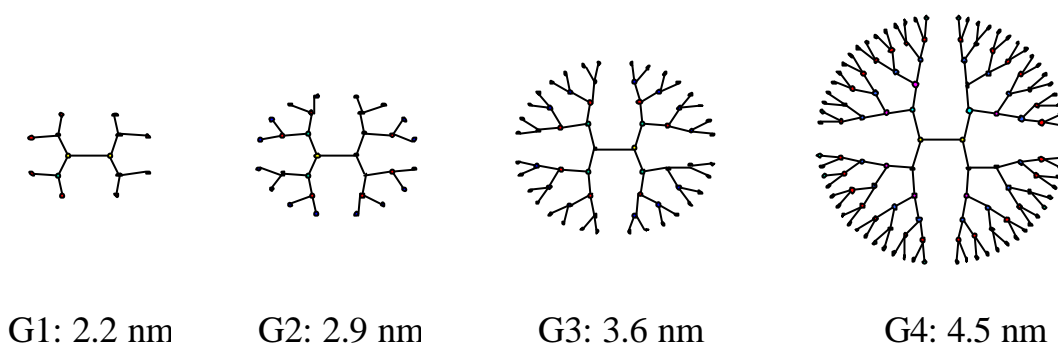


Figure 2.10 Schematic structures of PAMAM dendrimers from generation 1 (G1) to generation 4 (G4). Their diameters determined by size -exclusion chromatography are also shown [Crooks01].

From the viewpoint of structural design, dendrimers can be considered as a special kind of molecular core-shell-structure. When the composition or the functionality of core molecule and the repetitive unit is different, the former can be considered as core and the latter as shell. Thickness of the shell increases with the generation. For example, Y. Tomoyose et al. used a metalloporphyrin as interior core and an aryl ether as repetitive unit. They found that the encapsulation of the zinc porphyrin functionality by the dendrimer framework was nearly accomplished after 5 generations [Tomoyose96]. This

concept has been applied to the protection of small nanoparticles. It was found that the photochemical stability of semiconductor nanoparticles protected by dendron ligands increased with increasing generation [Wang02].

If the whole dendrimer molecule is considered as a core, another molecule that modifies the end groups of the core can be viewed as shell. Uppuluri et al. used  $\text{NH}_2$ -terminated PAMAM dendrimers as core molecules and  $\text{COOH}$ -terminated PAMAM dendrimers as shell molecules [Uppuluri00]. After protonation, the former became positively charged ( $\text{NH}_3^+$ -terminated). After deprotonation, the later became negatively charged ( $\text{COO}^-$ -terminated). When  $\text{COO}^-$ -terminated dendrimers were in surplus, they formed a kind of core-shell structure around  $\text{NH}_3^+$ -terminated dendrimers via electrostatic forces. This supramolecular core-shell assembly could become a covalent core-shell structure through a further amidation reaction.

Due to the specific configuration of dendrimers and the versatility of their constituents, applications in many different fields, such as biomedical diagnostics and therapy [Stiriba02], catalysis [Crooks00], scanning probe lithography [Tully99], are currently explored.

### **2.3.1 The structure, chemical and physical properties of PAMAM dendrimers**

Here, we only concentrate on one commercially available product, PAMAM dendrimers. Preparation of PAMAM dendrimers consists of a reiterative sequence of two basic reactions: a Michael addition reaction of amino groups to the double bond of methyl acrylate, followed by amidation of the resulting methyl ester with ethylene

diamine. The ester-terminated, half-generation dendrimers are denoted as Gn.5 and the full-generation amine-terminated dendrimers are denoted as Gn where n is the generation. For high-generation dendrimers, as shown in Fig. 2.10, interiors are rather hollow, while exteriors are more crowded. Therefore, the interiors of dendrimers can be used to encapsulate some nanometer-sized functional materials. For PAMAM dendrimers, the core is ethylenediamine, and the repetitive unit is  $-(\text{CH}_2\text{CH}_2\text{CONHCH}_2\text{CH}_2)_2\text{N}-$ , and terminal groups can be primary amine, hydroxyl, carboxylate etc.

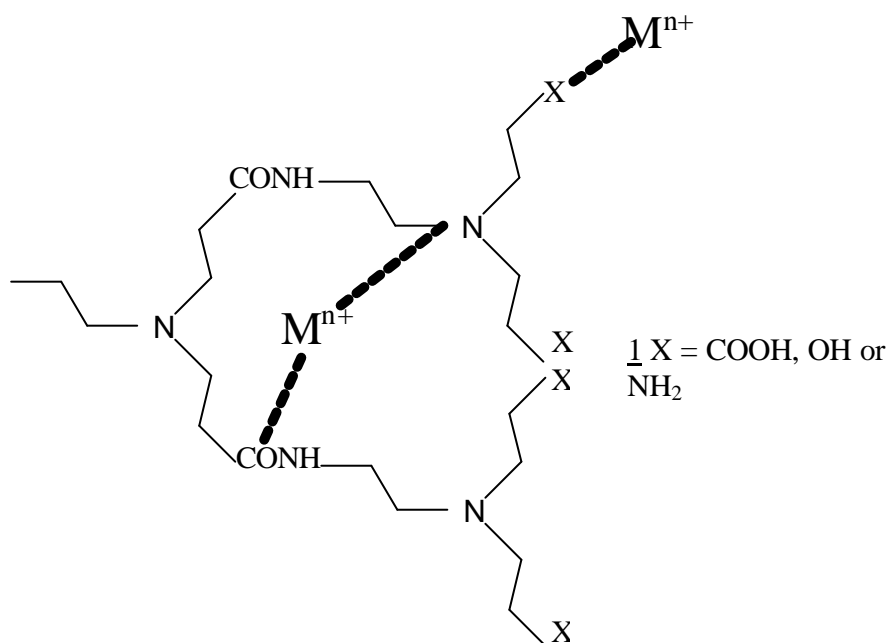


Figure 2.11 Interaction of metal ions ( $\text{M}^{n+}$ ) with chemical functional groups of PAMAM dendrimer outermost layer and terminal groups.

As shown in Fig. 2.11, the binding sites of dendrimers could be amide groups, primary amine groups, tertiary nitrogen groups, and carboxylate groups. The interaction strength of N-containing groups with metal ions normally follows the order  $-\text{NH}_2 > -\text{NR}_3$

> -CONHR (R is an alkyl chain) [Guilbault72, Ottaviani97]. Two examples are given in Fig. 2.12 and Fig. 2.13 [Wu]. Fig. 2. 12 shows the effect of  $\text{Cd}^{2+}$  ions on the UV/visible absorption spectra of G4OH and G4NH<sub>2</sub>. The absorption spectrum of pure dendrimers shows two bands that are related to C-N bonds. The strong one around 220 nm results from the  $\sigma \rightarrow \sigma^*$  transition of C-N bonds while the weak one around 270 nm corresponds to the  $n \rightarrow \sigma^*$  transition of C-N bonds. In order to show the change of the latter, the strong absorption peak of the former is not shown here. The effects of  $\text{Cd}^{2+}$  ions on the absorption spectra of dendrimer are small. For the  $\text{Cd}^{2+}$ /G4OH system, the  $\sigma \rightarrow \sigma^*$  and  $n \rightarrow \sigma^*$  transitions of the C-N bonds show a small decrease in absorbance intensity and no shift of the band. The superposition of the absorption spectra of pure G4OH and pure  $\text{Cd}(\text{CH}_3\text{COO})_2$  ( $\text{Cd}(\text{Ac})_2$ ) with a  $\text{Cd}^{2+}/\text{NR}_3$  molar ratio of 2/1 is also shown for comparison. It shows a negligible effect. For the  $\text{Cd}^{2+}$ -G4NH<sub>2</sub> system, the  $\sigma \rightarrow \sigma^*$  and  $n \rightarrow \sigma^*$  transitions of C-N bonds show a small degree of redshift, indicating an increased disturbance by  $\text{Cd}^{2+}$  ions compared with the case of G4OH. The superposition of the absorption spectra of pure G4NH<sub>2</sub> and pure  $\text{Cd}(\text{Ac})_2$  with a  $\text{Cd}^{2+}/(\text{NH}_2 + \text{NR}_3)$  molar ratio of 0.8 shows a small decrease in absorption due to dilution. Since the difference between G4OH and G4NH<sub>2</sub> is that G4NH<sub>2</sub> has primary amine groups, the interaction of  $\text{Cd}^{2+}$  with NH<sub>2</sub> groups must be stronger than its interaction with NR<sub>3</sub> groups, which also follows the usual trend in complex chemistry.

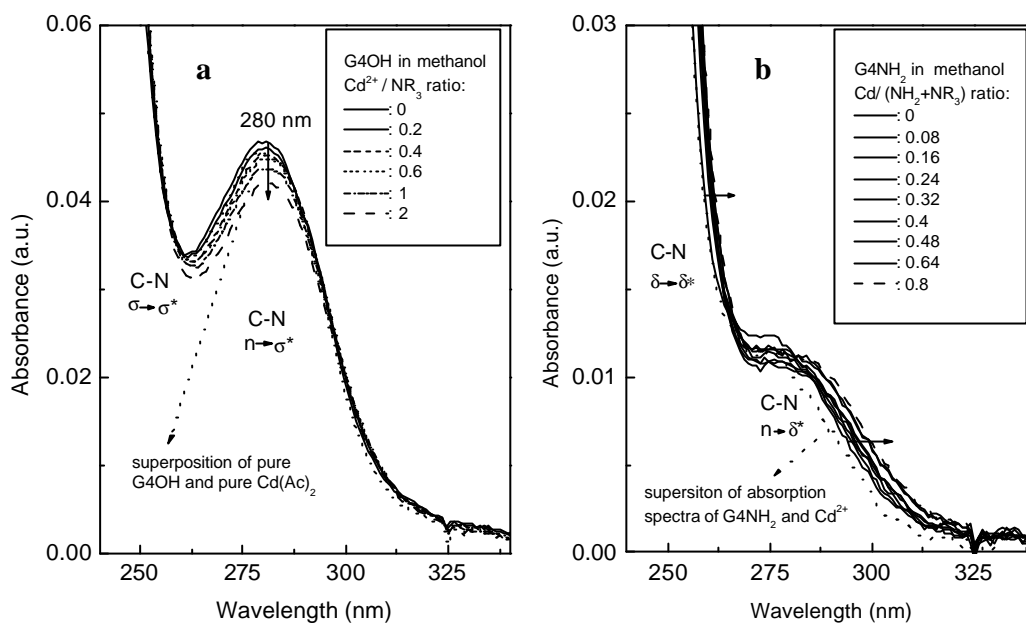


Figure 2.12 Effects of  $\text{Cd}^{2+}$  ions on the UV/visible absorption spectra of G4OH (a) and G4NH<sub>2</sub> (b) in methanol [Wu]

Fig. 2.13 shows the changes of absorption spectra of G4OH and G4NH<sub>2</sub> upon addition of  $\text{Co}^{2+}$  ions. For G4OH dendrimers, the effect of adding  $\text{Co}^{2+}$  ions is very weak. The increase in absorption intensity at the  $n \rightarrow \sigma^*$  transitions of C-N bonds (280 nm) is due to the contribution of  $\text{Co}^{2+}$  aqueous complex. A long wavelength absorption band at 510 nm is due to the d-d transition band of  $[\text{Co}(\text{H}_2\text{O})_6]^{2+}$  complex. A superposition of the absorption spectra of pure G4OH and pure  $\text{Co}^{2+}$  aqueous complex with a  $\text{Co}^{2+}/\text{NR}_3$  ratio of 6.4 is nearly identical with the absorption spectrum of the mixture of both at this ratio. In contrast, for G4NH<sub>2</sub> dendrimers, a new strong ligand metal charge transfer (LMCT) band forms. It appears as a shoulder around 280 nm. With increasing amount of  $\text{Co}^{2+}$  ions, the absorption intensity of this new band first increases, and then gradually saturates. The absorption at long wavelength regions also show new absorption structures

at 584 nm and 638 nm, indicating the formation of Co-NH<sub>2</sub> bonds via a ligand substitution reaction. Since the interaction of Co<sup>2+</sup> with G4OH is negligible, we can use the change in the LMCT band to evaluate the loading factor of Co<sup>2+</sup> ions to NH<sub>2</sub>-terminated dendrimers. As shown in one inset of Fig. 2.13b, the ratio Co<sup>2+</sup>/NH<sub>2</sub> is around 1/2. This ratio agrees with its complexation with nonylamine, indicating that two water molecules bound to Co<sup>2+</sup> ions are displaced by two NH<sub>2</sub> groups [Allan93]. This ratio corresponds to 32 Co<sup>2+</sup> ions for a single G4NH<sub>2</sub> molecule and 512 Co<sup>2+</sup> ions for a single G8NH<sub>2</sub> molecule, respectively. From these two examples we can draw the following three conclusions. First, for both Cd<sup>2+</sup> and Co<sup>2+</sup> ions, interaction with primary amine groups is stronger than that with tertiary amine groups. This order has already been verified for other metal ions such as Cu<sup>2+</sup>, Pd<sup>2+</sup> and Pt<sup>2+</sup> [Zhao98, Zhao99a, Zhao99b]. Second, The effects of Cd<sup>2+</sup> ions to the UV/visible absorption spectra of G4OH and G4NH<sub>2</sub> are very small, this excludes the possibility to estimate the loading factor of Cd<sup>2+</sup> ions to dendrimers using a simple spectroscopic titration. In contrast, this can be fulfilled for the Co<sup>2+</sup>-G4NH<sub>2</sub> system. Third, Co<sup>2+</sup> ions show a very high selective binding with NH<sub>2</sub>-terminated dendrimers compared with OH-terminated ones. This is in contrast with other metal ions such as Cu<sup>2+</sup>, Pd<sup>2+</sup> and Pt<sup>2+</sup>. Their interactions with the above two dendrimers have been studied and do not show this high selectivity. The interactions between Co<sup>2+</sup> ions with small molecules such as mono- and trimethylamine do not show such a large difference either [Guilbault72]. The reason for this high selectivity is unclear at the moment.

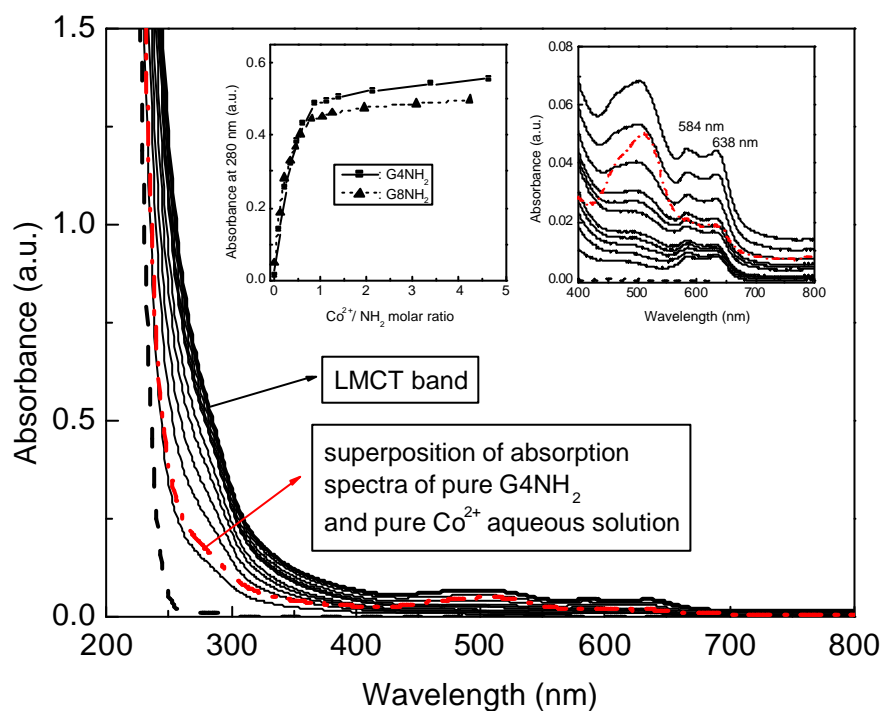
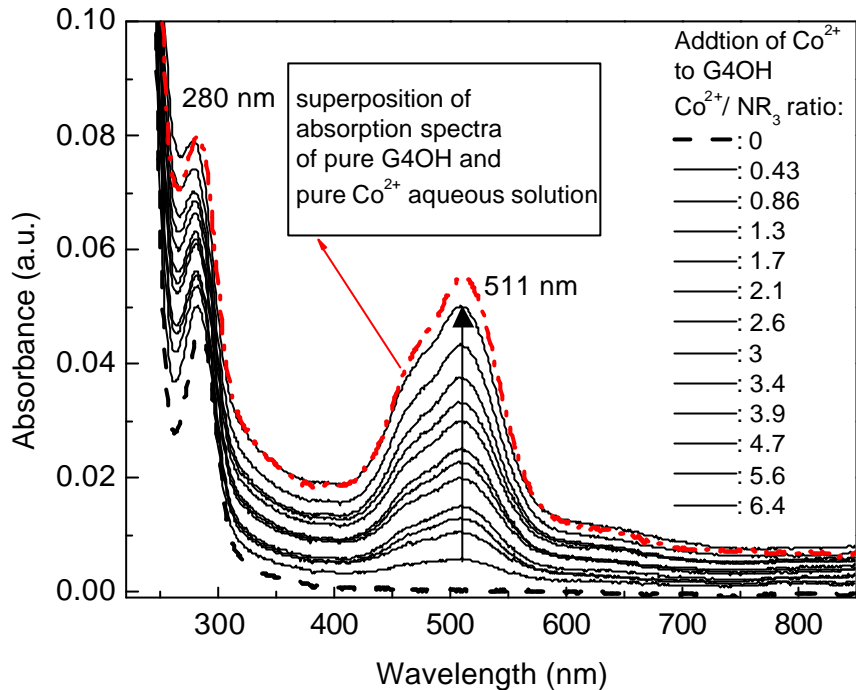


Figure 2.13a Effects of  $\text{Co}^{2+}$  ions on the UV/visible absorption spectra of G4OH.

Figure 2.13b Evolution of the UV/visible absorption spectra of G4NH<sub>2</sub> in water by adding  $\text{Co}^{2+}$  ions. Inset:  $\text{Co}^{2+}$  ion spectroscopic titration curves for G4NH<sub>2</sub> and G8NH<sub>2</sub> dendrimers and absorption changes in d-d transitions of  $\text{Co}^{2+}$  by complexation with N-containing groups [Wu].



Binding between  $\text{Co}^{2+}$  and PAMAM dendrimers is pH dependent. Fig. 2.14 shows the evolution of absorption spectra upon adding  $\text{H}^+$  ions. The d-d transition bands arising from complexation between  $\text{G4NH}_2$  and  $\text{Co}^{2+}$  at 584 nm and 638 nm decrease with increasing the amount of  $\text{H}^+$  (corresponding to decreasing pH). Finally, these two bands disappear and the band corresponding to  $[\text{Co}(\text{H}_2\text{O})_6]^{2+}$  dominates at 511 nm. This indicates that the protonation of amine groups from the dendrimers is in competition with their complexation with metal ions. On the other hand, it verifies that these two bands are related to the binding of  $\text{Co}^{2+}$  to amine groups of the dendrimers.

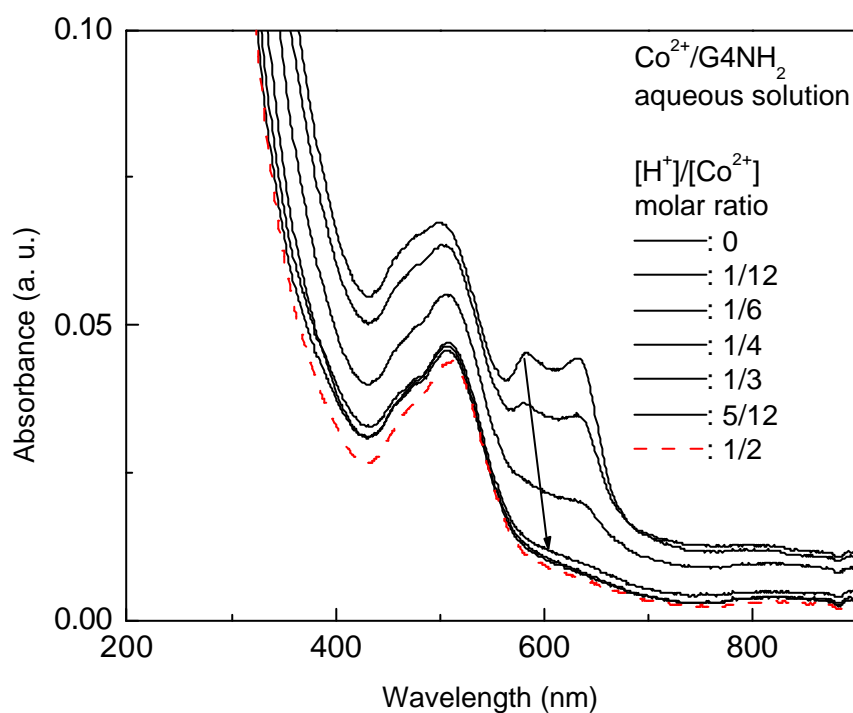


Figure 2.14 Effects of adding  $\text{H}^+$  on the UV/visible absorption spectra of  $\text{Co}^{2+}/\text{G4NH}_2$  aqueous solution [Wu].

Apart from these two interactions, other interactions, such as electrostatic forces and acid-base interactions [Groehn00], have also been explored to bind metal ions to dendrimers.

### **2.3.2 Dendrimers as nanotemplates (nanoreactors)**

As is well known, the synthesis of nanoparticles usually needs templates or stabilizers. Most of templates are however not single molecules and therefore exhibit size distribution. Dendrimers are monodisperse and can be a template with a highly defined size for the synthesis of nanoparticles. According to the relative position of the synthesized nanoparticles with the dendrimers, we can classify nanoparticle/dendrimer composites into two types. When the synthesized nanoparticle is located inside a dendrimer, we call them internal type (“I” type), for example: Cu [Zhao98], Pt and Pd/G4OH nanocomposites [Zhao99a and Zhao99b]. When the synthesized nanoparticle is located at the periphery of a dendrimer, we call them external type (“E” type), for example: Ag/G4OH [Zheng02] and Au/GnOCH<sub>3</sub> (methoxy-terminated PAMAM dendrimer generation n) [Esumi01, Torigoe01] and CdS/G4NH<sub>2</sub> [Soolkal98]. The types of the synthesized nanocomposites are determined by many factors, such as binding sites and strengths, reaction paths etc. [Balogh99]. For the Pd/G4OH system, since Cl<sup>-</sup> ions from PdCl<sub>4</sub><sup>2-</sup> are easily substituted by interior tertiary N, the binding of Pd<sup>2+</sup> ions are confined inside the dendrimer. The size of the resulting Pd nanoparticles (1.3 ± 0.3 nm) is slightly larger than the theoretical value of 1.1 nm (G4OH/Pd<sub>40</sub>), which is calculated using the assumption that the particles are contained within the smallest sphere that circumscribes the Pd crystals with face-centered cubic packing [Zhao99b]. The less than

2 nm diameter for Pd particles we obtained using the same procedure (Fig. 2.15a) verifies the above results. This diameter is smaller than the diameter of G4OH (4.5 nm), indicating the encapsulation of Pd nanoparticles inside the dendrimer. Therefore, Pd/G4OH nanocomposites belong to the “I” type. For the Ag/G4OH system, although the binding of  $\text{Ag}^+$  ions with tertiary N is confined inside the dendrimer, it is less favorable compared to  $\text{Pd}^{2+}/\text{G4OH}$  system [Crooks01]. The size of the resulting Ag nanoparticles (ca. 7 nm) is larger than the diameter of the host dendrimers. Since the synthesized Ag nanoparticles are very stable, it is most likely that each Ag nanoparticle is surrounded by several dendrimers. When the binding of metal ions to dendrimers is at the terminal groups of the dendrimers, “E” type nanocomposites are normally formed. For example, for the  $\text{Cd}^{2+}/\text{G8NH}_2$  system, as shown above,  $\text{Cd}^{2+}$  ions interact more strongly with exterior primary N than with interior tertiary N. The binding sites of  $\text{Cd}^{2+}$  ions are thus at the periphery of  $\text{G8NH}_2$ . After addition of  $\text{S}^{2-}$  ions, CdS nanoparticles nucleate and grow at the surface of the dendrimers. Therefore  $\text{CdS}/\text{G8NH}_2$  belongs to the “E” type. Fig. 2.15b shows the possible configuration of  $\text{CdS}/\text{G8NH}_2$  nanocomposites and a TEM image. The average size of CdS nanoparticles is ca. 2 nm ( $\text{Cd}_4\text{S}_4$ ) and agrees with the size obtained from absorption spectra. Details will be given in Chapter 4.

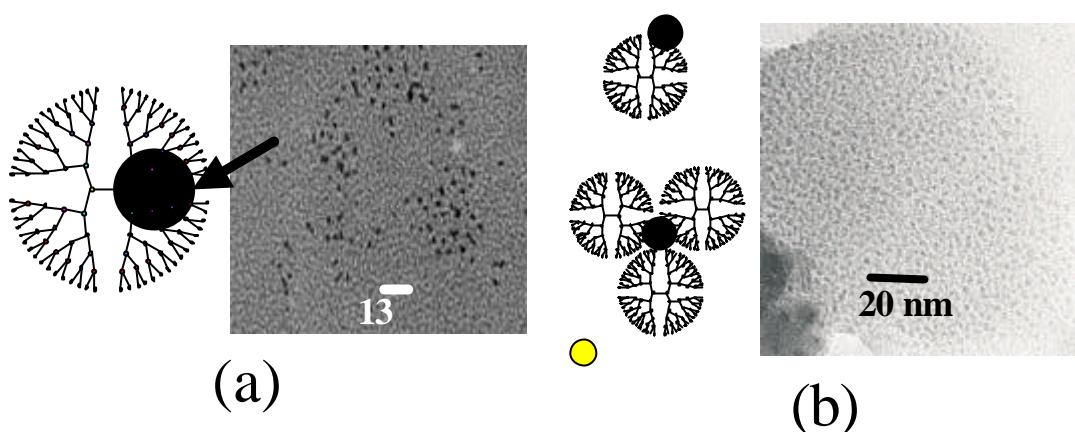


Figure 2.15 Schematic representations and TEM images of (a) Pd/G4OH (“I” type) and (b) CdS/G8NH<sub>2</sub> (“E” type) [Wu].

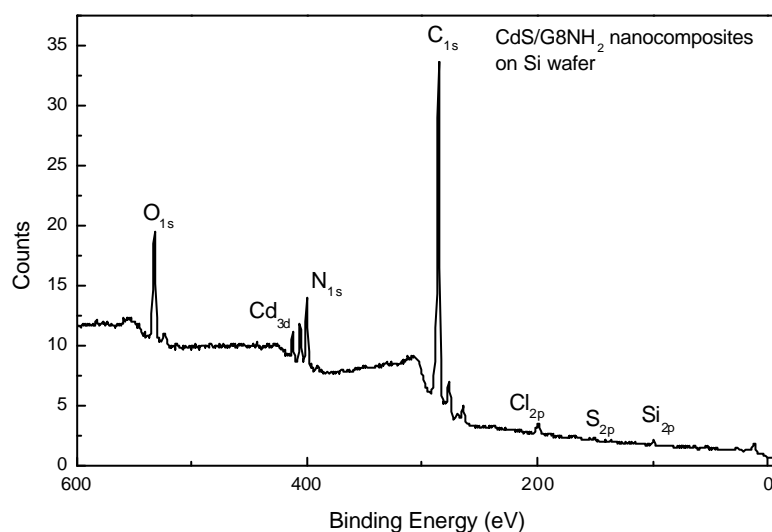


Figure 2.16 Survey XPS spectrum of CdS/G8NH<sub>2</sub> (initial Cd<sup>2+</sup>/S<sup>2-</sup> = 3/1) nanocomposites on a Si wafer [Wu].

Fig. 2.16 is a survey XPS spectrum of CdS/G8NH<sub>2</sub> nanocomposites (dialysis against methanol overnight before deposition) on a Si wafer [Wu]. C, N, O signals are mainly from G8NH<sub>2</sub> dendrimers while Cd and S signals are from CdS nanoparticles. Cl,

Si, and O signals are from the Si wafer. Lack of Na ( $\text{Na}_2\text{S}$  is the source for sulfide) signal indicates that byproducts are removed by dialysis.

Although metal ions in each dendrimer are homogeneously distributed due to the homogeneous distribution of the chemical binding sites in the dendrimer, the difference in binding affinity will influence the nucleation and growth process in a subsequent step. A strong binding will either favor the formation of smaller nuclei or limit the mobility of formed nuclei. This will lead to smaller nanoparticles. Therefore, through the control of the binding of metal ions to dendrimers, we can control the size of nanoparticles. One example is given in Fig. 2.17. For semiconductor nanoparticles, absorption band gap and photoluminescence (PL) blueshift with decreasing particle size. The dependence of the band gap on the radius,  $R$ , is approximated by [Brus84]:

$$E(R) = E_g + \hbar^2 \pi^2 / 2R^2 [1/m_e + 1/m_h] - 1.8e^2 / \epsilon R + \dots \quad (2.1)$$

This formula depends only upon known bulk parameters: the two effective masses,  $m_e$  and  $m_h$ , and the dielectric constant at optical frequencies,  $\epsilon$ . Therefore, the size of particles can be estimated from the degree of blueshift. We keep the concentrations of G3.5COOH, G4NH<sub>2</sub>, and G4OH at 78  $\mu\text{M}$  and with a  $\text{Cd}^{2+}$ /dendrimer ratio of 26/1. From Fig. 2.17, it can be seen that the size of the CdS nanoparticles increases in the order G3.5COOH < G4NH<sub>2</sub> < G4OH. The binding affinity of different chemical groups in dendrimers to  $\text{Cd}^{2+}$  ions follows the trend:  $-\text{COOH} > -\text{NH}_2 > -\text{NR}_3 > \text{CONHR} > -\text{OH}$ . This agrees with our assumption. In addition, since the numbers of dendrimer molecules and the total amount of  $\text{Cd}^{2+}$  and  $\text{S}^{2-}$  ions are identical, this means

that the average numbers of CdS nanoparticles per dendrimer increase in the order  $G4OH < G4NH_2 < G3.5COOH$ .

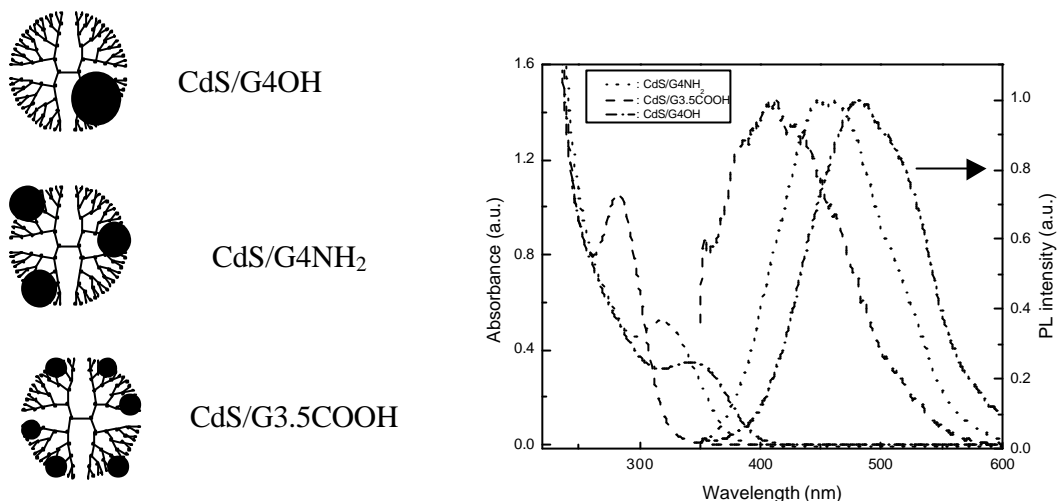


Figure 2.17 (left) Schematic representations of CdS nanoparticles in methanol using G3.5COOH, G4NH<sub>2</sub> and G4OH as nanoreactors [wu].

Figure 2.17 (right) Corresponding UV/visible absorption and PL spectra (right). For PL spectra the excitation wavelength is 320 nm [Wu].

### 2.3.3 Monolayers and multilayers of dendrimers

PAMAM dendrimers terminated by NH<sub>2</sub>, COOH and OH groups can adsorb on oxide or OH-terminated surfaces via hydrogen bonds. Fig. 2.18a shows an example for the adsorption of G4OH, G4NH<sub>2</sub> and G8NH<sub>2</sub> dendrimers on a Si wafer [Wu]. Through solution immersion, dendrimers adsorb onto the Si wafer. The adsorption process is very fast and reaches nominal monolayer thickness for all three dendrimers within several minutes. Further immersion changes the ellipsometric thickness little. Hence a nominal monolayer is formed. The heights of G4 and G8 monolayers are ca.1.2 nm and 3.3 nm, respectively. These values show a large deviation from their ideal spherical diameter of

4.5 nm for G4 and 9.7 nm for G8. These heights are however close to the heights of single G4 and G8 dendrimers on hydrophilic surfaces [Tsukruk97]. This indicates that the strong interaction with hydrophilic surfaces deforms dendrimers. They show oblate morphology on these surfaces. A topographic IC-AFM image of a G4NH<sub>2</sub> monolayer on a Si wafer is shown in Fig. 2.18b. The G4NH<sub>2</sub> monolayer is quite flat as can be seen from the height profile.

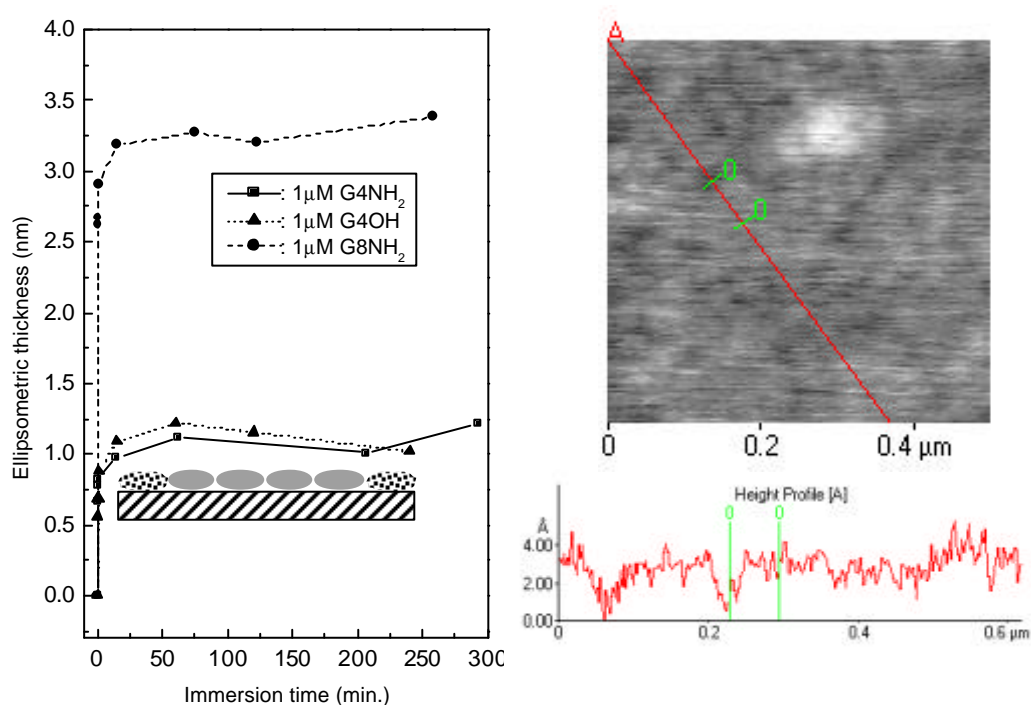


Figure 2.18 (left) Ellipsometric thickness of G4OH, G4NH<sub>2</sub> and G8NH<sub>2</sub> on Si surfaces measured in air after immersion, rinsing with ethanol and drying with argon [Wu].

Fig. 2.18 (right) Topographic IC-AFM image of G4NH<sub>2</sub> monolayer on a Si wafer [Wu].

Apart from monolayers, multilayers of dendrimers can be formed. Electrostatic forces [Tsukruk97] and metal ligand interaction [Zhang02] are employed for this

purpose, as shown in Fig. 2.19. Because of the adsorption properties of dendrimers, they are also good inks for the  $\mu$ CP technique [Wu02, LiH02]. Fig. 2.20 displays SEM images of printed G4NH<sub>2</sub> on an Au/Cr/glass substrate and of printed G8NH<sub>2</sub> on a Si wafer [Wu]. The bright parts are printed dendrimers layers. The stripe structures on Au are Au terraces.

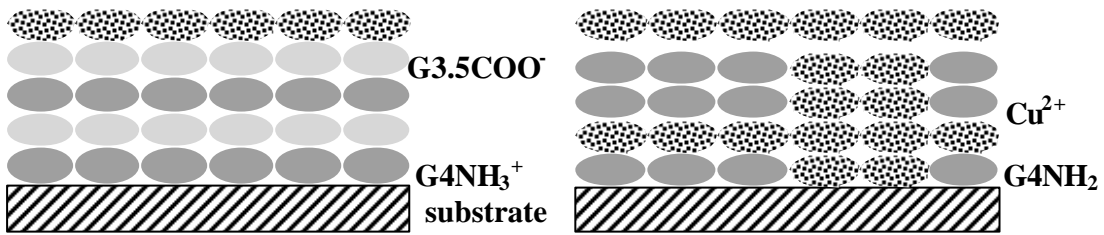


Figure 2.19 Schematic representations of the buildup of dendrimer multilayers based on (a) electrostatic forces and (b) metal–ligand interactions.

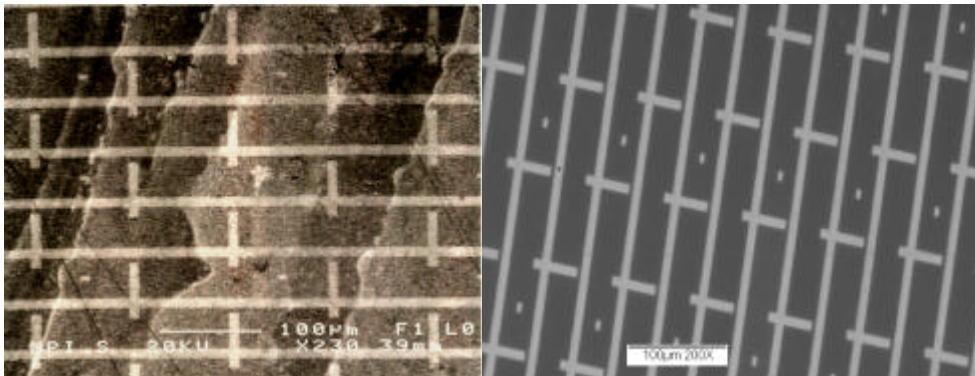


Figure 2.20 SEM images of printed G4NH<sub>2</sub> dendrimers on an Au/Cr/glass substrate (left) and of printed G8NH<sub>2</sub> dendrimers on a Si wafer (right) [Wu].



## 2.4 Design of patterned functionality on surfaces

The  $\mu$ CP technique can realize large-scale predefined structures. We term this “primary organization”. At each pattern, the control of the distribution of nano-objects or a modification can be further refined. For example, a pattern with catalytic metal nanoparticles can be used to metallize the whole pattern via electroless deposition (ELD) (path 1). Arrangement of nano-objects in a certain way can be used to obtain isolated or collective nano-functionalities (path 2). We call these processes “secondary organization”.

These strategies are shown in Fig. 2.21. Path 1 is straightforward: We can print passivation layers and use unprinted regions for the ELD of metal as shown in Fig. 2.22. We can also print active layers and use them to guide the ELD process as will be shown later in chapter 3. For path 2 the spatial positioning of nano-objects is crucial. In most cases, when nano-objects are brought to the surface, they or their aggregates randomly distribute on the surface (Fig. 2.21 case (b)). In special cases, they attain a certain degree of order on the surface due to self-assembly processes (Fig. 2.21 case (c)). The most accurate way to arrange nano-objects in an arbitrary way might be arranging nano-objects using nanolithography technique (Fig. 2.21 case (d)).

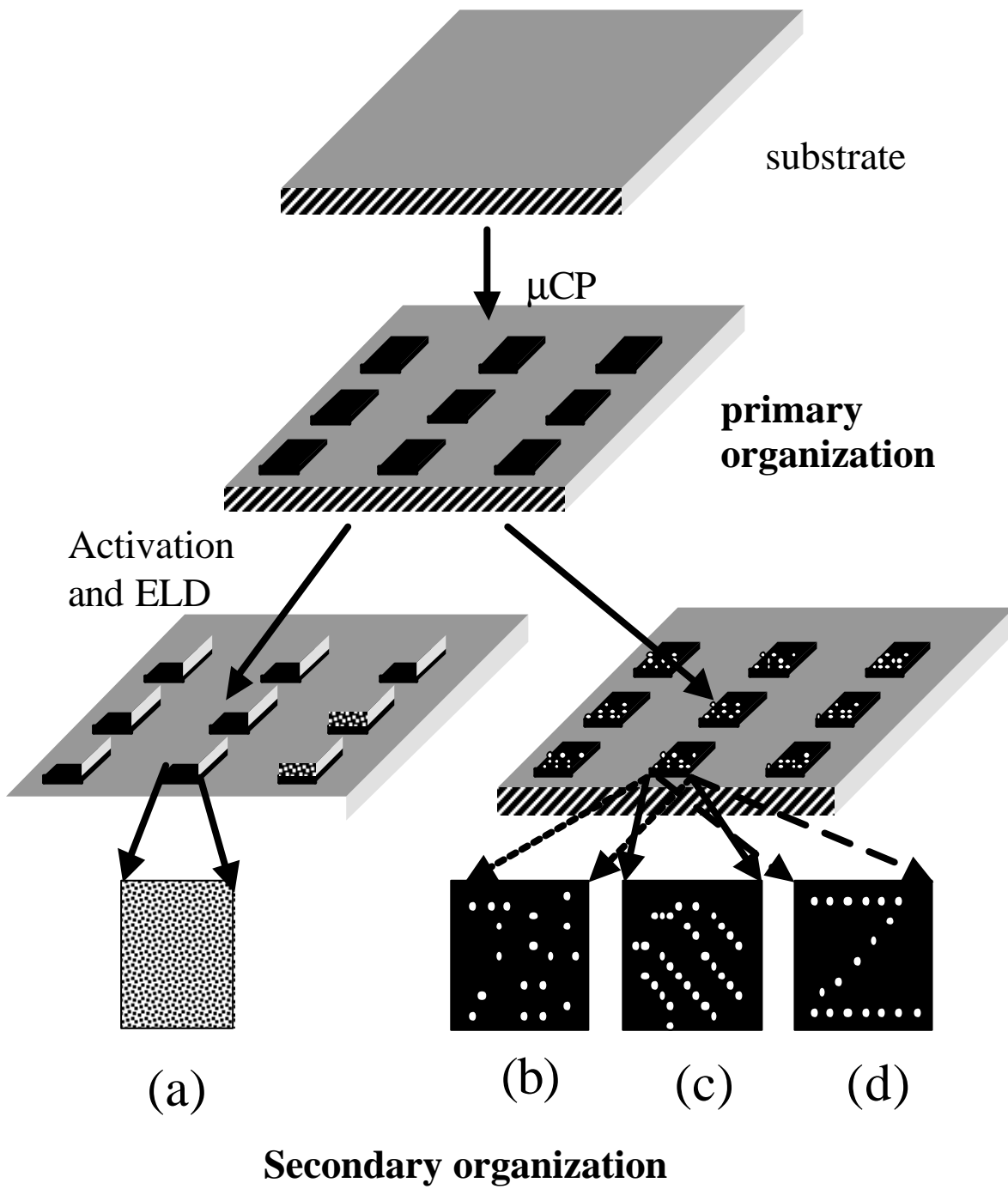


Figure 2.21 Schematic diagram for the realization of patterned bulk- and nano-functionality.

### 2.4.1 Primary Organization

It is well known that long chain alkanethiols form high quality passivation layers on Au substrates. They can be printed to Au surfaces to form passivation patterns. Unprinted regions can be used to obtain a further functional modification. One example is given below [Bittner02]. In case (a) of Fig. 2.22, a  $\text{CH}_3(\text{CH}_2)_{17}\text{SH}$  ink is printed to an Au/Cr/glass substrate;  $\text{G}_4\text{NH}_2$  dendrimers adsorb on the bare Au. Due to the structure of the dendrimers, they allow the penetration of copper ions to the Au underneath, which acts as catalyst for the formation of copper patterns. The obtained copper patterns are in contact with the Au substrate. In this case, the dendrimer monolayer effectively slows down the ELD rate of copper. Without the dendrimer monolayer, the ELD reaction can be so fast that homogeneous copper patterns cannot be obtained. In case (b), instead of pure dendrimers, alkanethiol-modified dendrimers are used. The Au underneath the thiol-modified dendrimers plays no role as catalyst. In this case, copper nanoparticles are first formed in the dendrimers and then act as catalyst for the formation of copper patterns. In this way, the formed copper patterns in principle are not in a direct contact with the Au substrate.

Apart from alkanethiols on Au substrates, printed alkylsilanes are used to form passivation patterns on oxide substrates. Gas phase depositions of metal on the unprinted regions are achieved [Xia95, Jeon97].

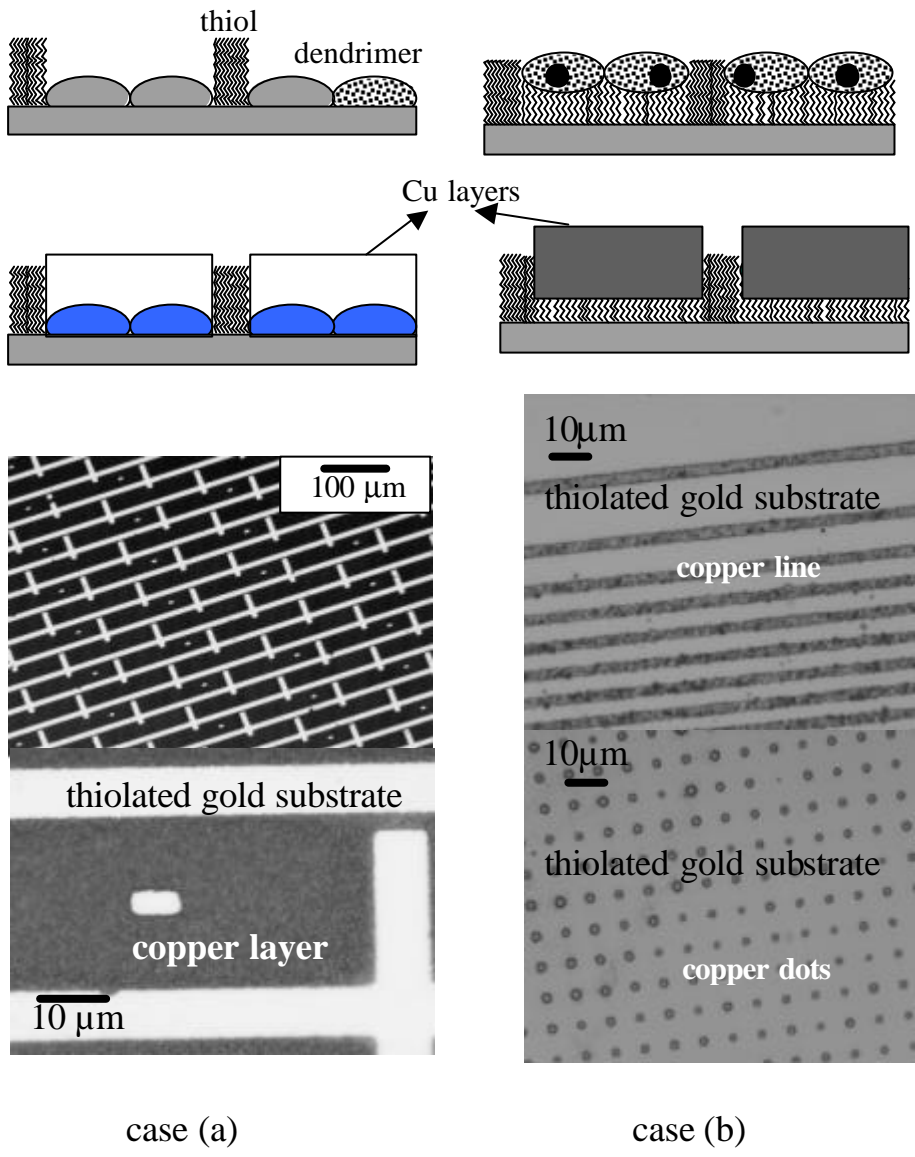


Figure 2.22 Schematic diagram and optical microscopy images of copper patterns [Bittner02], see text.

## 2.4.2 Secondary Organization

Bringing nanoparticles (here semiconductor and metal) onto surfaces can be obtained in two ways. In the first way, nanoparticles are first synthesized using wet chemical methods, then brought to the surface via either physisorption or chemical interaction. In the second way, nanoparticles are directly deposited on surfaces. The density of nanoparticles is controlled by dilution with nonfunctional molecules or by controlling deposition parameters. Since the nanoparticles are normally brought to surfaces through a dilution procedure, their distribution on the surface is statistical. That is, we cannot accurately control the position of each nanoparticle. However, some applications require the accurate control of spatial position and number of nanoparticles on surfaces [Qin99, Massey01]. Apart from nanolithographic techniques, two ways that arrange nano-objects in a parallel process can be explored. We term the first way “self-assembly” [Fogg97, Sun99]: Due to the inherent interaction between nano-objects, they form regular patterns, such as hexagonal packing of monodisperse spherical hard nanoparticles [Murray95]. The second way relies on external forces, e.g., from an electric field [Smith00], Langmuir technique [Markovich99], an electromagnetic radiation [Murakoshi00, Vossmeier97], or a magnetic field [Legrand01], to align nano-objects in a regular way.



## Chapter 3

# Spatially Selective Electroless Deposition of Cobalt on Oxide Surfaces Directed by Microcontact Printing of Dendrimers

In this chapter we first explore the capability of pure G4OH dendrimers as ink molecules. After that, the potential of G4OH dendrimers to bind  $\text{Pd}^{2+}$  ions inside the dendrimer is used to control the binding of the latter. The resulting Pd nanoparticles after reduction are catalytically active and can act as nucleation centers for electroless cobalt plating. We produce cobalt structures down to several hundred nanometers lateral size and up to several tens of nanometer thickness with high spatial selectivity. The printed dendrimers are cage-like molecules with well-defined chemical groups; hence they can selectively bind guest molecules (here palladium complexes) when the latter possess chemical groups that favor a host-guest interaction. Printing dendrimers therefore points towards a more general method to create patterns with chemical functionality.

### 3.1 Introduction

Up to now, the best system for  $\mu\text{CP}$  is printing thiols on Au substrates since the substrate is a well-defined surface (a single crystal can be employed) and since the printed layer is monomolecular and well characterized. Lateral structures of 100 nm and

less have been achieved [Xia96, Delamarche98]. In chapter 2.3, we demonstrated the realization of patterned copper layers using the combination of printing passivation long chain alkanethiol on an Au substrate with ELD of metal layers on unprinted regions [Bittner02]. However, the use of the thiols restricts the choice of surfaces to several metals like Au or Cu. For many experiments, the extension of  $\mu$ CP to other substrates is desirable, especially when non-conducting surfaces such as oxide surfaces are required. One simple way to pattern oxide surfaces is via direct  $\mu$ CP of chlorosilanes [Xia95, John96, Wang96, Pompe99]. However, this method has limitations: (1) Due to the sensitivity of chlorosilanes to environmental parameters such as humidity and temperature, the quality of chlorosilane-based printed SAMs is difficult to control and to guarantee. (2) The solvents for chlorosilanes are hydrocarbons; they can easily swell the PDMS stamps. This will lead to a distortion of the printed pattern, especially for small feature sizes. An alternative method to pattern oxide surfaces is the so-called lift-off technique [Walheim99]; it is based on printing thiols on Au/Ti/Si substrates, followed by several passivation and etching steps. In this way, an inverse of the original pattern is obtained on oxide surfaces. Although this method avoids the disadvantages of direct printing of chlorosilanes, many steps are involved in obtaining a patterned surface. Therefore, molecules that avoid the disadvantages of alkylsilanes are desirable for directly patterning oxide surfaces. Dendrimers can be such a candidate. They are less sensitive to the environmental parameters, have a good solubility in alcoholic solvents, and can form layers on various surfaces including oxide surfaces.

ELD of metals is a process widely used for the production of fine metal patterns in printed circuits [Mallory90]. ELD occurs by an autocatalytic redox process, which



generally takes place only on surfaces capable of catalyzing it. Noncatalytic surfaces first have to be "activated" with a metal catalyst before the metallization can occur. Selective deposition can be achieved either by selective deactivation of a catalytic substrate [chapter 2.3, Bittner02] or by selective activation of a nonreactive surface by a catalyst [Putten93]. An oxide surface patterned with dendrimer-stabilized noble metal nanoparticles will be an ideal system to study the catalytic properties of these particles for the ELD process.

G4OH dendrimers are selected as inks. As we know from chapter 2.2.3, they form monolayers on oxide surfaces via hydrogen bonds by solution adsorption. The potential of them as ink molecules is first explored. After the optimization of printing conditions,  $\text{Pd}^{2+}$  ions are bound to the printed G4OH molecules via solution adsorption. Upon immersion of a patterned substrate in a cobalt ELD bath, a selective deposition of cobalt films on the patterned regions is realized. We chose cobalt patterns as an example since we aim at showing that  $\mu\text{CP}$  can also produce conducting and even magnetic patterns on Si wafers; such patterns usually have to be fabricated by lithographic techniques. Our method allows to fabricate lines, pixels etc. on any surface that contains a sufficient amount of hydroxyl groups.

## 3.2 Experimental part

**Substrates and stamps.** Si wafers (orientation (100), Crystal, Berlin) are terminated by silicon oxide with OH groups by the standard RCA procedure: 15 min immersion into a 340-350 K hot 1:1:5 mixture of 25%  $\text{NH}_4\text{OH}$  (VLSI Selectipur, Merck), 31%  $\text{H}_2\text{O}_2$  (VLSI Selectipur, Merck) and water (Millipore, 18  $\text{M}\Omega\text{cm}$ ); 15 min immersion into a

340-350 K hot 1:1:5 mixture of 37% HCl (Suprapur, Merck), 31% H<sub>2</sub>O<sub>2</sub> and water. PDMS stamps (Sylgard 184, Dow Corning) are formed on flat polystyrene dishes or patterned Si wafer masters (IBM Zürich and IMS Stuttgart; before first use each master is rendered hydrophobic with fluoroalkyl-trichlorosilane vapour). The stamp is activated in a 1 mbar oxygen plasma 15 s before inking.

**Inking, printing and loading of Pd<sup>2+</sup> Catalyst.** G4OH dendrimer molecules (Aldrich) are dissolved in 99.8% ethanol (Roth) with concentrations from 2 μM to 0.2 mM as ink solutions. For ellipsometric measurements, the direct printing technique is employed: freshly activated flat stamps are covered with one drop (20 μL) of ink solution for 25s, and then blown dry with argon. The stamp is brought in conformal contact with a freshly cleaned Si wafer for 10-120 s and peeled off from the substrate. To check the possible distribution and density of catalytic metal nanoparticles on the surface: 40 μL of 0.06 M CuSO<sub>4</sub> (Aldrich) aqueous solution is put on the printed substrate 5 min for binding. Then bound Cu<sup>2+</sup> ions are reduced to copper nanoparticles using NaBH<sub>4</sub> (Fluka) aqueous solution. After rinsing, a HAuCl<sub>4</sub> (Aldrich) aqueous solution is put on the substrate to obtain gold nanoparticles via a displacement reaction ( $\text{Cu}(0) + \text{Au}^{3+} \rightarrow \text{Au}(0) + \text{Cu}^{2+}$ ). For ELD experiments, contact-inking with a flat inker pad is used in order to avoid edge accumulation (see Fig. 2.2). One drop of an aqueous solution containing 0.36 mM Na<sub>2</sub>PdCl<sub>4</sub> (Aldrich), 0.1 M NaCl (Fluka) and 0.01 M 2-morpholinoethanesulfonic acid (MES, pH= 4.9, Aldrich) as a buffer [Dressick94] is put on the printed substrate for 5 to 15 min, then the substrate is rinsed with water several times.

**Electroless cobalt deposition.** The metallization solution is prepared immediately prior to use by mixing three parts of cobalt stock solution, two parts of reductant and five parts

of water. The stock solution is prepared by adjusting a 100 ml aqueous solution of 1 g  $\text{NH}_4\text{Cl}$  (Fluka), 0.6g  $\text{CoCl}_2$  (Fluka), and 0.8 g of  $\text{Na}_2\text{EDTA}$  (Aldrich) to  $\text{pH} = 7$  with 2 M  $\text{NaOH}$  (Fluka). The reductant consisted of a solution of 1.7 g of dimethylamineborane (DMAB, Aldrich) in 50 ml water [Kind98]. The patterned substrate is put in an argon-bubbled cobalt bath at 310 K for 1 to 3 min to obtain a metallic film.

**Instrumentation.** Ellipsometric measurements are performed in air with an EL X-02C ellipsometer (DRE, Ratzeburg) at  $70^\circ$  angle of incidence and 633 nm wavelength. The ellipticity of the HeNe laser beam is minimized with a  $\lambda/4$  plate. Measurements are made at  $> 4$  points randomly picked across the sample and averaged. A two-layer transparent film model is used for the thickness calculations of dendrimer layers on oxidized silicon wafers. The refractive index of dendrimers is fixed at 1.45 [Chechik99]. AFM images are obtained in IC mode with a Thermomicroscopes Autoprobe M5. Probes are ultrasharp noncontact silicon cantilevers from MikroMarsch or from Nanosensors. Scan rates are changed between 0.5 to 2 Hz according to the scan size. Images include either  $256 \times 256$  or  $512 \times 512$  data points. We use a JSM-6400 Scanning Electron Microscope (SEM).

### 3.3 Printing of G4OH dendrimers

Dendrimers with hydrophilic terminal groups form monolayers on Si surfaces ( $\text{SiO}_2/\text{Si}$ ) via hydrogen bonds since the surfaces contain OH groups. Different from long chain linear molecules, dendrimers of a generation higher than 4 exhibit nearly spherical shapes in solution. When they adsorb on a hydrophilic surface, they become oblate and thus form a film. It is important to note that, although dendrimer layers are closely packed, they are not as dense as those from long chain thiols and siloxanes. For example,

G4NH<sub>2</sub> layers on Au substrates can slow down the rate for the ELD of copper on Au, but they cannot prevent it, while long chain thiol SAMs on Au will suppress copper ELD completely [chapter 2.3, Bittner02]. Dendrimer layers are therefore "active" by both their own functional groups and by allowing other molecules to access the substrate.

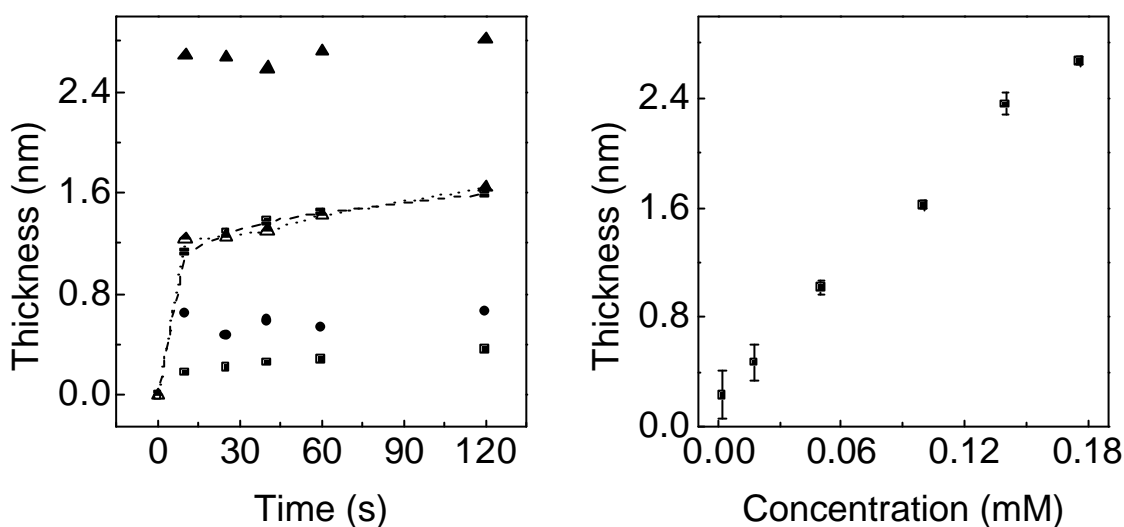


Figure 3.1(left) Ellipsometrically determined thickness of G4OH films on Si wafers. The films are formed by printing or immersion in ethanolic dendrimer solution. For printing with the ink concentrations of 2  $\mu\text{M}$  (solid squares), 17.6  $\mu\text{M}$  (solid circles), and 176  $\mu\text{M}$  (solid triangles) an inking time of 25 s is used. For the adsorption 2  $\mu\text{M}$  (half empty squares + dot line) and 176  $\mu\text{M}$  (half empty triangles + dash line) solutions are employed.

Figure 3.1(right) Relation between the layer thickness and the ink concentration (inking time 25 s, printing time 25 s).

Optical ellipsometry is a convenient technique for measuring the thickness of very thin layers and has been used extensively to study the nature of SAMs. The exact calculation of the thickness of dendrimer layers needs to consider the voids unoccupied by dendrimers as discussed by Tokuhiya et al. [Tokuhiya99]. Since our main concern is

the nominal mass coverage of dendrimers (not the actual thickness of the monolayer or the molecules), we use the simple two-layer model (dendrimer/SiO<sub>2</sub>) to obtain the thickness of a dendrimer layer. Although this model is not exact, the thus measured thickness of a G4OH monolayer – prepared by adsorption from solution - shows a good agreement with the thickness obtained by X-ray reflectivity and atomic force microscopy measurement [Tsukruk97]. This indicates that our simple model still is a good approximation. Fig. 3.1(left) shows the relation between the average (nominal) layer thickness and the printing (or immersion) time. In the case of  $\mu$ CP, we employ flat stamps instead of patterned ones in order to avoid measuring uncovered regions of the wafer. For the solution adsorption process, the concentrations of G4OH have no obvious effect on the thickness of the layers. The layers rapidly reach the thickness of G4 dendrimer monolayers,  $(1.4 \pm 0.4)$  nm [Tsukruk97]. In contrast, the concentrations of the G4OH ink have a large effect on the thickness of printed layers. It increases from 0.25 nm for 2  $\mu$ M ink concentration to 2.8 nm for 0.18 mM. On the other hand, the printing time has no obvious effect. This is different from printing thiols and chlorosilanes, which show an obvious increase of printed SAM thickness with contact time [Delamarche98, Finnie00]. Thus we can shorten printing times to decrease the lateral diffusion in the case of very small pattern sizes.

Fig. 3.1(right) further details the change of the thickness with increasing ink concentration. It shows a linear correlation with the ink concentration. This indicates that the mass coverage of dendrimers can be tuned through the control of dendrimer concentration. This dependence of the printed thickness on ink concentration exists for thiol and chlorosilane systems as well, but a nonlinear increase of SAM thickness with

ink concentration was observed for these two systems [Delamarche98, Finnie00]. For printing thiols, normally a monolayer is obtained [Delamarche98] while in the case of chlorosilane multilayers are easily produced [Jeon97]. Since the assembly process of chlorosilane molecules is based on hydrolysis and condensation reactions, they can easily form three-dimensional networks via self-condensation. Such networks have been used as resist layers for etching processes since printed monolayers of octadecyltrichlorosilane cannot protect a Si wafer effectively [John96, Wang96]. G4OH dendrimers have 64 terminal hydroxyl groups. They adsorb on hydrophilic oxide surfaces via hydrogen bonds, i.e., without a chemical reaction. They can also adsorb onto a thus formed monolayer. Therefore it is not surprising that we printed multilayers at high ink concentrations.

In order to check the distribution and density of metallic nanoparticles on these printed surfaces, we deposit gold nanoparticles on these surfaces. Considering the difference in binding affinity of  $\text{Au}^{3+}$  ions and  $\text{Cu}^{2+}$  ions to the tertiary N of G4OH molecules, we first bind the latter to the printed G4OH molecules and reduce them to copper nanoparticles. Gold nanoparticles are obtained through a displacement reaction of  $\text{Au}^{3+}$  ions with copper (0) nanoparticles.

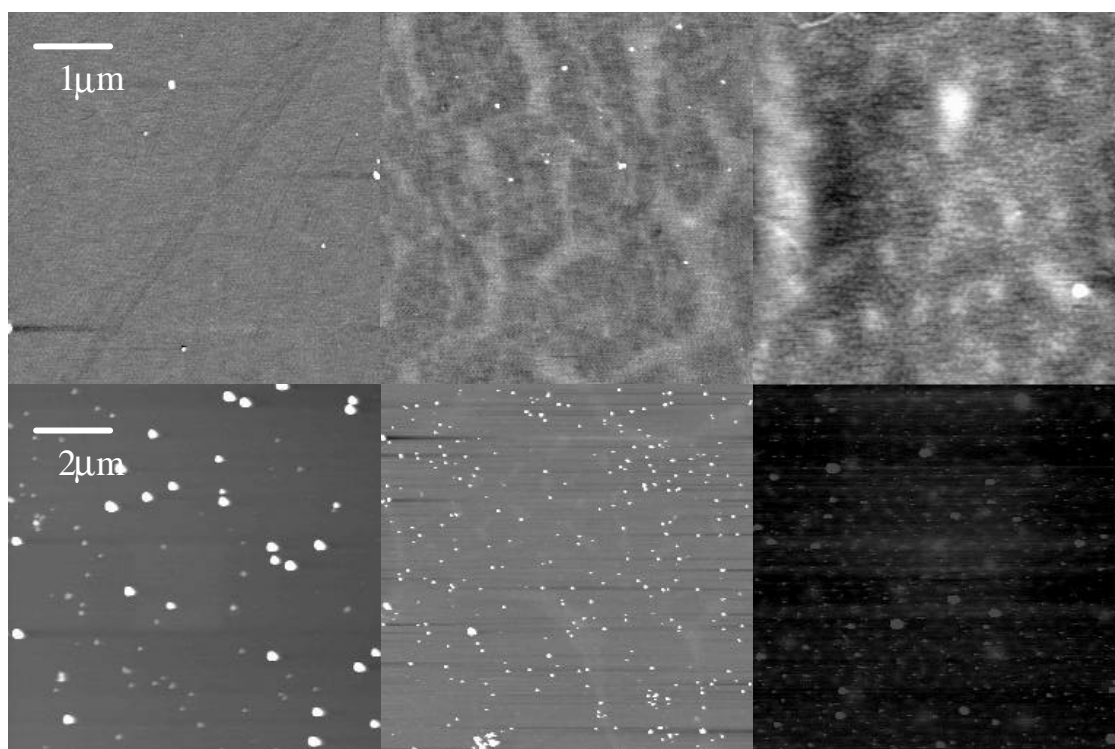


Figure 3.2 Topographic IC-AFM images of printed G4OH on Si wafers (upper parts) and of Au particles formed on these surfaces after adsorption of metal ions and reduction (lower parts). From left to right: printing ink concentrations: 17.6  $\mu\text{M}$ , 50  $\mu\text{M}$  and 100  $\mu\text{M}$  of G4OH in ethanol.

In Fig. 3.2 upper parts, topographic images of the printed G4OH layers with different ink concentrations are shown. Increasing the ink concentrations, the amount of G4OH molecules on the surface also increases and some structures appear at higher ink concentrations. After the formation of gold nanoparticles, many white dots appear on the surface (Fig. 3.2 lower parts). The density of the particles increases with increasing ink concentration. This agrees with that more G4OH molecules are printed on the surface at the higher ink concentration and that G4OH molecules supply the binding sites for metal ions. The sizes of formed gold nanoparticles can be roughly divided into two groups: big ones and small ones. For the lower ink concentration, many big particles appear. At a

medium ink concentration, smaller particles dominate. At the higher ink concentration, also smaller particles dominate. But the number of large particles also increases due to the increased disorder by more than one layer of G4OH molecules. From the viewpoint of size distribution, medium ink concentration gives best results. The size of smaller gold nanoparticles decreases with increasing ink concentrations. This might suggest that a large amount of G4OH molecules (either by roughness or by steric hindrance) at higher ink concentrations limits the mobility of formed gold nanoparticles and thus diffusion-induced growth is reduced.

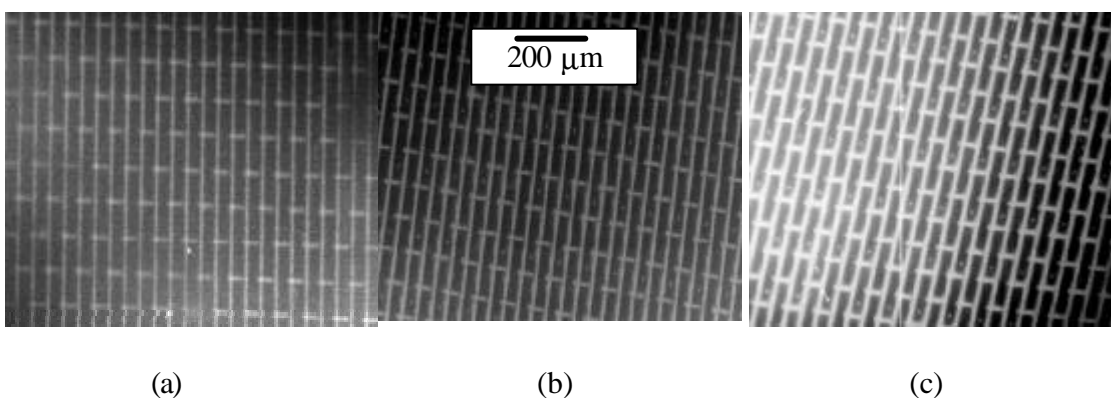


Figure 3.3 Electron microscopy micrographs of printed G4OH patterns on Si wafers. Printing ink concentrations: 2  $\mu\text{M}$  (a), 50  $\mu\text{M}$  (b) and 100  $\mu\text{M}$  (c) G4OH in ethanol. The patterns are 8  $\mu\text{m}$  wide structures separated by 50  $\mu\text{m}$  spaces.

Fig. 3.3 presents SEM micrographs of patterned G4OH layers at three different concentrations. With increasing concentration the printed pattern size will gradually increase. This undesired concentration "widening" of lines and pixels exists also for thiols and chlorosilanes [Delamarche98, Finnie00]. Although lateral diffusion of G4OH



molecules on the surface should be much less than small thiols and chlorosilane molecules due to their large molecular weight (14279 g/mol), it seems that it is also unavoidable at higher ink concentrations. Therefore an optimization of the ink concentration is required. In our case, the best ink concentration is in the range of several  $\mu\text{M}$  of G4OH. Fig. 3.4 shows an AFM image of 600 nm wide linear patterns, printed with 2  $\mu\text{M}$  G4OH in ethanol. It indicates that pattern sizes can easily be reduced down to several hundred nanometers. For printing flat stamp, we obtain submonolayer coverage of G4OH molecules on the surface as shown in Fig. 3.1. However, for printing structural stamps with small features, monolayer coverage of G4OH molecules is reached. This difference in coverage in printing small- and large-area patterns under the same conditions has been discussed by Delamarche et al. [Delamarche98].

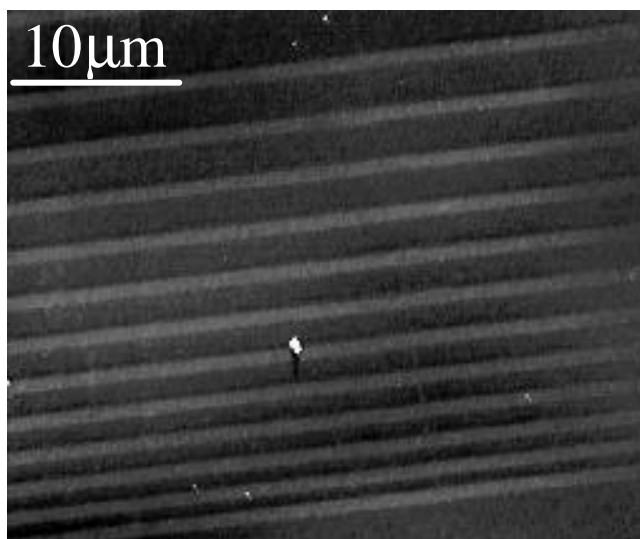


Figure 3.4 Topographic AFM image of 600 nm linear dendrimer patterns on a Si wafer, obtained in intermittent contact mode (ink concentration: 2 $\mu\text{M}$  G4OH in ethanol; inking time: 25 s; printing time: 25 s).

### **3.4 Binding of Pd<sup>2+</sup> ions and ELD of cobalt layers**

Pd<sup>2+</sup> ions in buffered fresh solutions of pH = 5 (see chapter 3.2) can easily bind to the thus obtained G4OH dendrimer patterns. After washing and immersion of the palladium-treated sample in a cobalt ELD bath (see chapter 3.2), a cobalt pattern will form selectively on the printed dendrimer layer. Fig. 3.5 shows a topographic IC-AFM image of a 700 nm wide cobalt line pattern produced in this way. The average height of the Co pattern is ~ 80 nm. A zoom-in (see inset of Fig. 3.5) provides details of the Co structure, presumably grains and grain boundaries. We found that the inked stamp could be used several times without re-inking. In addition to being highly relevant to applications, this leaves space for a further decrease of the ink concentration for even smaller pattern sizes.

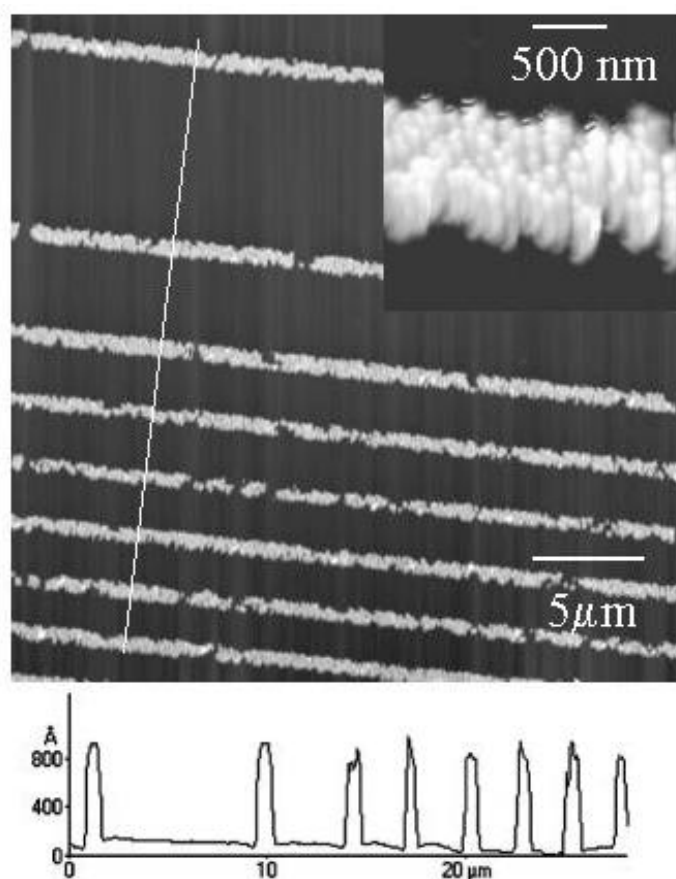


Figure 3.5 Topographic IC-AFM image of cobalt metal patterns. A cobalt ion - borane electroless deposition bath was applied to a chloropalladate-treated dendrimer pattern (ink concentration 2  $\mu\text{M}$  in ethanol, inking time 25 s, printing time 25 s) on a Si wafer surface (inset: zoom-in scan).

Apart from the optimization of the G4OH ink concentration, another vital factor for the successful fabrication of the cobalt pattern is the effective binding between G4OH and  $\text{Pd}^{2+}$  ions. Each G4OH molecule has 62 tertiary amine and 124 amide groups which both can bind  $\text{Pd}^{2+}$  ions while the 64 hydroxyl groups are relatively weak ligands. The ability of G4OH dendrimers to complex  $\text{Pd}^{2+}$  from solution requires that the amine groups are available to the solution species and that  $\text{Pd}^{2+}$  possesses at least one sufficiently labile coordination site.

Cl<sup>-</sup> is a labile coordination site in Pd<sup>2+</sup> halogen complexes, thus the chemistry of Pd<sup>2+</sup> halogen complexes in aqueous solution is dominated by hydrolysis above pH ~2. However, at pH = 1 and high chloride concentrations (0.7 M), PdCl<sub>4</sub><sup>2-</sup> solutions contain >80% of PdCl<sub>4</sub><sup>2-</sup> (sufficient labile coordination sites for amines) which is now stable against hydrolysis; palladium particles produced from these solutions on amine-terminated monolayers are catalysts for the growth of small cobalt islands [Kind98]. However, in our case no growth of cobalt layers was observed when we treated dendrimer patterns with this solution and tried to deposit cobalt from the cobalt ELD bath. A possible reason is the partial protonation of the amine groups in the dendrimer. Protonated amines can still complex Pd<sup>2+</sup> (amine complexes can be synthesized in good yield at low pH), but (de)protonation of a macromolecule leads to multiple interconnected equilibria. This could result in binding very few Pd<sup>2+</sup> ions to G4OH molecules. Pd particles formed after reduction may be too few to catalyze the formation of complete cobalt layers.

A fresh Pd<sup>2+</sup> solution with 0.1 M Cl<sup>-</sup> and pH=5, prepared according to the recipe of Dressick et al. [Dressick94], has a rather low PdCl<sub>4</sub><sup>2-</sup> concentration (<20%) compared with the above-mentioned 80%. But still the overall amount of chloropalladate species PdCl<sub>n</sub>(H<sub>2</sub>O)<sub>4-n</sub><sup>2-n</sup> (n>0) is over 90% since the hydrolysis - finally yielding Pd(H<sub>2</sub>O)<sub>4</sub><sup>2+</sup> - is slow. More important, amine groups in dendrimers are deprotonated at pH = 5. Employing this solution led to cobalt growth from the ELD bath, indicating a successful complexation of Pd<sup>2+</sup> ions within the dendrimer. Since amide groups are neither protonated nor deprotonated in the investigated pH range, we can speculate that only the tertiary amine groups bind substantial amounts of Pd<sup>2+</sup>.

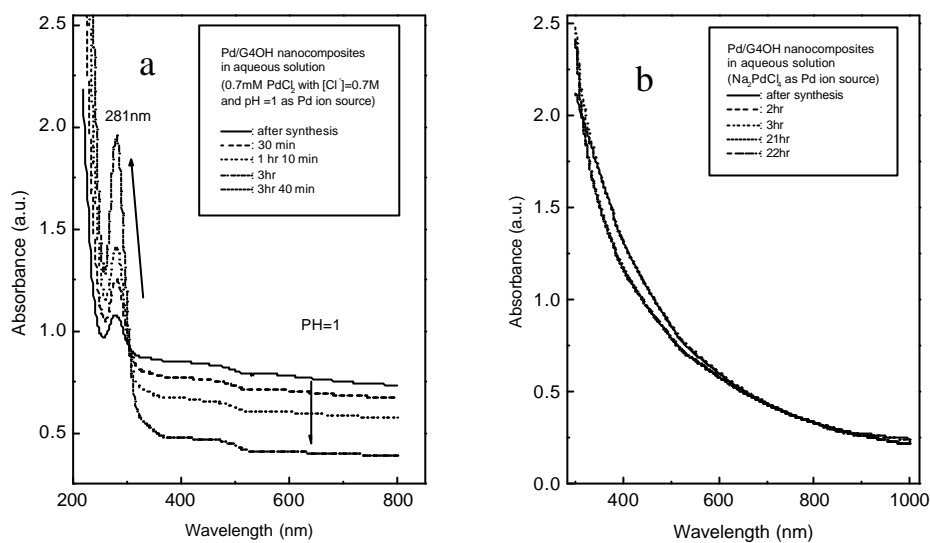


Figure 3.6 UV/visible absorption spectra of Pd/G4OH nanocomposites ( $\text{Pd}^{2+}/\text{G4OH} = 10/1$  and 0.16 M of G4OH) in aqueous solution synthesized at pH = 1 (a) and pH = 5 (b).

The above assumption has been partially verified by comparing the UV/visible absorption spectra of Pd/G4OH nanocomposites synthesized at PH 1 and 5, respectively. At pH = 1, Pd nanoparticles can be formed. However, the size and the morphology are less defined (smooth absorbance change at 400 ~ 800 nm). Pd nanoparticles are unstable. Their absorption decreases with time while the absorption of  $\text{Pd}^{2+}$  ions (284 nm) increases simultaneously. This is because Pd(0) can be oxidized by dissolved  $\text{O}_2$  under acid conditions [Carvalho02]. In contrast, Pd nanoparticles synthesized at pH 5 show well-defined morphology (steep increase in absorbance at 400 ~ 800 nm) and high stability.

Oxide surfaces can be patterned with a combination of  $\mu\text{CP}$  of functional molecules or particles with ELD [Hidber96, Kind00b], but the necessary methods rely on rather complex steps (surface modification, preparation of Pd complexes) compared with the simple method we present here. In our case, all surfaces with hydroxyl groups like

glass, mica and other oxide surfaces should be suitable, generally speaking all surfaces that can form hydrogen bonds with dendrimers. In contrast to printing catalysts, printing dendrimers means patterning a surface with a functional host molecule. Therefore, other functional molecules and particles that can bind to dendrimers can easily be connected to the patterned regions.

### 3.5 Conclusions

Compared with printing other functional molecules, the dendrimer printing method that we present here has the following advantages.

- (1) The requirement of special conditions such as absence of water and oxygen during microcontact printing is not as stringent as in the case of chlorosilanes. Even more important, the solvents for dendrimers are alcohols that cause only a negligible swell of the polymeric stamps. Therefore, dendrimers can be a good replacement for chlorosilanes in small pattern sizes (e.g.  $< 1 \mu\text{m}$ ).
- (2) Many dendrimers are commercially available and quite stable. A range of metals can be synthesized inside (or at) dendrimers via either direct adsorption/reduction synthesis or via displacement with other metals [Zhao99b]. Even semiconductors and dyes can be combined with dendrimers [Sooklal98, Chechik00]. Although our technique relies on the printing of molecules with only three rather simple chemical functionalities, many molecules with more complex chemical groups and even nanoparticles can easily be trapped inside or bound at dendrimers. The wide chemical and structural variability of dendrimers makes these cage-like molecules good carriers or hosts for other functional materials. We infer that the simple procedure of  $\mu\text{CP}$  of dendrimers will allow the patterning of surfaces with such materials.

(3) We showed that arbitrary submicrometric metallic patterns can be formed with high spatial selectivity on nonconducting surfaces, based on very simple wet chemical processes.





## Chapter 4

### **Synthesis, Structure and Optical Properties of CdS/**

### **Dendrimer Nanocomposites**

In chapter 3, G4OH molecules are first printed on a surface; metal ions are then bound to them. This means that the morphology of the printed dendrimers will influence the growth of metal nanoparticles in a subsequent reduction step. A problem is that the morphology of printed dendrimers is much more difficult to control than their morphology in solution. The size distribution of metal nanoparticles from the former is therefore larger than that from solution synthesis (Fig. 3.2). This might not influence the electroless deposition of thick layers much since the size distribution of nuclei does not play a critical role in this process. But it may play a very important role in other processes. For example, photoluminescence (PL) from semiconductor nanoparticles is highly sensitive to the size distribution. A large size distribution means a low degree of color purity. Is it possible to directly print dendrimer-stabilized nanoparticles synthesized in solution with good control of experimental conditions? We will address this in two chapters. This chapter demonstrates the first step: we explore the solution synthesis, morphology and PL properties of dendrimer-stabilized CdS nanoparticles.

## 4.1 Introduction

Semiconductor nanoparticles show unique size-dependent optical properties and are of great interest for applications in optoelectronics and photovoltaic devices [Henglein88, Bawendi90]. Up to now, various chemical synthetic methods have been developed to prepare nanoparticles. Generally speaking, the syntheses of semiconductor nanoparticles are realized under the protection of various stabilizers. The stabilizers can be divided into two classes: simple ligands and nanocages.

In the first case, ligands cap the surface of nanoparticles during their growth and thus stabilize them. Two quite different methods have been developed to synthesize high-quality semiconductor nanoparticles. One is an organometallic synthesis based on the high-temperature thermolysis of the precursors, which was first reported by Murray et al. in 1993 [Murray93]. It has been further improved since then [Peng97, PengZ01, PengZ02]. Another synthesis is performed in an aqueous medium using polyphosphates [Spanhel87] or thiols [Vossmeier94, Gaponik02] as stabilizing agents. The disadvantage for these two methods is that the deposition of nanoparticles on surfaces often requires ligand exchange interactions [Vossmeier98] or further modifications of the surface of the nanoparticles [Rogach00]. Concerning nanocages, various cage-shaped functional materials such as reverse micelles [Pileni00], diblock copolymers [ZhaoH01], vesicles [Zhou93] etc. are used as nanoreactors to control the growth of nanoparticles. Recently, biomaterials have also been reported to be nanotemplates for nanoparticles [Douglas98, Braun98, Mertig98, Shenton98, Knez02, WangQ02].

PAMAM dendrimers, first synthesized by Tomalia in 1985, have been found to be good nanoreactors for the formation of metal nanoparticles [Balogh98, Zhao98a]. Using

them as nanoreactors for semiconductor and oxide nanoparticles has also been reported recently [Sooklal98, Huang99, Tan99, Lemon00, Strable01]. Most important, through the control of terminal groups, dendrimers can form layers on various surfaces via electrostatic forces, hydrogen bonds, van der Waals forces, metal-ligand interactions etc. [Tsukruk97, Lackowski99, Zhang02]. This makes the immobilization of nanoparticle/dendrimer composites on surfaces much simpler than other synthetic methods. In addition, as shown in the previous chapter that dendrimers can be patterned on surfaces with the microcontact printing technique [Wu02, see chapter 3]. This makes the patterning of nanoparticle/dendrimer composites very simple. CdS nanoparticles have been prepared in various media and studied widely [Youn88, Haesselbarth93, Mews94, Mews96, Cizeron97, Carrot99]. For the convenience of comparison, in this chapter we use CdS as a model nano-guest and explore the potential of dendrimers as nanoreactor-hosts for semiconductors.

## 4.2 Experimental

**Chemicals:** Amine-terminated, generation 8 polyamidoamine (PAMAM) starburst dendrimers (8.07% w/w in methanol) are from Dendritech. Inc. (here referred to as G8NH<sub>2</sub>). G4NH<sub>2</sub> (10 % w/w in methanol), G4OH (10 % w/w in methanol), Cd(CH<sub>3</sub>COO)<sub>2</sub>, Pb(CH<sub>3</sub>COO)<sub>2</sub>, Zn(CH<sub>3</sub>COO)<sub>2</sub>, hexadecylamine (C<sub>16</sub>H<sub>33</sub>NH<sub>2</sub>), and Na<sub>2</sub>S are from Aldrich and used as received (p.a.). Dodecanethiol (C<sub>12</sub>H<sub>25</sub>SH, p.a.) is from Sigma. Methanol, NaOH (p.a.) is from Merck.

**Preparation of CdS/G8NH<sub>2</sub> nanocomposites in methanol.** Methanolic Cd<sup>2+</sup>, S<sup>2-</sup> and G8NH<sub>2</sub> are mixed at room temperature under an argon atmosphere to obtain CdS/G8NH<sub>2</sub>

nanocomposites. A typical preparation of CdS/G8NH<sub>2</sub> nanocomposites with an initial Cd/S molar ratio of 1/1 is as follows: 50  $\mu$ L G8NH<sub>2</sub> is diluted with methanol to 2.5 ml (5.5  $\mu$ M G8NH<sub>2</sub>), then 2.5 ml of 2 mM Cd(CH<sub>3</sub>COO)<sub>2</sub> and 2.5 ml of 2 mM Na<sub>2</sub>S in methanol are added to the dendrimer solution sequentially. The ratio of Cd<sup>2+</sup>/G8NH<sub>2</sub> corresponds here to 360 Cd<sup>2+</sup> ions per dendrimer. The number of primary amine groups in each G8NH<sub>2</sub> is 1024. This corresponds to more than two NH<sub>2</sub> groups for each Cd<sup>2+</sup> without considering protonation of NH<sub>2</sub> groups. The initial Cd/NH<sub>2</sub> ratio is kept identical for all the experiments in this chapter.

**Instruments.** UV/Vis absorption spectra are obtained with a Perkin Elmer Lambda 2 in the wavelength range of 200 - 650 nm. Photoluminescence and Excitation spectra are taken with a Perkin Elmer LS 50B. For the time-resolved measurements the pulsed output of a frequency-doubled titanium-sapphire laser (370 nm, 150 fs, 76 MHz) is used for sample excitation. The photoluminescence signal is spectrally dispersed by a monochromator and temporally resolved by a streak camera system (Hamamatsu). The time resolution of the system is 10 ps.

### **4.3 Effects of Cd<sup>2+</sup>/G8NH<sub>2</sub> and Cd<sup>2+</sup>/S<sup>2-</sup> ratios on the formation of CdS nanoparticles**

PAMAM dendrimers have three types of amine groups, NH<sub>2</sub>, NR<sub>3</sub>, and CONHR (R is a linear hydrocarbon chain, see Fig. 2.9 for their structures). Their binding ability to metal ions is expected to follow the trend NH<sub>2</sub> > NR<sub>3</sub> > CONHR [Ottaviani97,

Guilbault72]. Unlike  $\text{Cu}^{2+}$ ,  $\text{Pd}^{2+}$  ions etc., the binding of  $\text{Cd}^{2+}$  ions to N groups does not show any new features in UV/Vis absorption spectra as shown in Fig. 2.12 of Chapter 2. This excludes the possibility of controlling the loading factor of  $\text{Cd}^{2+}$  to dendrimers by a simple spectroscopic titration. Due to this, we evaluate the loading factor by monitoring the formation of CdS nanoparticles. Assuming amine groups as primary binding sites for  $\text{Cd}^{2+}$  ions and two N groups per  $\text{Cd}^{2+}$  ion, we cover the range of  $\text{Cd}^{2+}/\text{N}$  ratios from  $\text{Cd}^{2+}$  binding only  $\text{NH}_2$  groups (512  $\text{Cd}^{2+}/\text{G8NH}_2$ ), over  $\text{Cd}^{2+}$  binding  $\text{NH}_2$  and the outermost shell of  $\text{NR}_3$  (768  $\text{Cd}^{2+}/\text{G8NH}_2$ ),  $\text{Cd}^{2+}$  binding  $\text{NH}_2$  and all  $\text{NR}_3$  groups (1023  $\text{Cd}^{2+}/\text{G8NH}_2$ ), to  $\text{Cd}^{2+}$  binding  $\text{NH}_2$ , total  $\text{NR}_3$  groups, and a part of the CONHR groups (1535  $\text{Cd}^{2+}/\text{G8NH}_2$ ). This is obtained by fixing the amount of  $\text{Cd}^{2+}$  ions and by decreasing that of  $\text{G8NH}_2$ . It is found that the latter three cases do not give stable colloidal solutions. They either yield precipitates immediately after the reaction or after one day of room temperature storage. Only the first case results in stable colloidal solutions. This suggests that  $\text{Cd}^{2+}$  ions mainly interact with  $\text{NH}_2$  terminal groups. Upon increasing the concentration of  $\text{G8NH}_2$ , the size of CdS nanoparticles decreases since the number of  $\text{Cd}^{2+}$  ions per  $\text{G8NH}_2$  decreases. Therefore, we keep the  $\text{NH}_2/\text{Cd}^{2+}$  ratio at  $< 2$ .

Apart from the loading factor of  $\text{Cd}^{2+}$  in  $\text{G8NH}_2$ , the  $\text{Cd}^{2+}/\text{S}^{2-}$  ratio is also an important factor since it can affect the growth behavior of nanoparticles and thus further influence their properties. We keep the amount of  $\text{Cd}^{2+}$  ions constant and change  $\text{Cd}^{2+}/\text{S}^{2-}$  ratios by increasing the concentration of  $\text{S}^{2-}$  ions. We choose three different  $\text{Cd}^{2+}/\text{S}^{2-}$  ratios, 3/1, 1/1, and 1/2. The absorption spectra and PL spectra are shown in Fig. 4.1. From formula 2.1, we know that with decreasing particle size, the band gap increases. From the  $\text{Cd}^{2+}/\text{S}^{2-}$  ratio of 3/1 to 1/1, the band gap redshifts, indicating an increase in

size. From 1/1 to 1/2, particle size does not increase since excess  $S^{2-}$  ions have no more  $Cd^{2+}$  ions to bind. All three samples show blue PL. With increasing particles size, the PL redshifts.

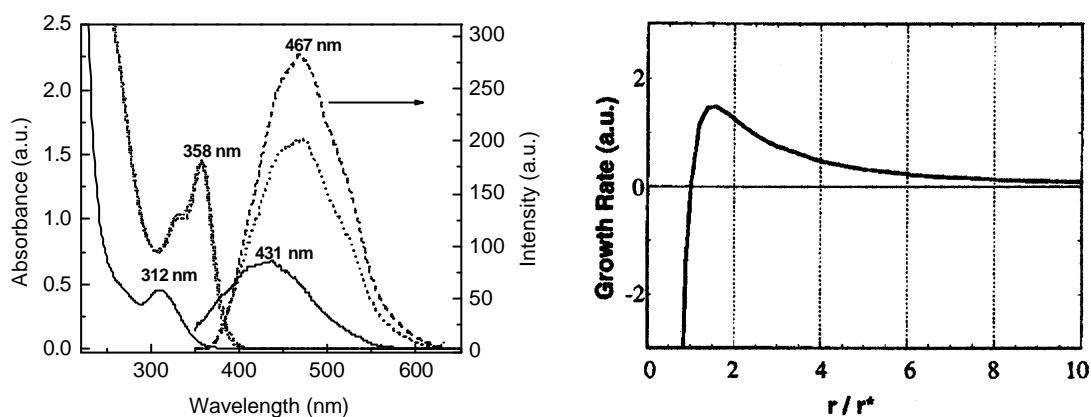


Figure 4.1 Absorption and PL spectra of CdS/G8NH<sub>2</sub> nanocomposites in methanol with  $Cd^{2+}/S^{2-}$  ratios of 3/1 (solid line), of 1/1 (dashed line) and of 1/2 (dotted line). Measurements are done after 1 h RT aging.  $\lambda_{ex}=320$  nm for PL.

Figure 4.2 Variation of growth rates with crystal sizes according to model of Sugimoto [Peng98]

## 4.4 Room temperature growth of CdS/dendrimer nanocomposites

It is found that the prepared CdS/dendrimers nanocomposites undergo further growth when stored at room temperature (RT). In order to hinder this process, samples are stored in a  $-35^{\circ}C$  freezer after synthesis. At this storage temperature, they do not show obvious growth. Reiss demonstrated theoretically that diffusion-limited growth could lead to narrowing of size distribution with time by considering diffusion area vs.

size [Reiss51]. This has recently been explored by Peng et al. to control the size distribution of semiconductor nanocrystals synthesized by wet chemistry [Peng98]. Diffusion controlled growth rate of the particle with size  $r$  is shown in Fig 4.2 [Peng98]. In this picture, at any given monomer (composition species, but not in the form of nanocrystals) concentration, there exists a critical size,  $r^*$ , which is at equilibrium (growth rate = 0). Nanocrystals smaller than the critical size have negative growth rates (dissolve), while larger ones grow at rates strongly dependent on size. Narrowing of the size distribution occurs when nanocrystals present in solution are all slightly larger than the critical size. Under these conditions, the smaller nanocrystals in the distribution grow faster than the larger ones. When the monomer concentration is depleted due to the growth, the critical size becomes larger than the average size present, and the distribution broadens because some smaller nanocrystals are shrinking and eventually disappear, while larger ones are still growing. This is Ostwald ripening.

The RT growth of CdS nanoparticles here can be explained by this growth rate curve. In Figure 4.3, CdS nanoparticles with an initial  $\text{Cd}^{2+}/\text{S}^{2-}$  ratio of 1/1 show no redshift of the band gap but a narrowing of absorption structures upon RT aging. This is due to the narrowing growth. CdS nanoparticles with initial  $\text{Cd}^{2+}/\text{S}^{2-}$  ratios of 3/1 and 1/2, on the other hand, show a narrowing of the absorption structures at short aging times and gradual redshift of band gaps at longer aging times. The later stage reflects a Ostwald ripening growth.

For direct band gap semiconductors, the band gap can be deduced from the equation [Ingrt99]:

$$\sigma h\nu = (h\nu - E_g)^{1/2} \quad (4.1)$$

$\sigma$ ,  $h\nu$  and  $E_g$  are the extinction coefficient, the energy of the radiation used and the band gap energy, respectively.  $(\sigma h\nu)^2$  vs.  $h\nu$  shows a straight line. The intersection of the straight line with  $h\nu$  axis gives  $E_g$ . Here we use absorbance ( $A$ ) from Fig. 4.3 as  $\sigma$  ( $A = \sigma lC$ ,  $l$  is optical path length;  $C$  is the concentration of the nanoparticle). The thus obtained band gaps versus RT aging times are shown in Figure 4.4b. During 6 day RT storage, CdS nanoparticles with the initial  $\text{Cd}^{2+}/\text{S}^{2-}$  ratio of 1/1 show no increase in particle size while those with the initial  $\text{Cd}^{2+}/\text{S}^{2-}$  ratios of 3/1 and 1/2 show an obvious increase in particle size. This means that CdS nanoparticles of stoichiometric ratio have a longer narrowing growth time than those of nonstoichiometric ratios. Note that the large variation in growth (both the narrowing of size distributions and the redshift of band gaps) happens mainly within one day. Therefore RT growth can be divided into two stages: a fast one, within one day, due to narrowing growth and a slow one due to Ostwald ripening growth. The control of the growth behavior has been used by Peng et al. to obtain II-VI and III-V nanoparticles with a narrow size distribution [Peng98]. From the viewpoint of keeping a narrow size distribution, CdS nanoparticles should be synthesized with a stoichiometric ratio (Fig. 4.4b). For CdS nanoparticles with an initial  $\text{Cd}^{2+}/\text{S}^{2-}$  ratio of 3/1, from the viewpoint of PL (Fig. 4.4a), this growth process is also an effective RT annealing process since the PL efficiency increases greatly. The PL efficiency can increase up to ten-fold (Fig. 4.4b). The PL efficiencies for the samples with initial  $\text{Cd}^{2+}/\text{S}^{2-}$  ratios of 1/1 and 1/2 also increase, but with less than two-fold.



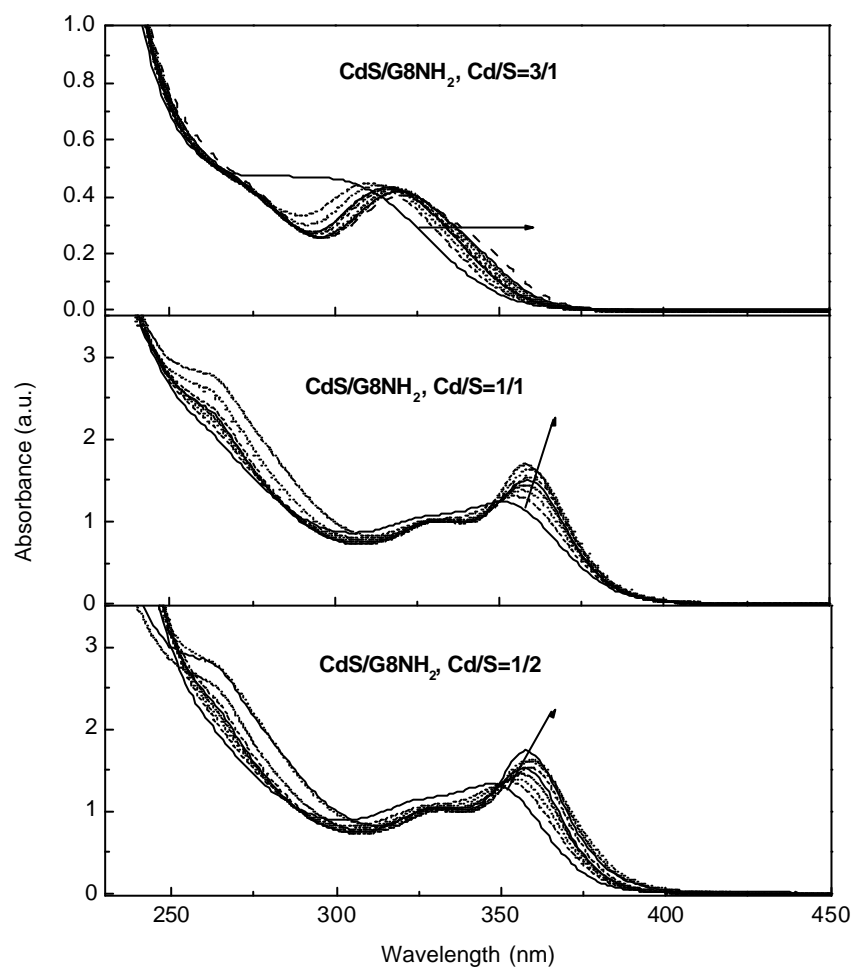


Figure 4.3 Evolution of absorption spectra of CdS/G8NH<sub>2</sub> nanocomposites in methanol upon RT storage with Cd/S ratios of 3/1: 0 min, 1h10 min, 2 h 10 min, 3 h 55 min, 5 h, 6 h, 17 h, 1 d, 3 d, and 6 d, and of 1/1 and 1/2: 0 min, 10 min, 30 min, 1 h 10 min, 3 h 15 min, 5 h 39 min, 2 d, 6 d, and 7 d. Arrows indicate the directions of spectral changes.

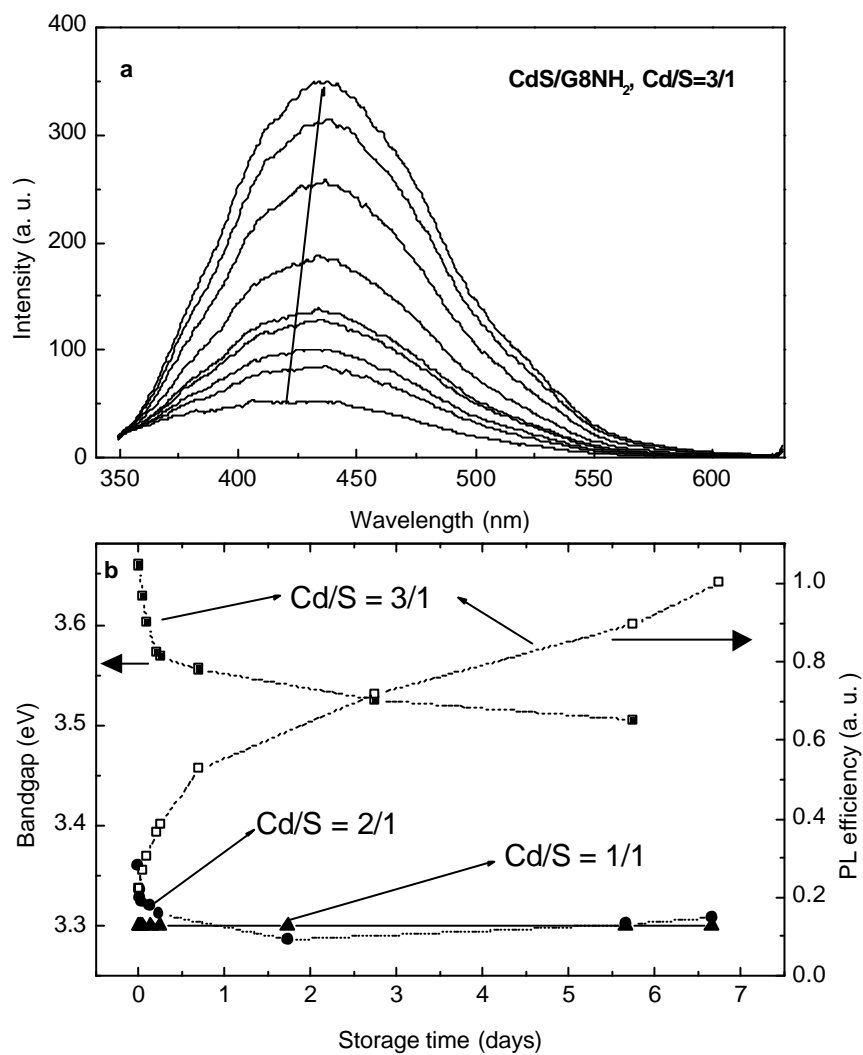


Figure 4.4a Corresponding time evolutions of PL spectra for the sample with the Cd/S ratio of 3/1. Times are shown in Fig. 4.3.

Figure 4.4b Band gaps vs. RT aging times with Cd/S ratios of 3/1, 1/1, and 1/2; PL efficiency versus RT aging times for the sample with the Cd/S ratio of 3/1.

## 4.5 Effects of adding organic additives to CdS/G8NH<sub>2</sub> nanocomposites

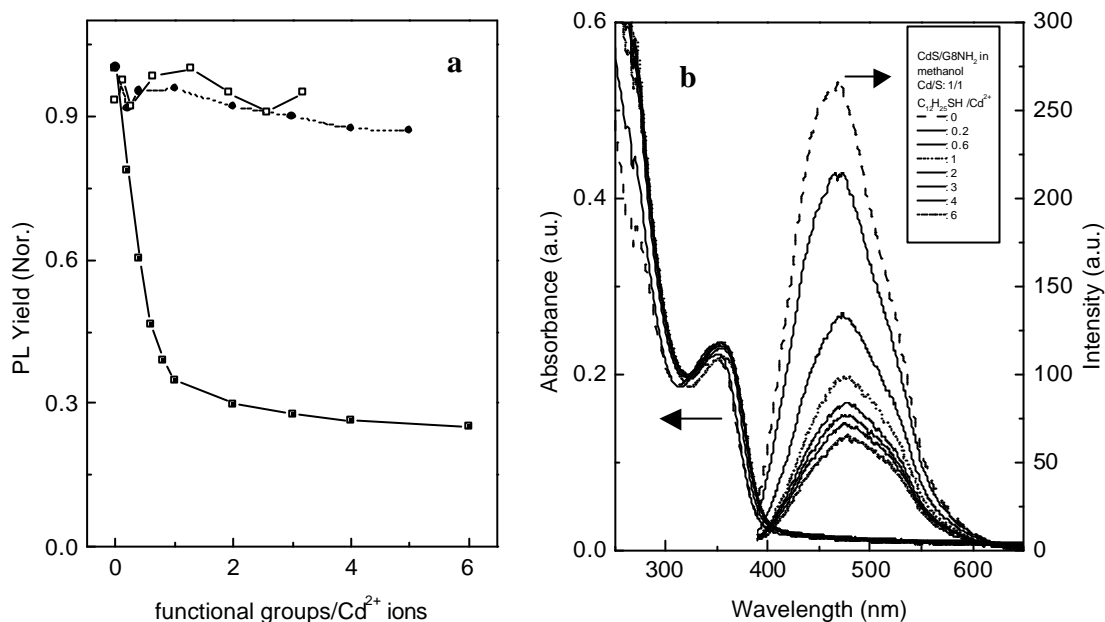


Figure 4.5a Dependence of the PL efficiency in methanol on ratios of functional groups/Cd<sup>2+</sup> ions: 2mM C<sub>12</sub>H<sub>25</sub>SH (solid squares + solid line), 2mM C<sub>16</sub>H<sub>33</sub>NH<sub>2</sub> (solid circles + dashed line), and 10  $\mu$ M G4NH<sub>2</sub> (empty squares + solid line). CdS/G8NH<sub>2</sub> in methanol with an initial Cd/S ratio of 1/1.

Figure 4.5b Evolution of absorption and PL spectra upon adding 2 mM C<sub>12</sub>H<sub>25</sub>SH in methanol.

Here we study the influence of three electron-donating organic additives (C<sub>12</sub>H<sub>25</sub>SH, C<sub>16</sub>H<sub>33</sub>NH<sub>2</sub> and G4NH<sub>2</sub>) on the surface passivation of nanoparticles. C<sub>12</sub>H<sub>25</sub>SH binds strongly to CdS nanoparticles and has been used to replace weakly interacting surfactants on the surface of CdS nanoparticles [Pileni00]. Long chain amines have been used as donors to interact with surface Cd<sup>2+</sup> ions (acceptors) of CdS nanoparticles to further optimize the band gap PL ( $h\nu = E_g$ ) [Peng97]. Figure 4.5a shows

the dependence of the PL efficiency on the ratio of functional groups/ $\text{Cd}^{2+}$  ions. Long chain  $\text{C}_{16}\text{H}_{33}\text{NH}_2$  and  $\text{NH}_2$ -terminated spherical dendrimers have no obvious effect on the blue PL while  $\text{C}_{12}\text{H}_{25}\text{SH}$  quenches the PL efficiently. Figure 4.5b shows evolution of absorption and PL spectra upon adding  $\text{C}_{12}\text{H}_{25}\text{SH}$ . Adding  $\text{C}_{12}\text{H}_{25}\text{SH}$  first leads to a little increase in CdS size, as seen from a small redshift in absorption and in PL. This indicates a little deficiency in actual  $\text{S}^{2-}$  ions amount in solution although we prepare nanoparticles with the  $\text{Cd}^{2+}/\text{S}^{2-}$  ratio of 1/1. After that, the band gap does not change with further adding  $\text{C}_{12}\text{H}_{25}\text{SH}$ .  $\text{C}_{12}\text{H}_{25}\text{SH}$  molecules bind to the surplus  $\text{Cd}^{2+}$  ions on the surface of CdS nanoparticles. This leads to a small increase in CdS size. When the excess  $\text{Cd}^{2+}$  ions are depleted by added  $\text{C}_{12}\text{H}_{25}\text{SH}$ , the size of CdS does not change with further adding  $\text{C}_{12}\text{H}_{25}\text{SH}$ . The variation in PL intensity shows two stages: at the beginning the PL dramatically decreases with adding  $\text{C}_{12}\text{H}_{25}\text{SH}$ . After this stage, adding  $\text{C}_{12}\text{H}_{25}\text{SH}$  has no obvious influence on the PL. The explanation for the PL efficiency is similar:  $\text{C}_{12}\text{H}_{25}\text{SH}$  molecules bound to  $\text{Cd}^{2+}$  ions at the surface of CdS nanoparticles influence the PL while those randomly distributed in solution have no influence.

## **4.6 Effects of adding inorganic ions and the formation of a core-shell structure**

As shown in chapter 4.3, the initial  $\text{Cd}^{2+}/\text{S}^{2-}$  ratios show an obvious influence on the PL. CdS nanoparticles with initial  $\text{Cd}^{2+}/\text{S}^{2-}$  ratios  $< 1/2$  show very weak PL. We now study the effects of adding  $\text{Cd}^{2+}$  or  $\text{S}^{2-}$  ions on the PL of the synthesized CdS.

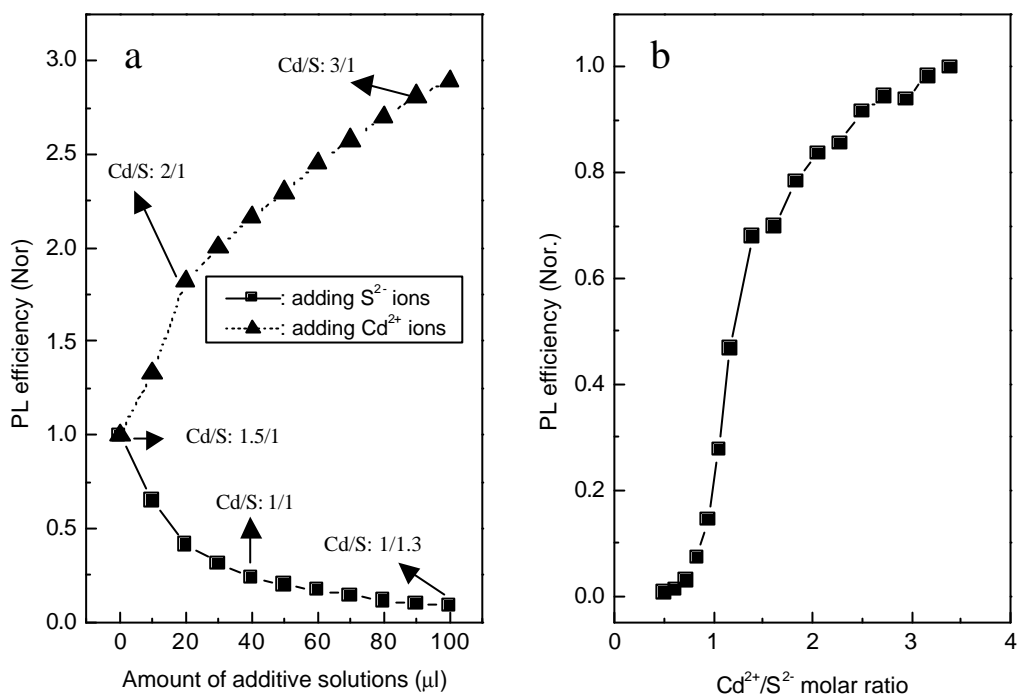


Figure 4.6a Effects of adding  $\text{Cd}^{2+}$  or  $\text{S}^{2-}$  ions (initial ratio of  $\text{Cd}^{2+}/\text{S}^{2-} = 1.5/1$ ) on the PL efficiency. The PL efficiency is normalized with that of  $\text{Cd}^{2+}/\text{S}^{2-} = 1.5/1$ .

Figure 4.6b Dependence of the PL efficiency on  $\text{Cd}^{2+}/\text{S}^{2-}$  ratios (initial ratio of  $\text{Cd}^{2+}/\text{S}^{2-} = 1/2$ ). The PL efficiency is normalized with that of  $\text{Cd}^{2+}/\text{S}^{2-} = 3.5/1$ .

Figure 4.6a shows the variations in the PL efficiency for a sample with an initial  $\text{Cd}^{2+}/\text{S}^{2-}$  ratio of 1.5/1 by adding  $\text{Cd}^{2+}$  ions and  $\text{S}^{2-}$ , respectively. Corresponding  $\text{Cd}^{2+}/\text{S}^{2-}$  ratios after the addition have been marked for some positions. They show opposite effects: adding  $\text{Cd}^{2+}$  increases the PL efficiency while adding  $\text{S}^{2-}$  decreases the PL. In addition, samples with an excess of  $\text{S}^{2-}$  ions ( $\text{Cd}^{2+}/\text{S}^{2-}$  ratio less than 1) are unstable compared to those with an excess of  $\text{Cd}^{2+}$  ions. Figure 4.6b shows the dependence of the PL efficiency on  $\text{Cd}^{2+}/\text{S}^{2-}$  ratios obtained by adding  $\text{Cd}^{2+}$  ions to a sample with an initial

$\text{Cd}^{2+}/\text{S}^{2-}$  ratio of 1/2. The PL efficiency increases very fast with  $\text{Cd}^{2+}/\text{S}^{2-}$  ratios from 1 to 1.5. After that it increases slowly and tends to saturation at higher  $\text{Cd}^{2+}/\text{S}^{2-}$  ratios. This trend agrees with the influence of the initial  $\text{Cd}^{2+}/\text{S}^{2-}$  ratios on the PL efficiency. Sooklal et al. found that the PL efficiency of CdS nanoparticles varied from 10 to 20 % (compared with Coumarin 4 whose PL efficiency is considered as 1) although they synthesized the nanoparticles in stoichiometric ratio. One reason might be that for 10 % PL efficiency samples the actual  $\text{Cd}^{2+}/\text{S}^{2-}$  ratio is lower than 1 while for 20 % PL efficiency samples the actual  $\text{Cd}^{2+}/\text{S}^{2-}$  ratio is higher than 1. From the viewpoint of high efficiency for the blue PL, samples with  $\text{Cd}^{2+}/\text{S}^{2-}$  ratio larger than 1.5 are preferred (Fig. 4.6b).

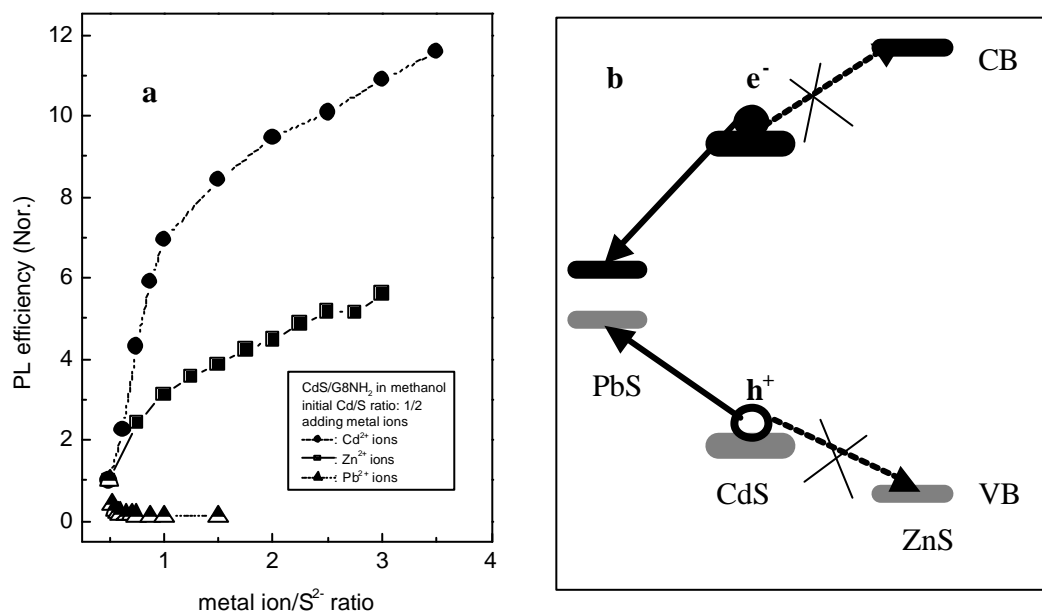


Figure 4.7a Effects of adding  $\text{Cd}^{2+}$ ,  $\text{Zn}^{2+}$  or  $\text{Pb}^{2-}$  on the PL efficiency of  $\text{CdS}/\text{G8NH}_2$  (initial  $\text{Cd}^{2+}/\text{S}^{2-}$  ratio of 1/2) in methanol. The PL efficiency is normalized with that of  $\text{Cd}^{2+}/\text{S}^{2-} = 1/2$ .

Figure 4.7b Energy levels of valence and conduction bands for PbS, CdS and ZnS.

Metal ions that can interact with CdS particles also show obvious influence on the PL. As shown in Figure 4.7, adding  $Zn^{2+}$  ions, similar to the case of adding  $Cd^{2+}$  ions, leads to an increase in the PL while adding  $Pb^{2+}$  quenches the PL. These added metal ions should be located at the surface of CdS nanoparticles; otherwise, if they were just randomly dispersed in the solution, they would not influence the nanoparticles. Hence core-shell type structures can be formed by a sequential addition of  $Zn^{2+}$  (or  $Pb^{2+}$ ) and  $S^{2-}$  ions into a CdS nanoparticle solution. In Fig. 4.7b, energy levels of valence band and conduction band in PbS, CdS and ZnS are shown schematically [Nethercot74]. Due to the band offsets in energy levels, relaxation of photoinduced electrons and holes from a CdS core to a PbS shell is energetically allowed while it is energetically prohibited from a CdS core to a ZnS shell. Since the solubility constant of PbS ( $8.0 \times 10^{-28}$ ) is smaller than that of CdS ( $8.0 \times 10^{-27}$ ), adding  $Pb^{2+}$  ions leads to replacement of  $Cd^{2+}$  ions by  $Pb^{2+}$  ions and to the formation of a lower band gap PbS. Thus photoinduced carriers are effectively trapped in PbS and combine nonradiatively. The formation of a CdS/PbS core-shell structure will lead to the quenching of the PL from the CdS part. This is verified from Fig. 4.7 for adding  $Pb^{2+}$  ions. The formation of a CdS/ZnS core-shell structure from this point of view will not influence the PL from CdS parts. However, if the ZnS shell can passivate some nonradiative defect states at the surface of CdS, the PL from the CdS will increase. This idea has been used to improve the band gap PL of II-VI semiconductor nanocrystals in wet chemical synthesis [Peng97, Hines98]. The formation of a CdS/ZnS core-shell-structure is shown in Figure 4.8. The band gaps of CdS nanoparticles redshift

by adding  $S^{2-}$  and  $Zn^{2+}$  ions, indicating the formation of the core-shell-structure [Mews96].

The molecular orbit model can explain the redshift of the band gap in a simple fashion: Due to the interaction between molecule-like orbits of CdS quantum dots and of ZnS quantum wells, the energy difference between the newly formed highest occupied molecular orbit (HOMO) and the lowest unoccupied molecular orbit (LUMO) is narrower than that of the former HOMO and LUMO (Fig. 4.8A). Apart from the formation of the core-shell structure (Fig. 4.8B(I)), isolated ZnS nanoparticles at the surface of CdS nanoparticles (Fig. 4.8B(II)) and  $Zn_xCd_{1-x}S$  ( $0 < x < 1$ ) alloys (Fig. 4.8(III)) could also form when preparing such binary compounds [Youn88, Haesselbarth93, Peng98]. Controlling experimental parameters can avoid unwanted structures. Pure ZnS nanoparticles show an exciton peak around 250 nm (Fig. 4.8C dashed dotted line). The absence of this exciton peak excludes the formation of isolated ZnS nanoparticles while the redshift of band gaps rules out the existence of  $Zn_xCd_{1-x}S$  ( $0 < x < 1$ ) alloys since the band gap blueshifts with increasing ZnS amount for such alloys. Figure 4.8D shows the effect of a ZnS shell on the PL of a CdS core. With increasing thickness of the ZnS shell, the PL from CdS decreases. The thickness of the ZnS shell can reach three layers. Upon further increasing the amount of  $Zn^{2+}$  and  $S^{2-}$  ions, the clear nanocomposite solution becomes turbid. It is found that in different samples the degree in decrease is also different, but not large compared with sulfur -containing quenchers. Note that the effect of  $Zn^{2+}$  ions on the PL (Fig. 4.7) is different from that of a ZnS shell (Fig. 4.8(D)). This will be discussed in the next part.



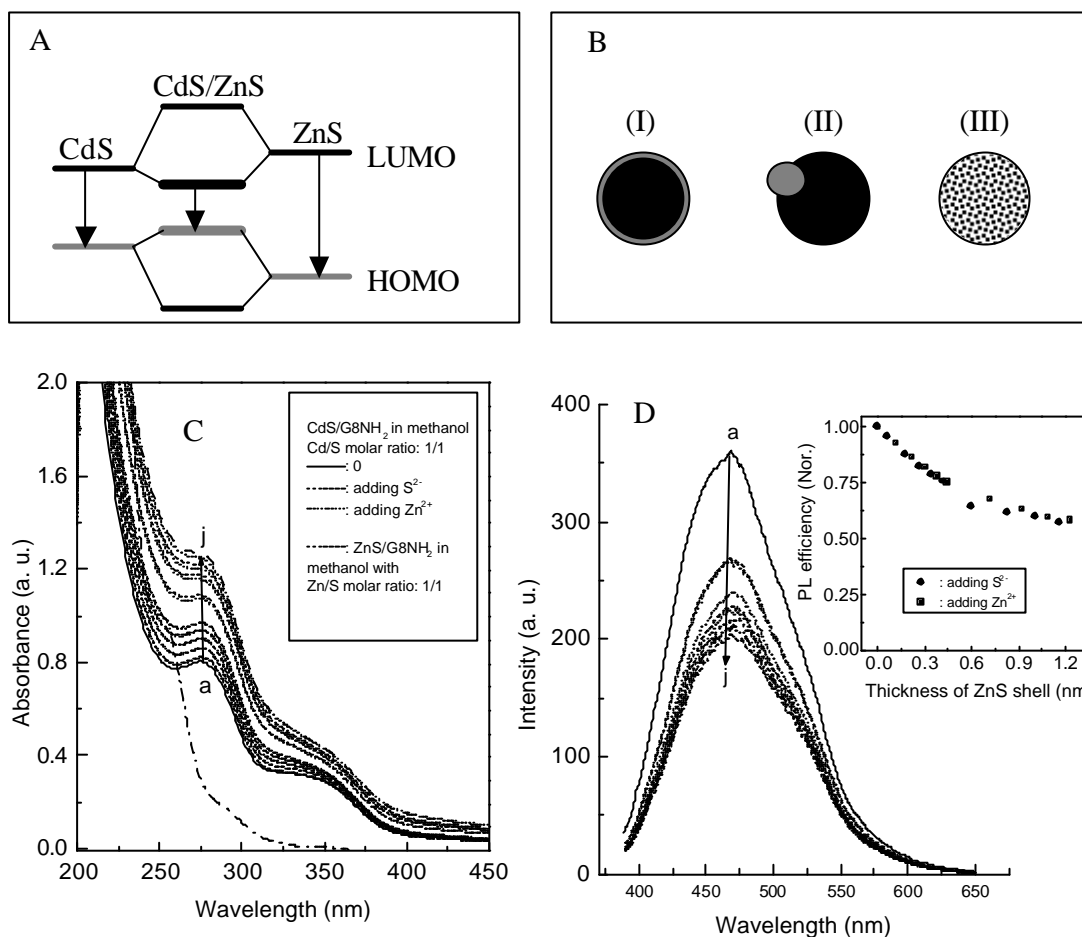


Figure 4.8A Redshift of band gap for a CdS/ZnS core-shell-structure from molecular orbit model.

Figure 4.8B Three possible structures of CdS/ZnS composites with (I) CdS Core-ZnS shell structure, (II) heterogeneous CdS and ZnS structure and (III)  $Zn_xCd_{1-x}S$  alloys.

Figure 4.8C Evolution of absorption spectra of CdS/G8NH<sub>2</sub> (initial Cd/S ratio of 1/1) nanocomposites in methanol upon sequential addition of Zn<sup>2+</sup> and S<sup>2-</sup>: calculated thickness of ZnS shell: (a) 0, (b) 0.06 nm, (c) 0.17 nm, (d) 0.26 nm, (e) 0.34 nm, (f) 0.41 nm, (g) 0.59 nm, (h) 0.82 nm, (i) 1 nm, (j) 1.2 nm.

Figure 4.8D Corresponding evolution of PL spectra. Inset: dependence of PL efficiency on ZnS shell thickness.

## 4.7 The mechanism of blue PL

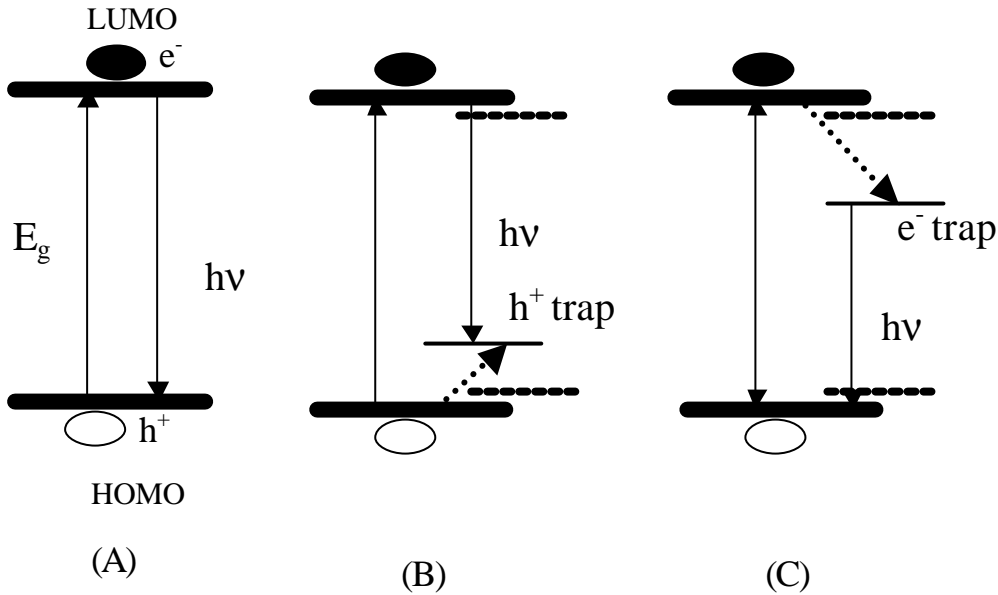


Figure 4.9 PL mechanism schemes. Dashed lines represent shallow nonradiative defect states.

Blue PL from CdS nanoparticles using other dendrimers as stabilizers was first reported by Sooklal et al. [Sooklal98]. The mechanism of this blue PL however has not been discussed. Figure 4.9 shows three possible mechanisms of the PL, i.e., recombination of free carriers (A), of trapped holes with free electrons (B), and of trapped electrons with free holes (C). If free carriers are responsible for the PL,  $h\nu$  is close to  $E_g$ . If deeply trapped holes are involved, the PL corresponds to a transition from the conduction band (LUMO) to the hole trap state (Figure 4.9(B)). If the deeply trapped carriers are electrons, the PL takes place from the trapped electron state to the valence band (HOMO, Figure 4.9 (C)). For CdS, the difference in the effective mass of electron ( $m_e = 0.22 m_0$ ,  $m_0$  is the mass of a free electron) and of hole ( $m_h = 0.7 m_0$ ) is relatively

large [Mews94]. According to formula 2.1, the fraction of extra kinetic energy due to confinement carried by electrons ( $E_e = E_t \cdot m_h / (m_h + m_e)$ ,  $E_e$ ,  $E_t$  are electron and total kinetic energy) is rather high (75%) compared to that by holes (25%). This indicates that the recombination of a free electron with a trapped hole is more sensitive to size effects than that of a trapped electron with a free hole. Therefore, we can use the sensitivity of the PL peak energy to the particle size to determine the PL mechanism.

As shown above, CdS nanoparticles with non-stoichiometric ratio show an obvious growth behavior. We can use this to study the relation between the PL and the particle size. Figure 4.10a shows absorption, (PL) excitation, and emission spectra of one day old CdS/G8NH<sub>2</sub> nanocomposites with an initial Cd/S ratio of 3/1. Figure 4.10b show the corresponding spectra after 22 days RT aging. Redshift in band gap and PL peak compared to Fig. 10a indicates an increase in particle size. As shown in Figure 4.10, the excitation band gap is narrower than the absorption band gap, indicating less effective emission from smaller particles. We use the excitation band gap as the band gap for photoluminescent particles.  $E_g - h\nu$  is 0.84 ( $\pm 0.005$ ) eV for Figure 4.10a and 0.87 eV for Figure 4.10b. Since  $E_g - h\nu$  is quite large, this excludes the mechanism shown in Fig. 4.9(A) as the PL mechanism. Therefore, the PL process should involve deeply trapped electrons or holes. For a transition arising from trapped electrons, the variation of  $h\nu$  with particle size,  $\Delta h\nu$ , would be  $0.25\Delta E_g$  ( $\Delta E_g$  is the variation of  $E_g$  with particle size). The  $\Delta h\nu$  between Figure 4.10a and Figure 4.10b (0.13 eV) is however rather close to  $0.75\Delta E_g$  (0.12 eV), indicating its high sensitivity on particle size. From this, we can exclude trapped electrons as deeply trapped carriers here. The energy level difference between the

hole trap and the valence band caused by size variation should be close to  $0.25 \Delta E_g$ . The value of 0.87 eV determined in Fig. 4.10a minus that of 0.84 eV from Fig. 4.10b is 0.03 eV. This value is in good agreement with the value of 0.04 eV obtained from  $0.25\Delta E_g$ . Therefore, the mechanism shown in Figure 4.10(B) is the most probable path for the PL process. This is consistent with observations. In bulk CdS, S sites disturbed by Cd vacancies produce deep hole trap states around 0.84 eV above the valence band [Ralph78].

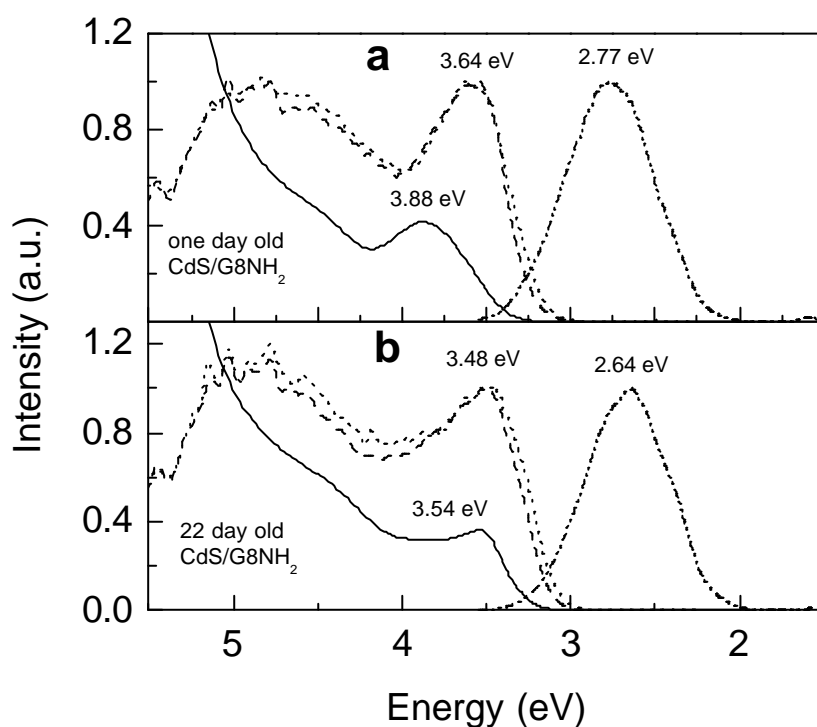


Figure 4.10 Absorption, excitation and PL spectra of CdS nanoparticles for (a) one day old and for (b) 22 day old.  $\lambda_{ex} = 320$  nm for PL spectra (dash dotted lines at right),  $\lambda_{em} = 450$  nm (dashed lines) and  $\lambda_{em} = 580$  nm (dotted lines) for excitation spectra.

We have investigated the effects of various additives on the blue PL. They can be divided into three groups: Group I increases the PL; group II decreases the PL; group III has no obvious influence on the PL.  $\text{Cd}^{2+}$  and  $\text{Zn}^{2+}$  ions belong to group I.  $\text{Pb}^{2+}$ ,  $\text{S}^{2-}$ , and  $\text{C}_{12}\text{H}_{25}\text{SH}$  belong to group II.  $\text{G4NH}_2$  and  $\text{C}_{16}\text{H}_{33}\text{NH}_2$  belong to group III. The PL efficiency is determined by both radiative processes and nonradiative processes. For nanoparticles, due to an increased surface area where various defect states dominate, nonradiative processes play an important role in the PL process.

From the viewpoint of nonradiative processes, opening of new nonradiative paths decreases the PL efficiency, while elimination of nonradiative paths increases the PL efficiency. This can be further divided into static and dynamic effects. For example, pure static quenching decreases the PL intensity with no influence to the PL decay kinetics while pure dynamic quenching decreases the PL intensity and simultaneously shortens the PL decay kinetics. For most systems both channels contribute. Time-resolved PL measurements can help us to understand the PL process better. Figure 4.11a shows the effects of adding  $\text{Pb}^{2+}$  and  $\text{Cd}^{2+}$  ions on the PL decay of nanocomposites. The inset in Figure 4.11 shows a complete decay curve. The rise time of the PL is very fast (within the time resolution of the measurement system), indicating very short trapping times for photoinduced electrons and holes. The decay process is longer than our 2 ns time window as some residual PL still exists when the next laser pulse arrives. Decay curves of PLs in a 2 ns time window can be fitted well using a biexponential function,  $I_{\text{em}} = A_1 \exp(-t/\tau_1) + A_2 \exp(-t/\tau_2)$ , with fitting parameters given in Table 4.1.

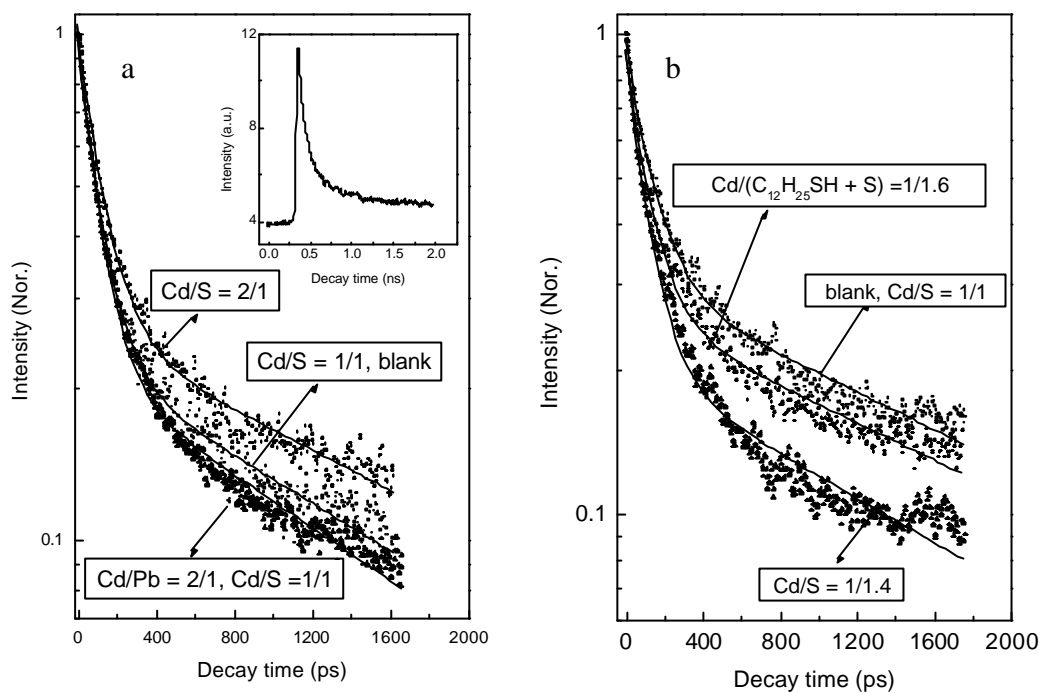


Figure 4.11 Normalized PL decay curves of the blue PL detected at the peak position (450 nm) for (a) blank sample, added  $\text{Pb}^{2+}$  ions and added  $\text{Cd}^{2+}$  ions and (b) blank sample, added  $\text{S}^{2-}$  and added  $\text{C}_{12}\text{H}_{25}\text{SH}$ . Dots are experimental points, while the solid lines show biexponential theoretical fits.

The multiexponential decay is often observed for a PL recombination in semiconductor nanoparticles [Braun01, Kumar01, Sirota01]. Various factors, such as size and morphology distribution, defect state energy distribution for both nonradiative and radiative centers, have been ascribed to contribute the multiexponential decay processes.

Table 4.1: The Fitting Parameters of the PL decay Curves.

Samples	A <sub>1</sub>	t <sub>1</sub> (ps)	A <sub>2</sub>	t <sub>2</sub> (ps)
<b>Series 1</b>				
<b>Blank (Cd/S = 1/1)</b>	0.78	102±1	0.22	1843±50
<b>Added Cd<sup>2+</sup> (Cd/S = 2/1)</b>	0.78	114±2	0.26	2179±63
<b>Added Pb<sup>2+</sup> (Pb/Cd = 0.04/1, Cd/S =1/1)</b>	0.81	96±1	0.29	1662±35
<b>Series 2</b>				
<b>Blank (Cd/S = 1/1)</b>	0.66	124±2	0.31	2229±57
<b>Added S<sup>2-</sup> (Cd/S =1/1.4)</b>	0.71	103±2	0.20	1875±63
<b>Added C<sub>12</sub>H<sub>25</sub>SH (Cd/SH =1/0.6, Cd/S+SH = 1/1.6)</b>	0.65	112±2	0.26	2256±72

Compared with the blank sample, the PL decay by adding Cd<sup>2+</sup> ions slows down a little while it accelerates slightly by adding Pb<sup>2+</sup>. This indicates that the effects of these added ions to the PL processes are partially dynamic. This can help us to analyze nonradiative processes. For the case of adding Pb<sup>2+</sup>, carriers trapped at PL centers of the CdS part are further relaxed to the PbS part due to the narrower band gap of the latter. This leads to the observed dynamic quenching. For the case of adding Cd<sup>2+</sup> ions, the slowing of the decay process indicates that some nonradiative paths may have been eliminated. Since Cd<sup>2+</sup> ions mainly bind S<sup>2-</sup> ions, this could mean that S dangling bonds

(for example), which form shallow traps above the valence band, play an important role in the nonradiative recombination. Adding  $\text{Cd}^{2+}$  ions can passivate S dangling bonds and hence increase the PL. Figure 4.16b shows the effects of adding  $\text{S}^{2-}$  ions and  $\text{C}_{12}\text{H}_{25}\text{SH}$  molecules on the PL decay process. Both shorten the decay process, probably indicating an increase in nonradiative centers. In comparison with  $\text{Cd}^{2+}$  ions,  $\text{S}^{2-}$  ions mainly interact with electron traps. If they interact for example with Cd dangling bonds (acceptor-type nonradiative centers), which form shallow traps below the conduction band, the PL should increase. But we observe the opposite phenomenon. This indicates that acceptor-type nonradiative centers might not play an important role in the nonradiative process. This is determined by the PL mechanism. Since PL centers are donor types (Cd vacancy states), they are in competition with donor-type nonradiative centers for electrons (either free or shallow-trapped). If the density of donor-type nonradiative centers is high, their recombination with electrons is preferred. The PL decreases. The status of electrons, either free or shallow-trapped, is not critical. Therefore adding  $\text{S}^{2-}$  ions should influence the surface structure and result in the formation of a surface with more nonradiative centers related to S dangling bonds. This leads to the quenching of the PL. The shortening of the PL decay times results from the further relaxation of carriers at PL centers to these nonradiative paths. The case for  $\text{C}_{12}\text{H}_{25}\text{SH}$  molecules is similar to that of  $\text{S}^{2-}$ . Since  $\text{C}_{12}\text{H}_{25}\text{SH}$  molecules cannot enter the crystal structure of CdS nanoparticles, this further verifies that the quenching process is mainly surface-related.

Since the solubility constant of ZnS ( $1.6 \times 10^{-23}$ ) is larger than that of CdS, adding only  $\text{Zn}^{2+}$  ions will not lead to the formation of a ZnS shell. However, similar to  $\text{Cd}^{2+}$  ions,  $\text{Zn}^{2+}$  ions can also decrease nonradiative centers related to S dangling bonds to a



certain degree and thus increase the PL, though in a less effective way than  $\text{Cd}^{2+}$  ions (for example, lattice mismatch). For CdS/ZnS core-shell structure, the PL decreases 30 % for 3 layers of the ZnS shell. The sources might be: formation of more interface defects due to the large mismatch of CdS and ZnS lattice constants (7 %) or elimination of some PL centers. As for  $\text{G4NH}_2$  and  $\text{C}_{16}\text{H}_{33}\text{NH}_2$ , they are electron donors and mainly influence acceptor-type nonradiative centers. Different from adding  $\text{S}^{2-}$  ions, they do not increase the density of S dangling bonds. Therefore, they show no obvious influence to the PL.

From the viewpoint of the radiative process, by increasing the density of radiative centers the PL should also increase. By adding  $\text{Cd}^{2+}$  ions, the number of S-vacancy-related radiative centers should be reduced. We should observe a decrease in the PL. By adding  $\text{S}^{2-}$ , we should observe an increase in the PL due to an increase in radiative centers. Experimental results show the opposite. Therefore, we believe that these additives mainly influence the nonradiative paths.

#### **4.8 The location of CdS nanoparticles and the morphology of CdS/ $\text{G8NH}_2$ nanocomposites**

According to the position of metal nanoparticles on dendrimers, three different types of metal-dendrimer nanocomposites have been recently defined by Balogh et al. [Balogh99]: Metal nanoparticle inside the dendrimer (internal type), outside the dendrimer (external type), or both inside and outside the dendrimer (mixed type). The realization of different types is determined by the binding mechanism of metal ions, by immobilization reactions, and by interactions in the nanocomposite. According to the

actual size of synthesized nanoparticles ( $D_N$ ), the diameter of dendrimers ( $D_D$ ), and the size of nanoparticles calculated from the number of metal ions bound to each dendrimer ( $D_C$ ), the constitution of nanocomposites can be roughly estimated: One nanoparticle/one dendrimer, several nanoparticles/one dendrimer or one nanoparticle/several dendrimers. When  $D_N$  is similar to  $D_C$ , one nanoparticle/one dendrimer is often formed. This case happens when the interactions between metal ions and internal functional groups of dendrimers are strong [Balogh98, Zhao98] or when the loading of metal ions is confined inside the dendrimers [Lemon00]. In this case, the nucleation and growth of nanoparticles is confined within a single dendrimer. The size of nanoparticles can be controlled via the loading factor of metal ions to dendrimers or via the variation of the dendrimer generation.

When  $D_N$  is much larger than  $D_C$ , one nanoparticle/several dendrimers is often formed. This happens for systems where the interactions between metal ions and internal groups of dendrimers are weak [Zheng02, Torigoe01] or where metal ions are mainly bound to the surface groups of dendrimers [Garcia99] or where the generation of the dendrimers is low [Esumi98, Torigoe01]. When  $D_N$  is smaller than both  $D_D$  and  $D_C$ , the morphology of several nanoparticles/one dendrimer is formed. This happens for systems where the generation of the dendrimers is high [Groehn00]. In the last two cases, dendrimers can be called “nanoreactors”, as nanoparticles are protected by dendrimer “ligands”. However the size of nanoparticles cannot be simply estimated from the loading factor of metal ions to the dendrimer.

As already shown in chapter 4.3, stable CdS/G8NH<sub>2</sub> colloid solutions can be obtained only at the NH<sub>2</sub>/Cd<sup>2+</sup> ratio < 2. This indicates that nucleation sites of CdS

nanoparticles are close to terminal  $\text{NH}_2$  groups. Therefore, the location of CdS nanoparticles is most probable at the surface regions of dendrimers, i.e., CdS nanoparticles are weakly bound to terminal  $\text{NH}_2$  groups. The diameter of CdS nanoparticles calculated from the absorption band gap is ca. 2 nm ( $D_N$ ) [Gaponenko98], which is smaller than 9.7 nm ( $\text{G8NH}_2$  size ( $D_D$ )) and than 3.4 nm calculated for the CdS size  $D_C$ . The obtained CdS/  $\text{G8NH}_2$  nanocomposites belong to the external type and consist of two nanoparticles/dendrimer. Figure 4.12 is a topographic IC-AFM image of CdS nanocomposites on a silicon wafer after adsorption. There are some very small dots (see white circle) whose heights correspond to a single  $\text{G8NH}_2$  on hydrophilic surfaces ( $3 \sim 4$  nm) [Hieleman98, Li00, Betley01]. They are either pure single  $\text{G8NH}_2$  or single  $\text{G8NH}_2$  with nanoparticles. Most of the dots are  $\sim 9$  nm high, indicating that they include 2 or 3  $\text{G8NH}_2$  molecules together with several small CdS nanoparticles.

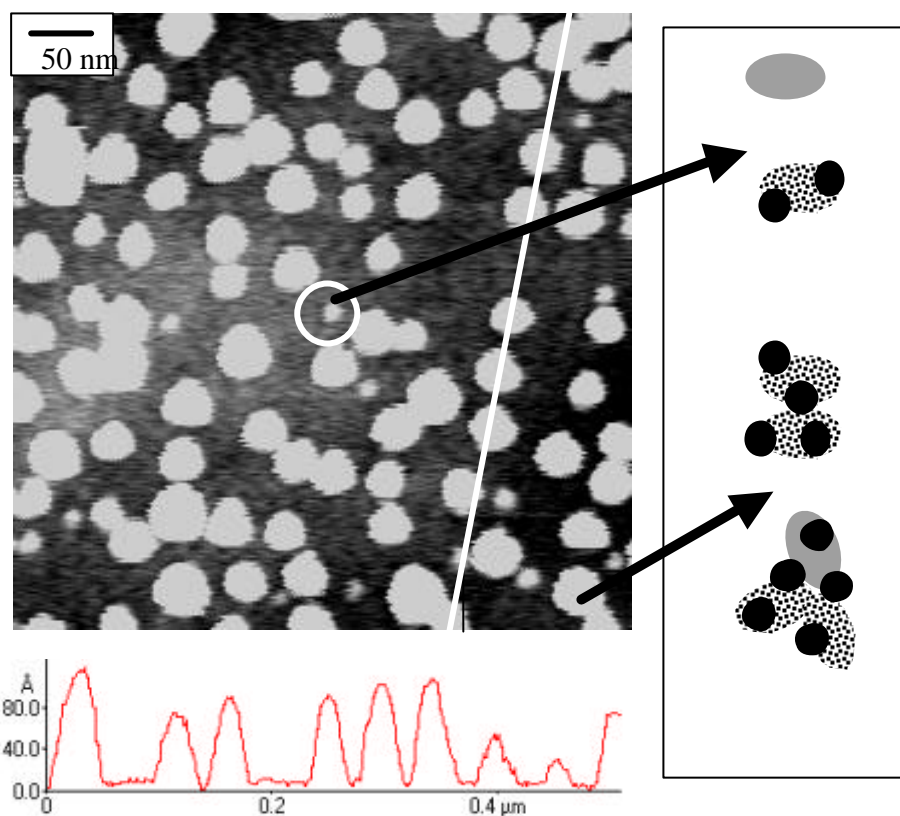


Figure 4.12 Topographic IC-AFM image of CdS/G8NH<sub>2</sub> nanocomposites (initial Cd<sup>2+</sup>/S<sup>2-</sup> ratio of 3/1) on a silicon wafer after adsorption. Possible morphologies are schematically drawn on the right.

Instead of NH<sub>2</sub>-terminated dendrimers, Lemon et al. used OH-terminated dendrimers as cages and synthesized CdS nanoparticles inside dendrimers [Lemon00]. However, compared to NH<sub>2</sub> groups, further chemical modification of OH groups, especially linking to surfaces, is more complicated. It is known that NH<sub>2</sub>-terminated dendrimers undergo protonation/deprotonation processes at different pH values [Duijvenbode98, Koper97]. Therefore, if we can control the protonation behavior of dendrimers, i.e.; we only protonate the terminal NH<sub>2</sub> groups and keep tertiary N groups deprotonated, we will have the possibility to confine CdS nanoparticles inside the dendrimers. After the synthesis of CdS nanoparticles, NH<sub>3</sub><sup>+</sup> groups can be deprotonated,

and further chemical modification can be carried out. Another advantage is that due to the repulsive interaction between protonated dendrimers, aggregation effect can be greatly reduced.

The protonation behavior of poly(propylene imine) (PPI) dendrimers has been investigated both experimentally and theoretically [Duijvenbode98]. At  $\text{pH} = 6 - 8$  (see plateau in Fig. 4.13), PPI dendrimers show the protonation behavior we want to obtain. Compared to PPI dendrimers,  $\text{NH}_2$ -terminated PAMAM dendrimers possess amide groups. Since the protonation of amide groups can be neglected at  $\text{pH}$  values discussed here, we assume that PAMAM dendrimers behave similar to PPI dendrimers.

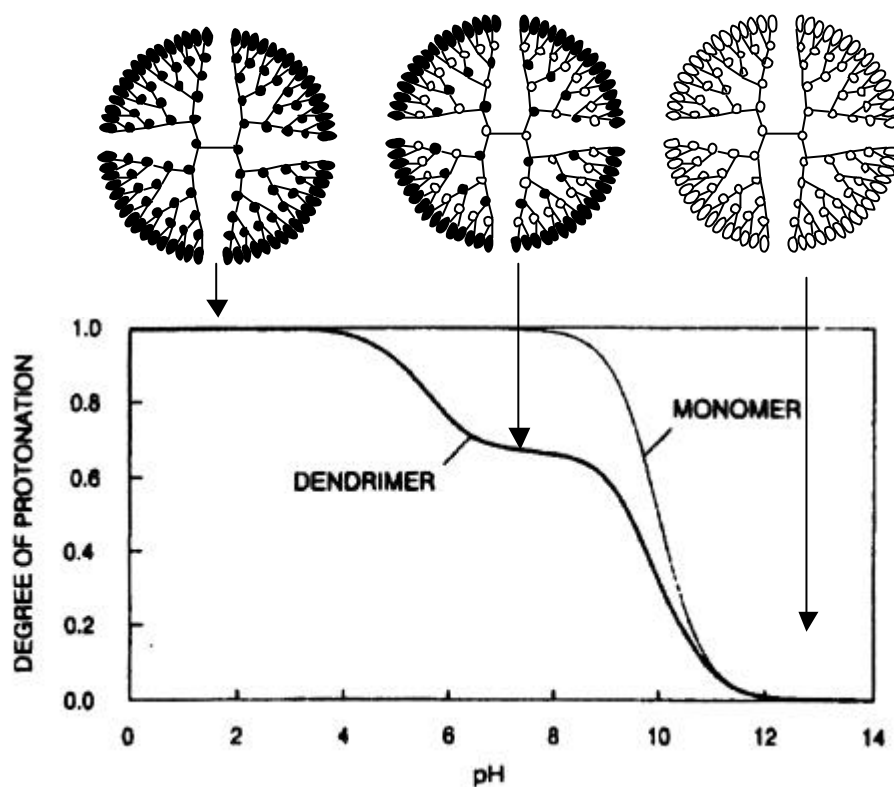


Figure 4.13 Calculated titration curve for a simplified Ising model of PPI generation 4 dendrimer. The corresponding most important protonation microstates are also shown (top). Empty circles represent deprotonated states while solid circles are for protonated states [Duijvenbode98].

Fig. 4.14a shows pH values for G8NH<sub>2</sub> and G4NH<sub>2</sub> vs. H<sup>+</sup>/(NH<sub>2</sub> + NR<sub>3</sub>). We use pH values of G4NH<sub>2</sub> in 1 M KCl aqueous solution as a reference. The pH values for G8NH<sub>2</sub> at a low electrolyte concentration with methanol as solvent are similar to those at a high electrolyte concentration with water as solvent. Above pH 5 they overlap well, indicating a similar protonation behavior. The methanolic solutions have the problems of unstable pH reading and long response time during the experiment, which is well known for non-aqueous systems with a low electrolyte concentration. Fig. 4.14b shows absorption spectra of CdS/G8NH<sub>2</sub> nanocomposites in methanol synthesized at different H<sup>+</sup>/(NH<sub>2</sub> + NR<sub>3</sub>) ratios. At pH = 6 - 7, we observe an increase in CdS particle size compared to the case at pH = 10. We obtain ca. 2 CdS nanoparticles per dendrimer at pH = 10, indicative of at least two final nucleation sites at the surface of the dendrimer. If Cd<sup>2+</sup> ions are confined inside the dendrimer, one final nucleation site is preferred. Then the size of CdS should increase. This is what we observed. Due to this, we assume that CdS is encapsulated inside the dendrimer at pH 6 ~ 8. After further decreasing the pH, precipitates form. For such cases only the absorption spectrum of the supernatant is shown.

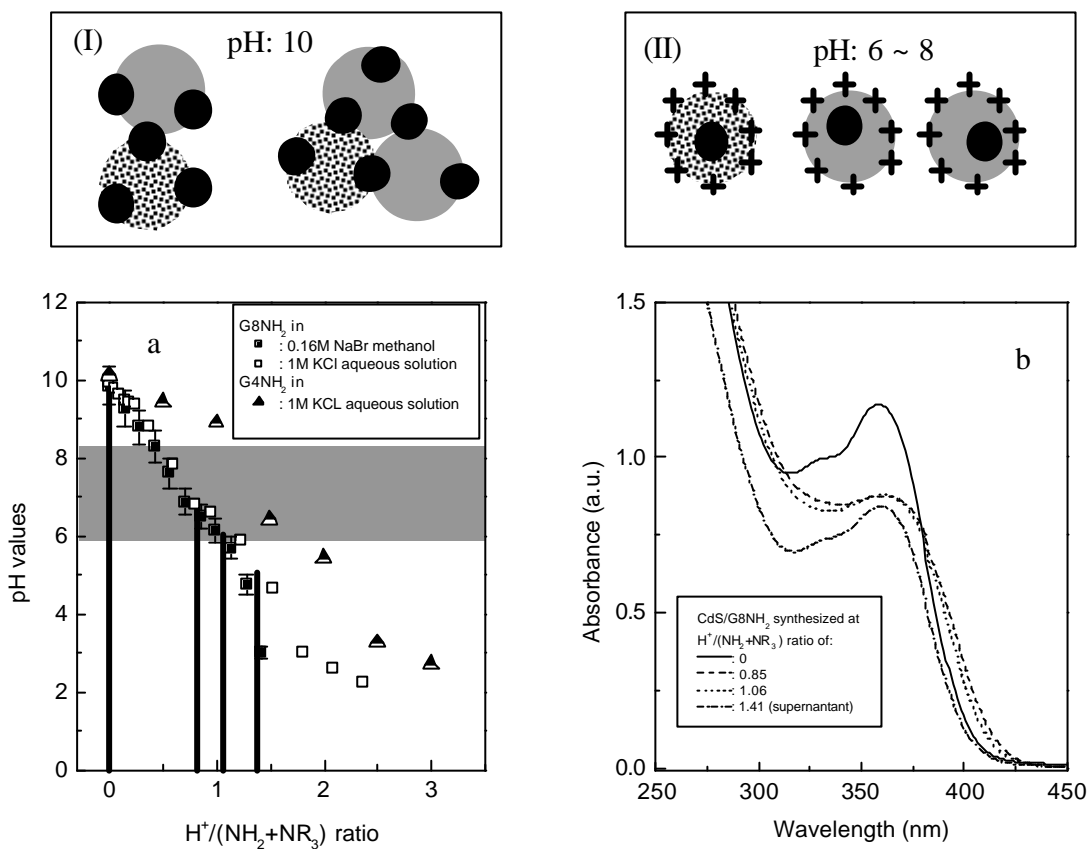


Figure 4.14a pH values for G8NH<sub>2</sub> and G4NH<sub>2</sub> at different solvent and electrolyte concentrations vs. H<sup>+</sup>/(NH<sub>2</sub> + NR<sub>3</sub>). Upper part: possible morphology of CdS/G8NH<sub>2</sub> nanocomposites synthesized at pH 10.

Figure 4.14b Absorption spectra of CdS/G8NH<sub>2</sub> nanocomposites in methanol synthesized at selected H<sup>+</sup>/(NH<sub>2</sub> + NR<sub>3</sub>) ratios. Upper part: possible morphology of CdS/G8NH<sub>2</sub> nanocomposites synthesized at pH 6 ~ 8.

Apart from using pH measurements to distinguish the protonation processes of tertiary and primary N, we find that the effects of protonation on absorption spectra are obvious and can be used qualitatively to distinguish their protonation behavior.

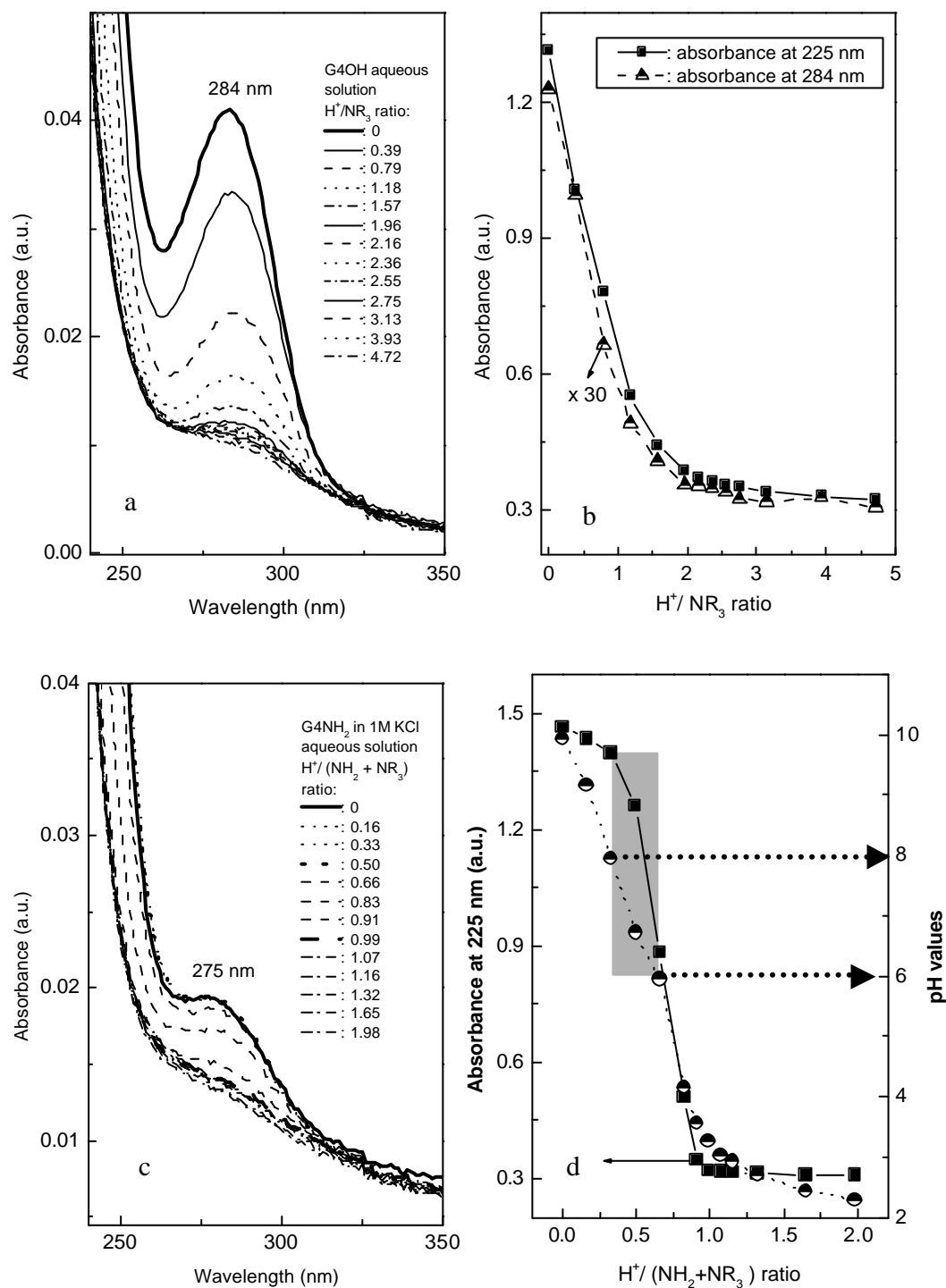


Figure 4.15 Evolution of absorption spectra of G4OH in aqueous solution (a) and the variations of absorbance at 225 and 284 nm vs.  $H^+/NR_3$  ratios (b).

Figure 4.15 Evolution of absorption spectra of G4NH<sub>2</sub> in aqueous solution (c) and the variations of absorbance at 225 nm and of pH values vs.  $H^+/(NH_2 + NR_3)$  ratios (d).



Fig. 4.15a shows the evolution of absorption spectra of G4OH in aqueous solution by adding HCl. Increasing  $H^+/NR_3$  ratio the oscillator strength of C-N bonds (both  $\delta \rightarrow \delta^*$  and  $n \rightarrow \delta^*$  bonds) obviously decreases at the beginning. This can be seen clearly from the variations of absorbance at these two bands with  $H^+/NR_3$  ratio (Fig. 4.15b). It can be divided into two stages: the rapidly decreasing stage corresponds to the protonation of tertiary N from G4OH while the flat stage indicates the completion of the protonation process. G4NH<sub>2</sub> shows a little difference to G4OH, a three-stage behavior. At the first stage, absorption spectra show a small redshift, and the variation in absorbance is small. After this stage the changes are similar to those of G4OH. Therefore, the first stage should correspond to the protonation process of primary N. The changes in spectra caused by adding HCl can be recovered by adding NaOH. This verifies that the changes are caused by reversible protonation processes.

In order to check the correlation between the variations in absorption and in protonation, we divide one sample into two parts: one part of the sample is used for pH measurement and the other part for absorption measurement. They show a good correlation as shown in Fig. 4.15d. The position at pH = 8 of the pH curve corresponds well to the turning point of absorbance at 225 nm ( $H^+/(NH_2 + NR_3)$  of 0.3), indicating the starting of the protonation of tertiary N. Therefore, the shallow area ( $H^+/(NH_2 + NR_3)$  of 0.3 to 0.6) can be used to synthesize CdS nanoparticles inside dendrimers.

An advantage of the spectroscopic method employed here is that strict measurement conditions such as high electrolyte concentration and water as solvent, which are needed for accurate pH measurements, can be avoided. A big advantage of confining nanoparticles inside NH<sub>2</sub>-terminated dendrimers is that the buildup of three-

dimensional structures can be easily realized via layer-by-layer electrostatic force assembly as schematically shown in Fig. 4.16. As shown in Chapter 2, this mechanism can be used to build three-dimensional structures of pure dendrimers. The incorporation of nanoparticles has yet not been realized. In a near future we are going to do it.

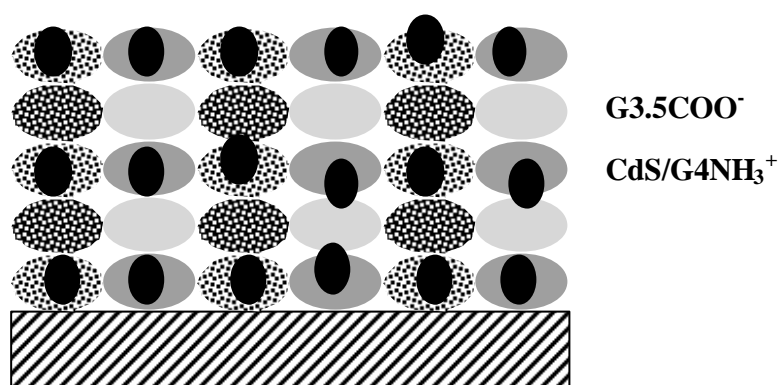


Figure 4.16 Buildup of three-dimensional CdS nanoparticles structures through electrostatic force layer-by-layer assembly.

## 4.9 Conclusions

From the above, we obtain the following conclusions:

- (a) Through the control of protonation of  $\text{NH}_2$ -terminated PAMAM dendrimers, CdS nanoparticles can be synthesized either inside dendrimers or outside dendrimers.
- (b) Blue PL is the dominant PL in this system. Energy level structure analysis and preliminary time-resolved PL decay measurements indicate that Cd vacancy-related states are the main defect states in this system. S sites disturbed by Cd vacancies are located deep within the band gap and contribute to the blue PL. S dangling bonds are

located slightly above the edge of the valence band and contribute to nonradiative processes. By controlling the nonradiative paths, the blue PL can be improved.

(c) Through the control of preparation conditions, very small CdS nanoparticles (2 nm in diameter) with a narrow size distribution can be obtained. However, the PL is dominated by a defect state emission. We have tried different additives to passivate various possible defect states at the surface of the CdS nanoparticles. Still, we have not succeeded in obtaining band edge PL. One reason might be that CdS tends to form defective particles compared with CdSe and CdTe, especially at small sizes. Only very recently CdS nanoparticles at such a small size (2 nm), obtained after a high-temperature synthesis procedure, have been reported to show the band edge PL [Peng01]. One alternative is that instead of synthesis of semiconductor nanoparticles using dendrimers as nanoreactors, we can directly use semiconductor nanoparticles that give a strong band gap PL and employ ligand exchanges to obtain dendrimer-stabilized nanoparticles. Both COOH- and NH<sub>2</sub>-terminated dendrimers are suitable ligands [Peng97, Yu02, Schmelz01]. This is one of the reasons why we synthesize “external type” CdS/dendrimer nanocomposites.



## Chapter 5

# Adsorption and Patterning of CdS/dendrimer Nanocomposites on Substrates

In chapter 4, we explored the synthesis, morphology and PL properties of CdS/G8NH<sub>2</sub> nanocomposites in solution. In this chapter, we will explore printing of “external type” CdS/G8NH<sub>2</sub> nanocomposites since printing “internal type” ones should be similar to that of pure dendrimers. First we will study their adsorption properties on different surfaces. Then we will use them as inks and print them on surfaces.

### 5.1 Introduction

The often-used mild method for positioning nanoparticles in a patterned way is via a selective adsorption on a pre-patterned surface. For example, Vossmeier et al. patterned a series of metal and semiconductor nanoparticles on a SiO<sub>2</sub>/Si surface based on the combination of lithographic patterning and solution adsorption of nanoparticles [Vossmeier98]. A combination of printing passivation SAMs and solution adsorption of nanoparticles is also a good choice if non-selective adsorption of nanoparticles on printed regions can be reduced to a low level [He00]. However, if the selective adsorption cannot be achieved easily, direct printing of nanoparticles themselves might be an alternative. In addition, compared to the  $\mu$ CP of passivation layers, the advantage of the direct printing of nanoparticles via  $\mu$ CP is the higher variability. Unprinted regions can be used for the

assembly of a second functionality. Whitesides and co-workers first reported the direct printing of Pd colloids, which in turn served as a catalyst for the electroless deposition of copper [Hidber96]. A series of surface modifications was studied before the successful printing of Pd nanoparticles could be achieved.

Here we want to explore a more general way to printing nanoparticles. A general stabilizer that can be used to synthesize or bind many different nanoparticles and can adsorb or be printed easily to the surface is desirable. So far, dendrimers have been used as nanoreactors for the synthesis of various nanoparticles, such as metals, semiconductors and magnetic oxides [Zhao98, Zhao99a, Zhao99b, Zheng02, Strable01, Sooklal98, Huang99, Tan99]. Through the control of terminal groups, dendrimers can form layers on various surfaces via electrostatic forces, hydrogen bonds, van der Waals interaction, and metal-ligand interactions [Tsukruk97, Lackowski99, Zhang02]. Therefore, dendrimers can be considered as a general stabilizer for the synthesis of nanoparticles. Recently, dendrimers themselves as ink molecules have been successfully printed on surfaces [Wu02, LiH02]. This makes direct printing of nanoparticles stabilized by dendrimers possible. Therefore, dendrimers satisfy the above requirements. In this chapter, we will explore this strategy using CdS/G8NH<sub>2</sub> nanocomposites as example.

## 5.2 Experimental

**Preparation of CdS/G8NH<sub>2</sub> nanocomposites.** Detailed preparation conditions are described in chapter 4. A representative preparation of CdS/G8NH<sub>2</sub> nanocomposites with Cd/S ratio of 3/1 is as follows: 2.5 ml of 5.5 μM G8NH<sub>2</sub> methanolic solution is mixed sequentially with 2.5 ml of 2 mM (CH<sub>3</sub>COO)<sub>2</sub>Cd and 2.5 ml of 0.7 mM Na<sub>2</sub>S (both in

methanol). The final concentration of G8NH<sub>2</sub> in the CdS/G8NH<sub>2</sub> nanocomposite solution is 1.85 μM. Here the Cd<sup>2+</sup>/S<sup>2-</sup> ratio is kept to 3/1 since it is found that at this ratio nanocomposites are successfully printed to the surface. After synthesis, the nanocomposites are stored at -35 °C to hinder further growth. The solution is dialyzed (10,000 MWCO) against methanol overnight to get rid of byproducts before adsorption and printing.

**Substrates, stamps and inks.** Si wafer: silicon wafers (orientation (100), Crystal, Berlin) are enriched with OH groups by the standard RCA procedure (see chapter 3 for details).

Au/mica and SAMs on Au/Mica: Au/mica samples are prepared by evaporation of 120-150 nm Au on 570 K preheated cleaved mica in a 10<sup>-5</sup> mbar vacuum and then annealed for several hours at 600 K (2x10<sup>-6</sup> mbar). Directly before use, the Au films are flame-annealed. For the self-assembly the samples are immersed in 1 mM COOHC<sub>15</sub>H<sub>31</sub>SH or C<sub>18</sub>H<sub>37</sub>SH ethanolic solution overnight.

Au/Cr/glass: Au substrates are first cleaned with detergents and stored under Nochromix overnight. After that the Au substrates are cleaned with 18.2 MΩ water and kept under water before evaporation (it was found that this cleaning procedure provides Au films with high quality). Normally 2-5 nm of chromium (0.08 nm s<sup>-1</sup> of deposition rate) and 150-200 nm of Au (0.23 nm s<sup>-1</sup> of deposition rate) are sequentially evaporated on a glass substrate at 650K and a base pressure of 10<sup>-5</sup> mbar. Directly before use, all Au films are flame-annealed. CN<sup>-</sup>/O<sub>2</sub> etching solution for gold: 3.725 g KCl and 0.48 g NaOH are dissolved in 1 liter of water. After checking the pH (it should be 12), 6.5 g of KCN are added.

G8NH<sub>2</sub> ink: G8NH<sub>2</sub> molecules are dissolved in 99.8% ethanol (Roth) with concentrations from 0.5 μM to 50 μM.

**Printing procedures:** see chapter 3 experimental part. For printing G8NH<sub>2</sub> and CdS/G8NH<sub>2</sub> nanocomposites, stamps are freshly activated with O<sub>2</sub> plasma. For printing alkanethiols, stamps are untreated and thus hydrophobic (~100° water contact angle). All other instruments are described in chapter 3 and 4. Fluorescence microscopy images are obtained using a Zeiss Axioskop.

### **5.3 Effects of substrates on the morphology of CdS/G8NH<sub>2</sub> nanocomposites**

The interaction between ink and substrate plays a crucial role for successful printing. Therefore, we first study the adsorption features of nanocomposites on various surfaces. The adsorption of pure dendrimers on surfaces can be classified into two types. On hydrophilic surfaces, single dendrimers dominate and the height of single dendrimers is smaller than its diameter in solution, indicating the deformation of the dendrimer due to strong interaction between dendrimer and surface [Hierleman98, Li00, Betley01]. On hydrophobic surfaces, aggregates of several or several tens of dendrimers dominate, but the height of a single dendrimer is similar to its diameter in solution, indicating weak interaction between dendrimer and surface [Li00, Sheiko96].

Fig.5.1 (upper parts) presents topographic IC-AFM images of fresh CdS/G8NH<sub>2</sub> nanocomposites on a Si wafer. The images show a high coverage of these



nanocomposites on the surface. We assume that similar to pure dendrimers the interaction between nanocomposites and the Si surface is based on hydrogen bonds.

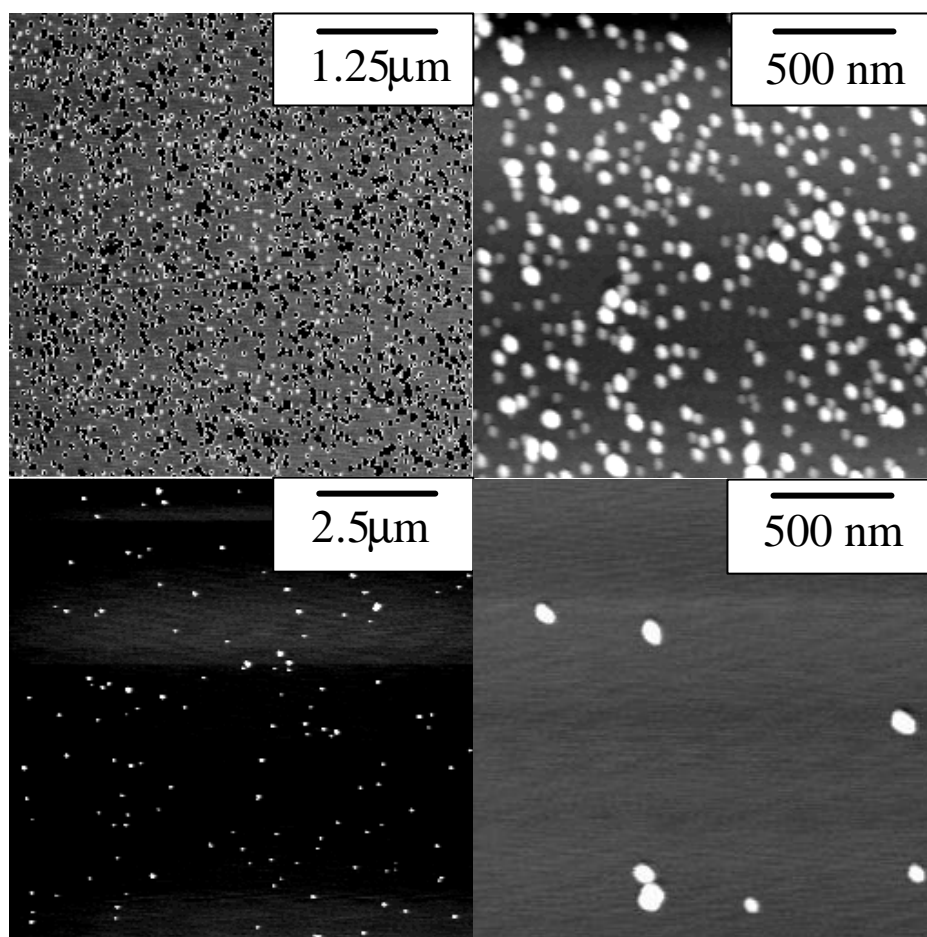


Figure 5.1 Topographic IC-AFM images of fresh CdS/G8NH<sub>2</sub> nanocomposites on Si wafer (upper parts) and on mica (lower part).

Fig.5.1 (lower parts) shows topographic IC-AFM images of CdS/G8NH<sub>2</sub> nanocomposites on freshly peeled mica. Compared to the Si wafer, the coverage of CdS/G8NH<sub>2</sub> on mica is much lower, despite of the high hydrophilicity of the mica surface. The particle size on mica is also larger than that on Si, indicating the formation of

aggregates. This shows some difference from the adsorption of pure  $\text{NH}_2$  (or  $\text{NH}_3^+$ )-terminated dendrimers on mica, where single dendrimers dominate [Li00]. The difference in adsorption of nanoparticles on Si wafers and on mica is unclear at present.

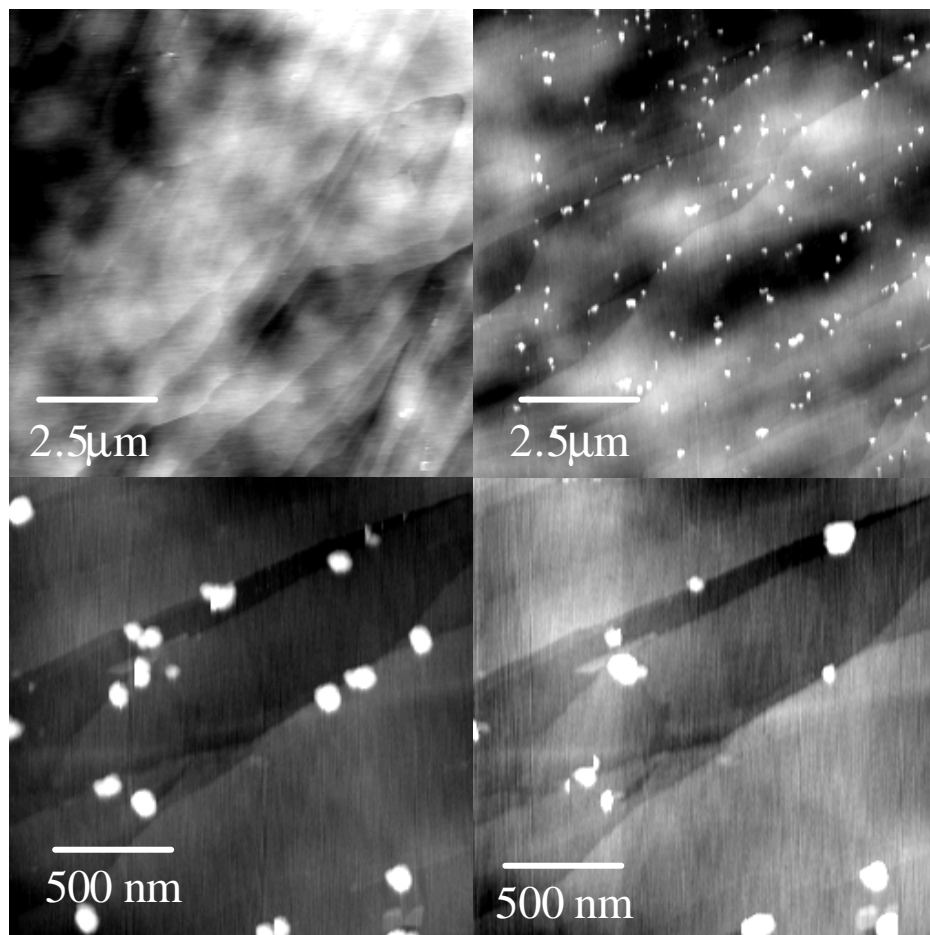


Figure 5.2 Topographic IC-AFM images of pure HOPG (upper left part) and of fresh CdS/G8NH<sub>2</sub> nanocomposites on HOPG (upper right part); effects of measurement conditions on the morphology of CdS/G8NH<sub>2</sub> nanocomposites on HOPG (lower part); for discussion see text.

Fig. 5.2 (upper left) shows a topographic image of a freshly peeled HOPG surface, revealing a clean surface with steps. After adsorption of CdS/G8NH<sub>2</sub>

nanocomposites the surface is now covered with white spots (upper right). Compared with CdS/G8NH<sub>2</sub> on a Si wafer, the spots are larger in size and more irregular in shape, indicating the further agglomeration of nanocomposites upon adsorption. At present, we are not sure whether CdS nanoparticles play a role in this agglomeration since dendrimers themselves also exist mainly in the form of aggregates on a hydrophobic surface. The interaction of the nanocomposites with the HOPG surface is weak: Either imaging amplitude or drive amplitude must be decreased in order to better image the particles. One example is shown in the two images on the lower part of Fig. 5.3. Lower left one is imaged with half drive amplitude compared to the lower right one. Due to the increase in the drive amplitude, some particles merge together; some move out of the scanned area; and some become smaller because some parts of original particles are dragged off by the tip. Another phenomenon is that these aggregates are preferentially located at step edges and defect sites of the surface. These positions have higher surface energies than flat terraces. Therefore, nanocomposites tend to adsorb at these sites.

Fig. 5.3 (upper parts) shows the adsorption of CdS/G8NH<sub>2</sub> nanocomposites on pure Au/mica and HOOC(CH<sub>2</sub>)<sub>15</sub>S /Au / mica. Since pure G8NH<sub>2</sub> can chemisorb on Au via multidentate Au-NH<sub>2</sub> ligand interactions, we assume a similar mechanism for the adsorption of CdS/G8NH<sub>2</sub> nanocomposites on Au. As for COOH-terminated SAMs, apart from hydrogen bonds, electrostatic forces also exist. Partial deprotonation of COOH groups produces a negatively charged surface. Partial protonation of NH<sub>2</sub> groups gives a positively charged nanocomposites. Electrostatic forces between them may dominate over hydrogen bonds and become the main force for the adsorption process of nanocomposites. Fig. 5.3 (lower left part) shows an IC-AFM image of CH<sub>3</sub>(CH<sub>2</sub>)<sub>17</sub>S /Au /

mica, and the right part is scanned after 10 min adsorption of CdS/G8NH<sub>2</sub>. Similar to the case of HOPG, there exist weakly interacting aggregates on the CH<sub>3</sub>-terminated hydrophobic surface. In addition, horizontal stripes on the image suggest that the tip drags (picking up and dropping down) material over the surface (fast scan direction is horizontal).

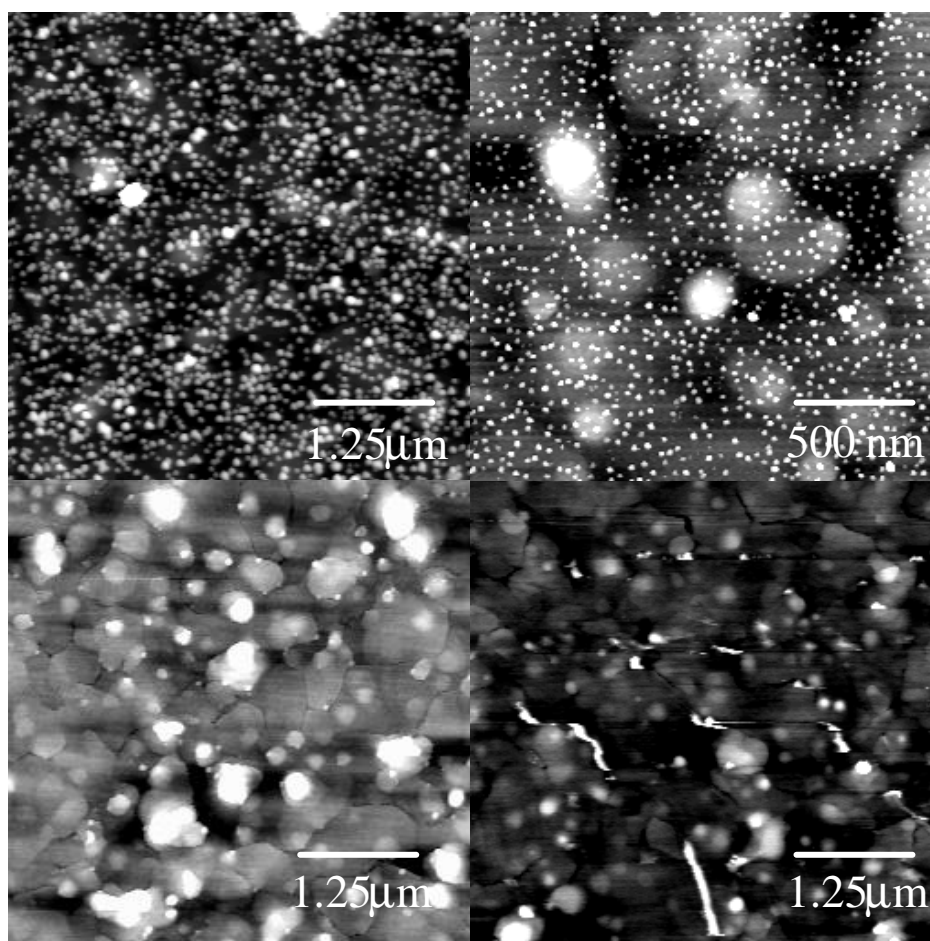


Figure 5.3 Topographic IC-AFM images of fresh CdS/G8NH<sub>2</sub> nanocomposites on Au/mica (upper left part), on HOOC(CH<sub>2</sub>)<sub>15</sub>S /Au / mica (upper right part), and on CH<sub>3</sub>(CH<sub>2</sub>)<sub>17</sub>S /Au / mica blank (lower right part). An image of pure CH<sub>3</sub>(CH<sub>2</sub>)<sub>17</sub>S /Au / mica before adsorption is shown for comparison (lower left part).

From these observations, we can roughly classify the adsorption of fresh CdS/G8NH<sub>2</sub> nanocomposites into two types according to their interactions with the surface. When nanocomposites have strong interactions (hydrogen bonds, multidentate metal-ligand interactions and electrostatic forces etc.) with the surface, they will adsorb strongly and will not form large aggregates. The surfaces that belong to this type are Si, Au and COOH-terminated surfaces. When nanocomposites have weak interactions (van der Waals forces) with the surface, they will adsorb weakly and form larger aggregates. The surfaces that belong to this type are HOPG and CH<sub>3</sub>-terminated surfaces. Two mechanisms may be responsible for the formation of larger aggregates. One is further adsorption of nanocomposites from solution to the sites already occupied by nanocomposites since interactions among themselves are stronger. Another one may be due to surface diffusion of nanocomposites. Weakly adsorbed nanocomposites, for example at terrace of HOPG, may move to more strongly adsorbed nanocomposites, for example at step edges of HOPG. This can also lead to the formation of larger aggregates. For the behavior of the pristine mica surface, we have no good explanation at present.

#### **5.4 Effects of aging on the morphology of CdS/G8NH<sub>2</sub> nanocomposites**

As already shown in chapter 4, CdS/G8NH<sub>2</sub> nanocomposites in solution upon RT aging exhibit Ostwald ripening. This growth process may not just influence CdS nanoparticles, it may also change the morphology of the whole nanocomposites and further influence their capability as inks. This is monitored by AFM measurements as

demonstrated in Fig. 5.4. The adsorption of nanocomposites on Si wafer does not cause aggregation among themselves, as shown in Fig. 5.1. Therefore, adsorption on a Si wafer can be used to study the aging behavior of nanocomposites.

Fig. 5.4 shows topographic IC-AFM images of CdS/G8NH<sub>2</sub> nanocomposites on Si wafers upon different RT aging times. From Fig. 5.4a-e, it can be seen that the nanocomposites gradually become larger upon RT aging and that the surface coverage decreases at the same time. The origin of the decrease in surface coverage is not clear. One reason is that, due to the merging of nanocomposites, the total particle number decreases. Another reason is that, due to the growth of nanocomposites, dispersion-van der Waals forces increase. The sticking coefficient to hydrophilic surfaces therefore decreases. The enhancement of van der Waals forces can be estimated from the sticking ability of nanocomposites to the surface. Fig 5.4f is a topographic IC-AFM image of aged nanocomposites on HOPG. Compared with fresh nanocomposites on HOPG (Fig. 5.2), these aged ones can be easily imaged under normal AFM measurement conditions. This indicates an increased sticking coefficient of aged nanocomposites for hydrophobic surfaces although they still prefer to adsorb at step edges rather than at terraces.

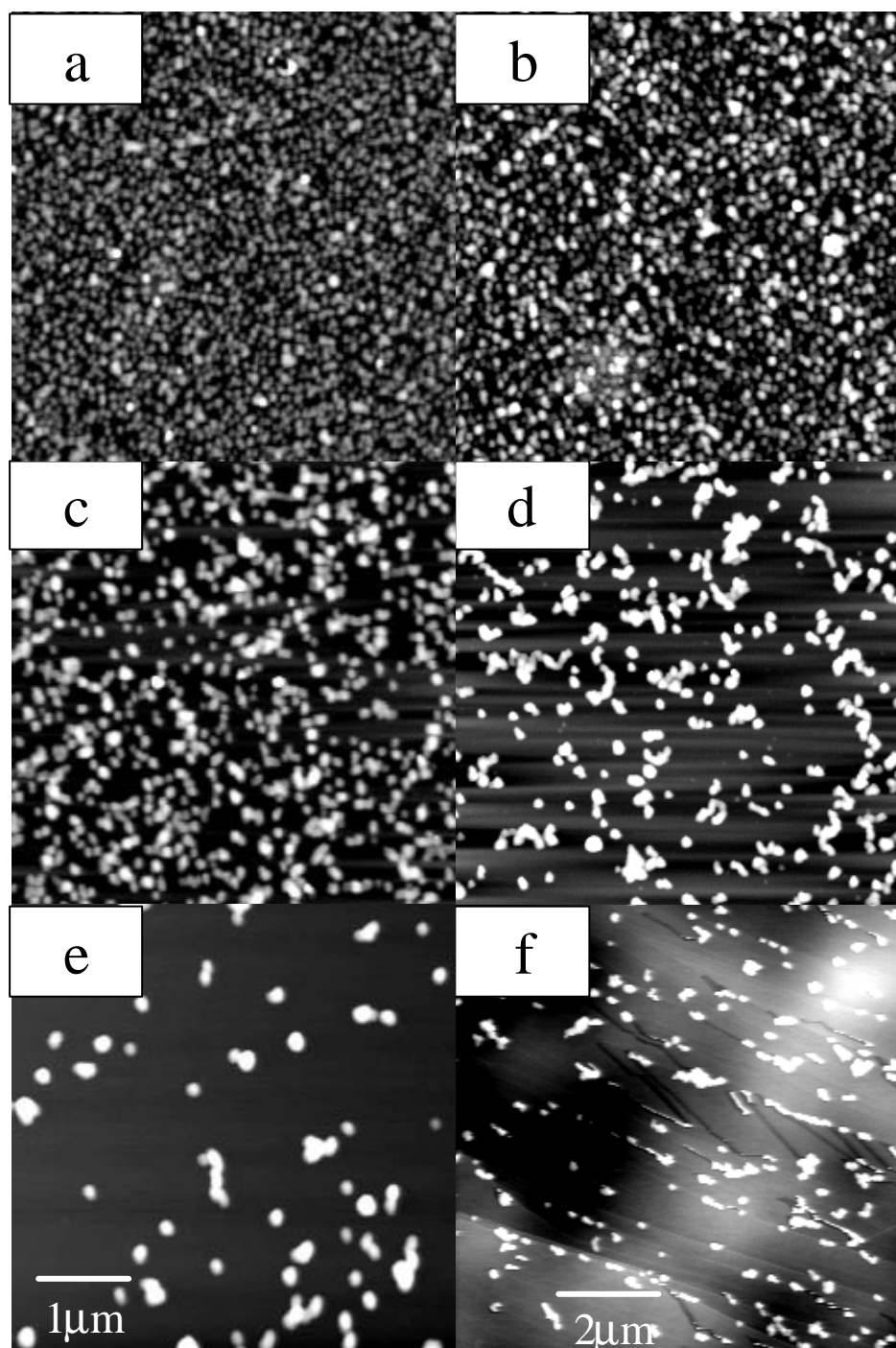


Figure 5.4 Topographic IC-AFM images of aged CdS/G8NH<sub>2</sub> nanocomposites on Si wafers with RT aging times of 2-day (a), 3-day (b), 8-day (c), 18-day (d), 29-day (e), and (f) 18-day aged nanocomposites on HOPG.

The AFM results we present here agree with the results from other methods, such as TEM [Sooklal98, Huang99] and dynamic light scattering for CdS/G4 dendrimers [Strable01, Sooklal98], and small angle X-ray and neutron scattering for CuS/G4 dendrimers [Tan99]. Since pure G8NH<sub>2</sub> molecules in methanol do not show this aggregation behavior, we believe that Ostwald ripening of CdS nanoparticles causes on one hand the growth of CdS nanoparticles themselves; on the other hand, it also causes the agglomeration of the whole nanocomposites. This leads to the formation of supramolecular aggregates. This RT aging will therefore decrease the capability of selective adsorption of nanocomposites on surfaces.

## **5.5 mCP of pure G8NH<sub>2</sub> host molecules**

As shown in chapter 3, we successfully printed G4OH dendrimers on Si wafers [Wu02]. Based on the same mechanism, NH<sub>2</sub>-terminated dendrimers should also be printable. Fig.5.5 shows an SEM image of printed G8NH<sub>2</sub> on a large area. The grey parts are printed G8NH<sub>2</sub> layers. It can be seen that G8NH<sub>2</sub> molecules are successfully transferred to the substrate, exactly in the designed pattern.



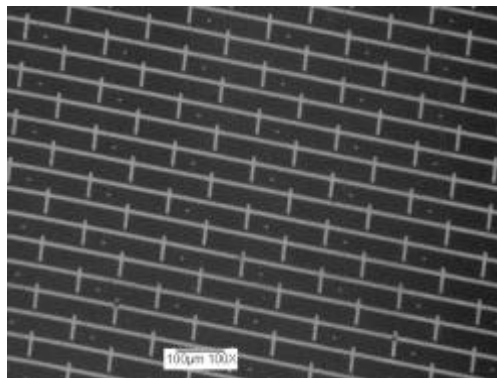


Figure 5.5 SEM image of printed G8NH<sub>2</sub> patterns on a silicon wafer. Ink concentration: 2.5 μM G8NH<sub>2</sub> in ethanol.

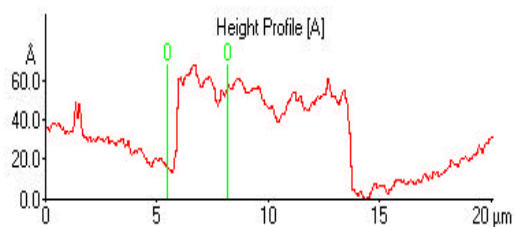
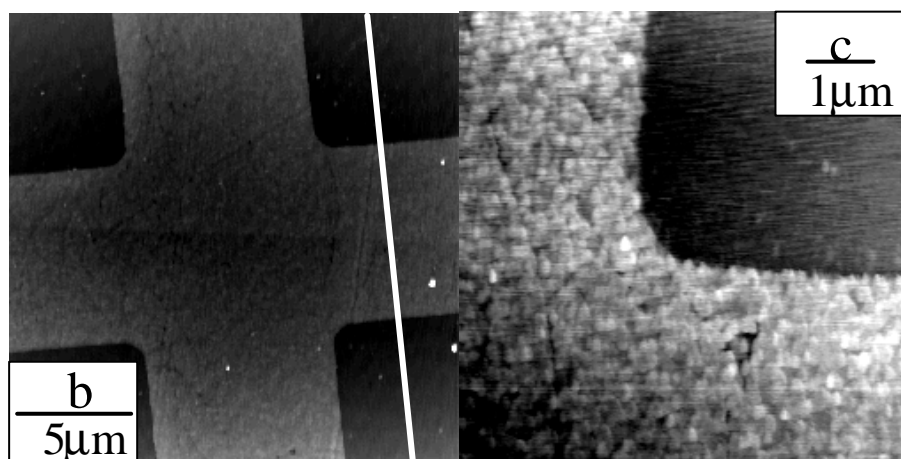


Figure 5.6 Topographic IC-AFM images (a) and (b) of printed G8NH<sub>2</sub> patterns on a silicon wafer. Ink concentration: 2.5 μM G8NH<sub>2</sub> in ethanol. Line height profile plot (lower right part)

Finer details can be revealed by zooming-in using AFM. Figs.5.6a and b are topographic IC-AFM images of a part of the pattern. From Fig. 5.6a, we can see that G8NH<sub>2</sub> molecules form a dense layer with dendrimers homogeneously distributed in the printed region. The height of the layer is between 3 and 4 nm from height profile plot, similar to the thickness of a G8NH<sub>2</sub> monolayer on hydrophilic surfaces [Zhao98]. The average roughness (the mean deviation of the data from the average of the height) of the printed layer is ca. 0.5 nm for a 5 μm size. The printed layer is therefore a smooth layer. The ink concentrations are varied from 0.5 μM to 50 μM as shown in Fig. 5.7. It is found that a good pattern quality can be achieved from 1 μM to 5 μM. Below 1 μM of G8NH<sub>2</sub>, an incomplete coverage of dendrimers on surfaces is observed. Some lines in the printed region are due to the structures from the flat stamp (which actually are surface structures of plastic dishes and are transferred to the flat stamp during molding). Above 5 μM, inhomogeneous multilayers with aggregates of dendrimers (white dots) are obtained.

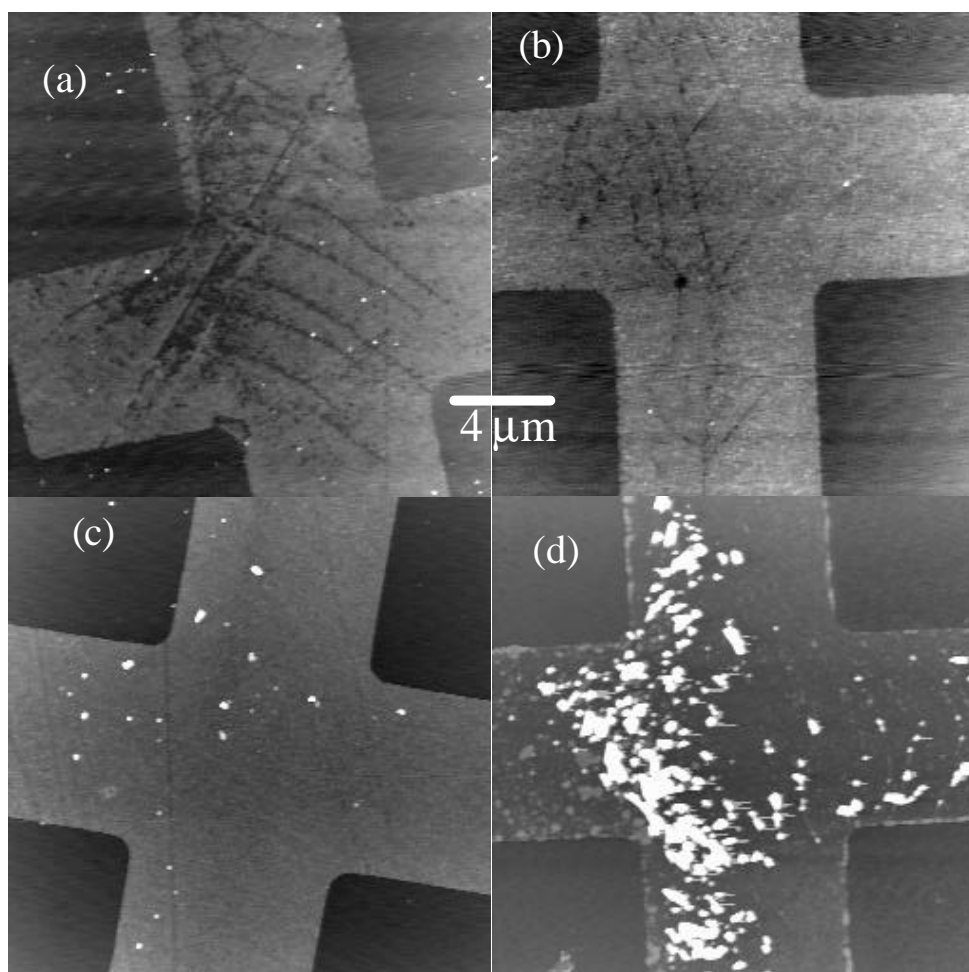


Figure 5.7 Topographic IC-AFM images of printed G8NH<sub>2</sub> patterns on silicon wafers with ink concentrations of 0.5 μM (a), 1 μM (b), 5 μM (c), and 50 μM (d) of G8NH<sub>2</sub> in ethanol.

## 5.6 Effects of morphology variation of CdS/G8NH<sub>2</sub> nanocomposites on printed patterns

Based on the same principle, nanocomposites can also be printed successfully as shown in Fig. 5.9.

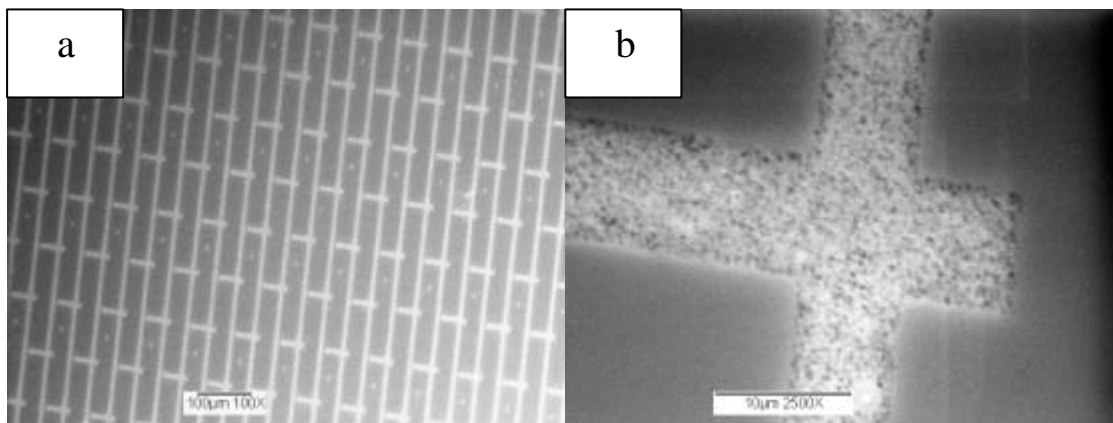


Figure 5.9 SEM images of printed aged CdS/G8NH<sub>2</sub> nanocomposites on Si wafer.

We have shown above that Ostwald ripening growth does not only increase the size of CdS nanoparticles, it also changes the morphology of the whole nanocomposites. Such changes can influence the printed patterns. Fig. 5.10 shows topographic IC-AFM images of nanocomposites after 2-day RT aging and after 22-day RT aging. For 2-day RT aging, the average height of nanocomposites is around 9 nm, and they have a relatively narrow size distribution and regular shape. They show a high affinity to the Si surface, as can be seen from the high density of nanocomposites. We term this stage “fresh nanocomposites”. After 22-day RT aging, the heights of the particles vary from 10 nm to 60 nm, and the distributions both in shape and in size also increase, suggesting the formation of supramolecular aggregates. They also show less affinity to the Si surface. We term this stage “aged aggregates”. As we discussed in chapter 4, for fresh nanocomposites, the main morphology is 2 or 3 G8NH<sub>2</sub> molecules together with several small CdS nanoparticles among them. For aged aggregates, the morphology becomes more complicated. Despite this aggregation, CdS nanoparticles do not coalesce due to the

protection by dendrimers around them: they remain distinct entities (from UV/visible absorption spectra).

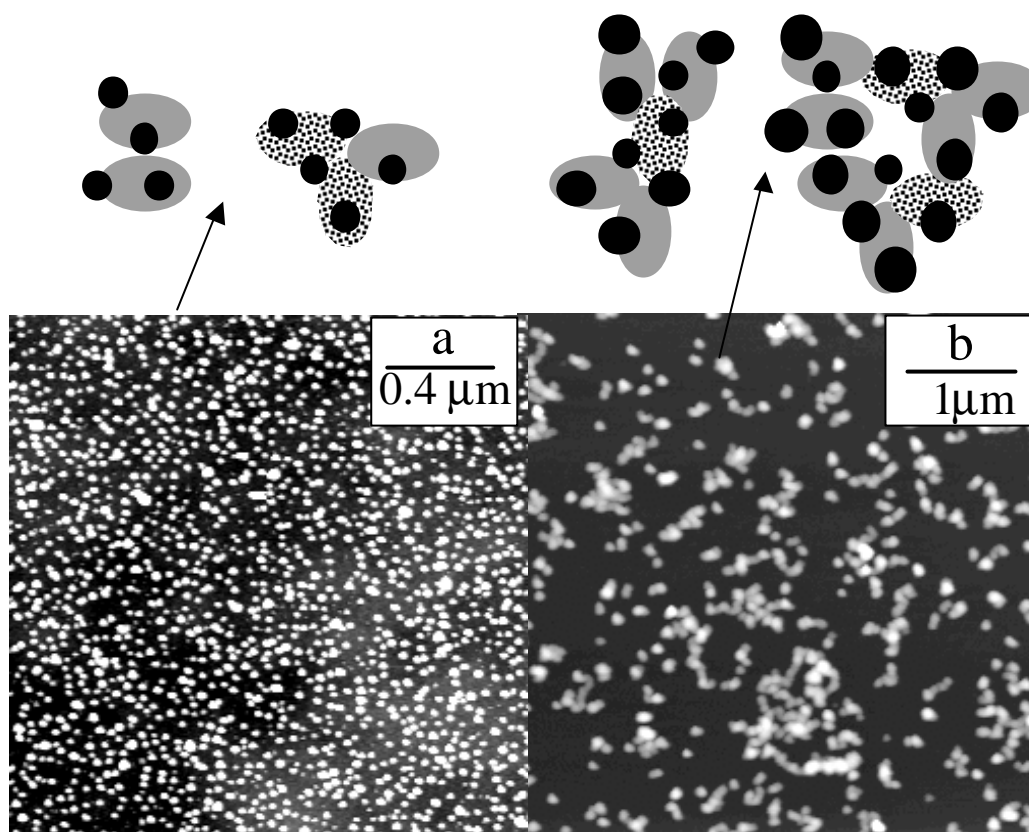


Figure 5.10 Topographic IC-AFM images of adsorbed CdS/G8NH<sub>2</sub> nanocomposites on Si wafers after 2-day RT aging (a) and after 22-day RT aging (b). Upper parts: possible morphology for these two cases.

The difference in morphology due to RT aging is reflected in printed patterns. For 2-day aged nanocomposites, the printed regions show stripe structures (Fig. 5.11a and b). For 22-day aged nanocomposites, printed regions show a homogeneous distribution of aggregates. Preliminary experimental results indicate that these stripes are formed during the conformal contact between the inked flat stamp and the structured stamp (first

printing). They are then transferred to the substrate during the second printing step. The relation between ink and stripe structure needs to be further studied before we can give an explanation of this striking phenomenon.

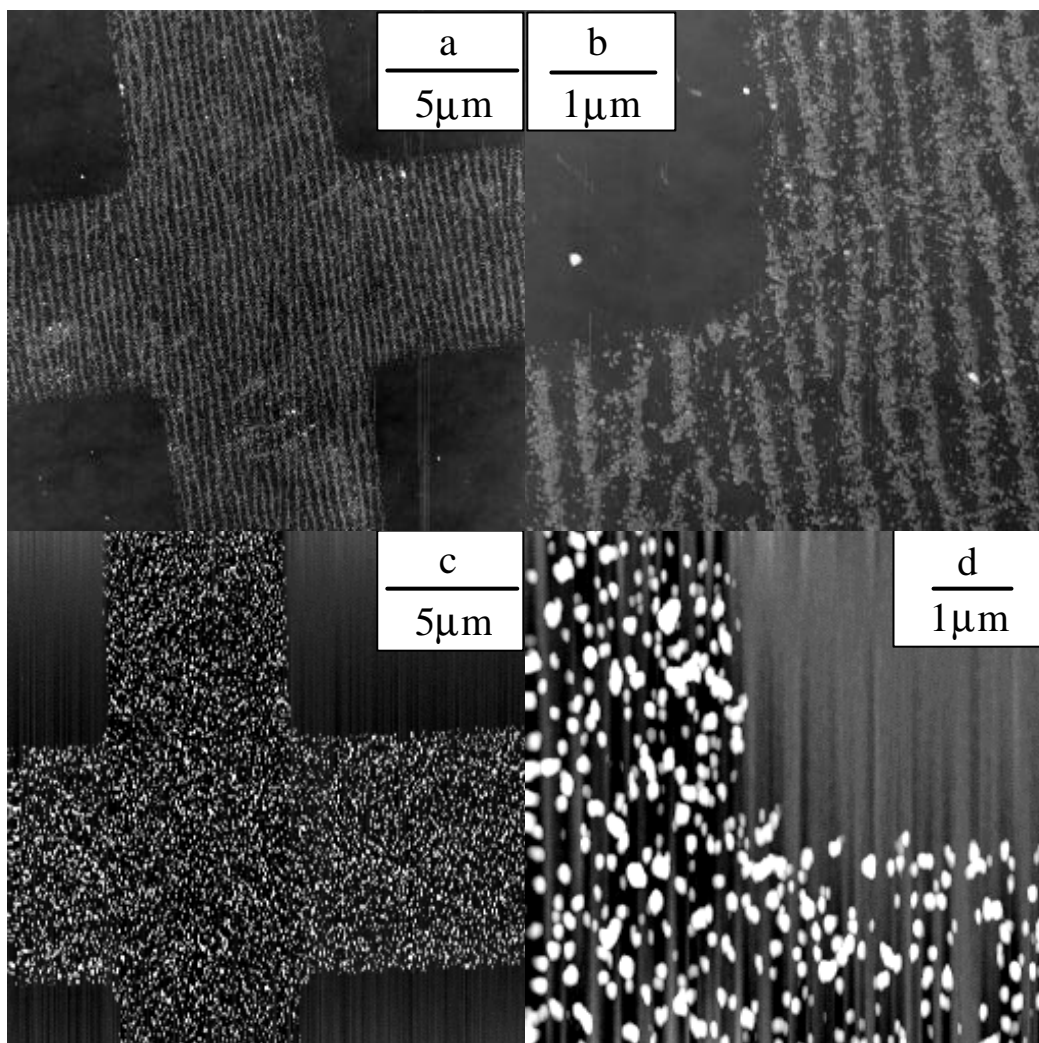


Figure 5.11 Topographic IC-AFM images of printed CdS/G8NH<sub>2</sub> patterns on silicon wafers: after 2-day RT aging (a and b) and after 22-day aging (c and d).

The successful printing of CdS/G8NH<sub>2</sub> nanocomposites on a Si wafer is based on interactions between the NH<sub>2</sub> groups of dendrimers and OH groups on the wafer. Due to

multidentate  $\text{Au}-(\text{NH}_2)_n$  ( $n$  represents possible interacting  $\text{NH}_2$  groups from dendrimers) interactions, dendrimers form a monolayer on Au via solution adsorption [Hierlemann98, Check99]. Fresh nanocomposites show a high coverage on Au by solution adsorption [Fig. 5.3]. They should also be printable on Au. This is indeed possible, as demonstrated in Fig. 5.12 for fresh nanocomposites and in Fig. 5.13 for aged aggregates.

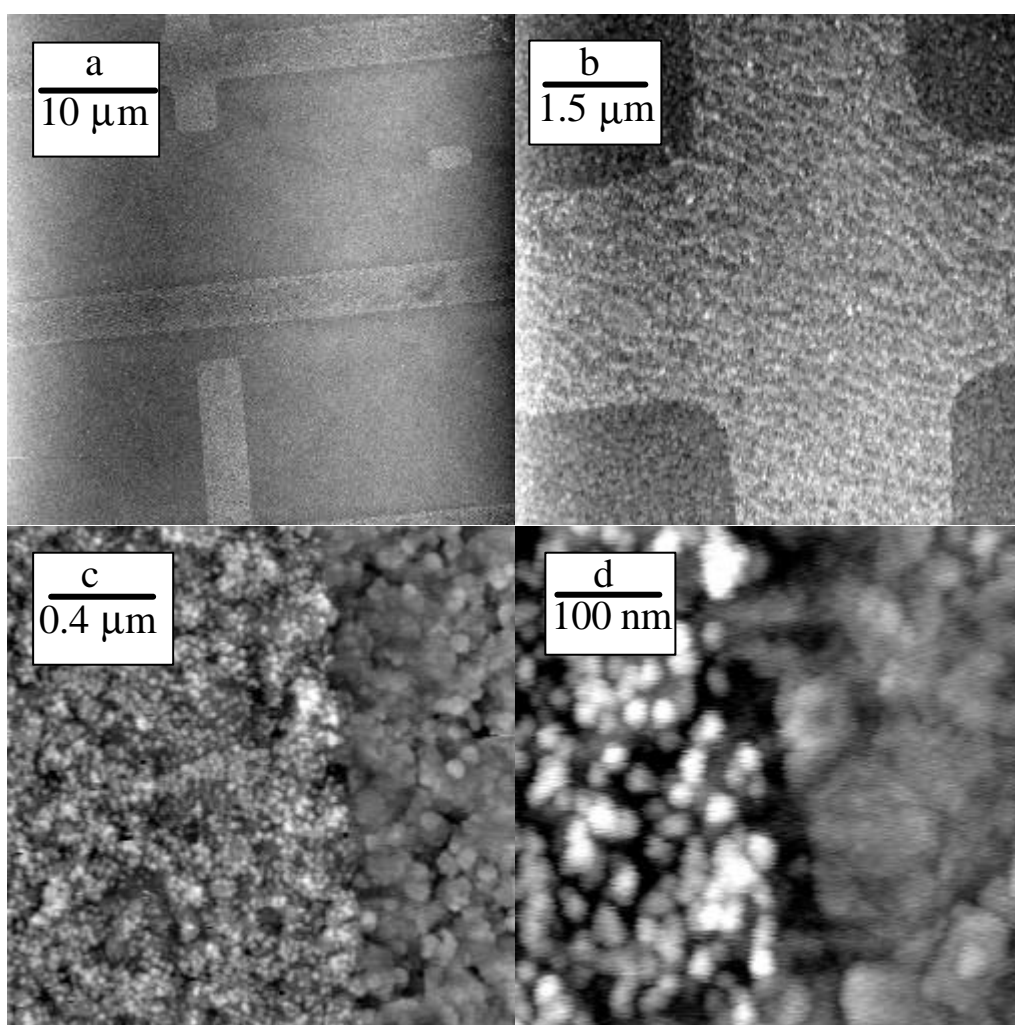


Figure 5.12 Topographic IC-AFM images of fresh  $\text{CdS/G8NH}_2$  nanocomposites printed on Au/Cr/Glass substrate. 3  $\mu\text{m}$  pattern size.

The large area AFM image in Fig. 5.12a indicates a successful transfer of nanocomposites to the Au surface. The zoom-in for a single pattern shows weak stripe features, similar to the case on Si wafer. Further zoom-in (Fig. 12c and d) suggests a high coverage of nanocomposites on Au and a sharp edge between the printed region and the unprinted region. For aged aggregates, successful transfer is also achieved as shown in Fig. 5.13.

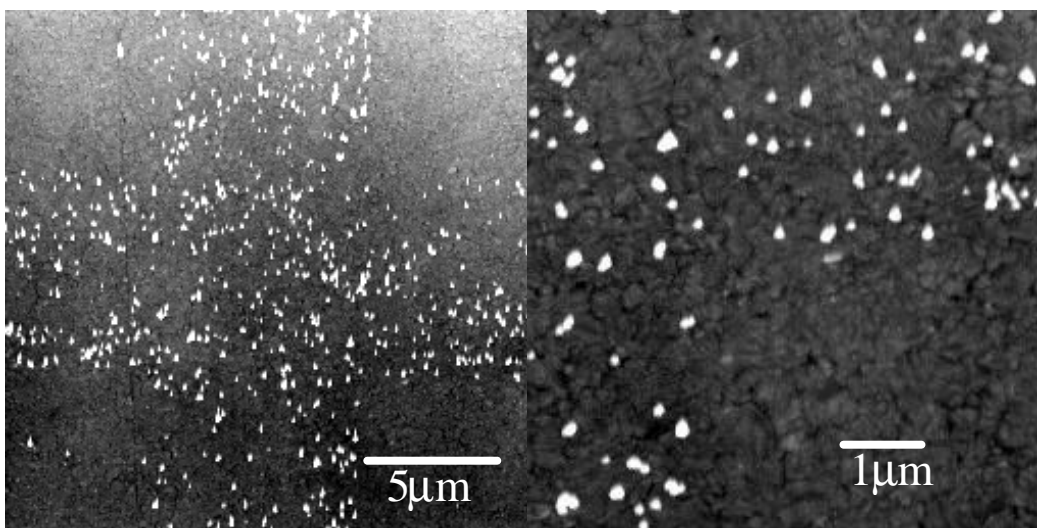


Figure 5.13 Topographic IC-AFM images of 20-day aged CdS/G8NH<sub>2</sub> nanocomposites printed on Au/Cr/Glass substrate. 8 μm pattern size.

## 5.7 Photoluminescent patterns of CdS/G8NH<sub>2</sub> nanocomposites

As shown in chapter 4, RT aging of nanocomposites can lead to ca. 10-fold increase in PL efficiency. We try to observe PL patterns of printed aged nanocomposites under a luminescence microscope. Fig. 5.14a is a PL image of printed patterns using aged CdS/G8NH<sub>2</sub> nanocomposites as inks. Control patterns formed from pure G8NH<sub>2</sub> show no



fluorescence images as expected. The PL of the nanocomposites samples shows irreversible quenching, indicating fast oxidation of the nanoparticles by O<sub>2</sub> with the help of excitation light (< 400 nm wavelength). Moreover, the homogeneity of the luminescence intensity from the patterns is poor. This is because we use a very large ink concentration. Fig. 5.14b shows a topographic IC-AFM image of the same sample (but not at the same position). Due to the high ink concentration, the distribution of nanocomposites on printed regions is inhomogeneous. This is the main reason for the inhomogeneity of the PL patterns. We have not succeeded in obtaining PL images at lower ink concentrations where homogeneous printing (coverage ca. one monolayer) could be fulfilled. Ideally, the excitation wavelength for nanocomposites should be in the near UV region, shorter than 400 nm excitation wavelength (see UV/visible absorption spectra). However, a luminescence microscope with laser source at this wavelength range is not commercially available. A way to increase the PL intensity is increasing the amount of nanocomposites on patterned regions since an increase in PL yield is limited (chapter 4). The best relative PL quantum yield for nanocomposites in our case is lower than 0.15 compared to Coumarin 4 at room temperature. Therefore, a good way to increase the amount of nanocomposites homogeneously is the buildup of three-dimensional structures. Another soft lithography technique: micromolding in capillaries [Xia98] might be a suitable way since the thickness of patterns can be much higher, and since nanocomposites can be better protected by another host matrix from O<sub>2</sub>.

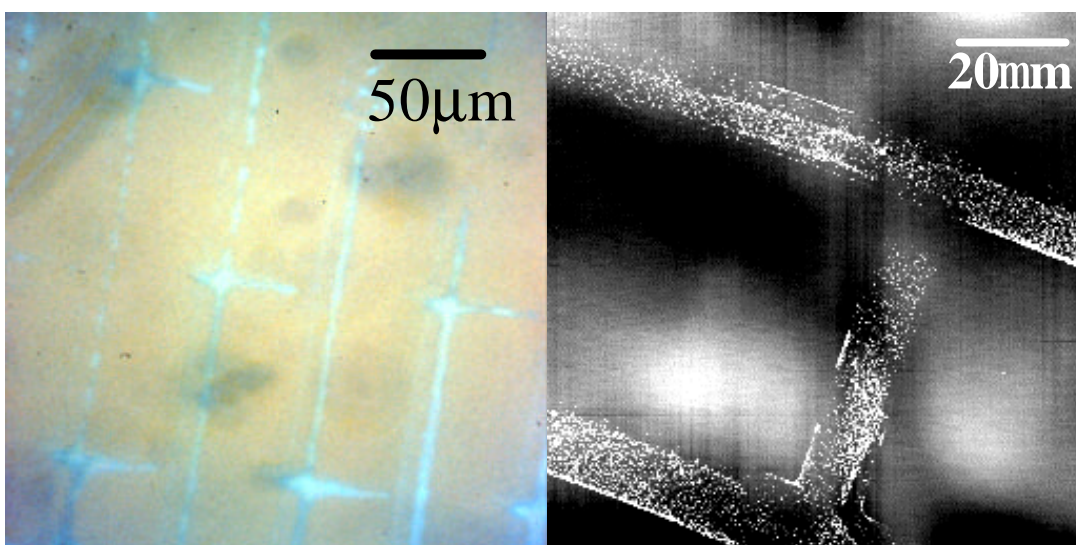


Figure 5.14 Fluorescence image (upper part) and topographic IC-AFM image (lower part) of printed aged CdS/G8NH<sub>2</sub> nanocomposites pattern on a Si wafer

## 5.8 Comparison of direct printing and indirect patterning

Patterning of functional materials is mainly based on the combination of printing passivation layers, followed by solution adsorption of functional materials. A low nonspecific adsorption of functional materials on passivated regions must be guaranteed. From adsorption experiment, we know that CdS/G8NH<sub>2</sub> nanocomposites, especially aged ones, show low selectivity in adsorption (Fig. 5.4f). This will in principle influence the feasibility of indirect patterning processes. For showing this, we first print CH<sub>3</sub>(CH<sub>2</sub>)<sub>17</sub>SH (0.5 mM CH<sub>3</sub>(CH<sub>2</sub>)<sub>17</sub>SH in ethanol) as a passivation layer on Au/Cr/glass. The CdS/G8NH<sub>2</sub> nanocomposites are then adsorbed to the surface.

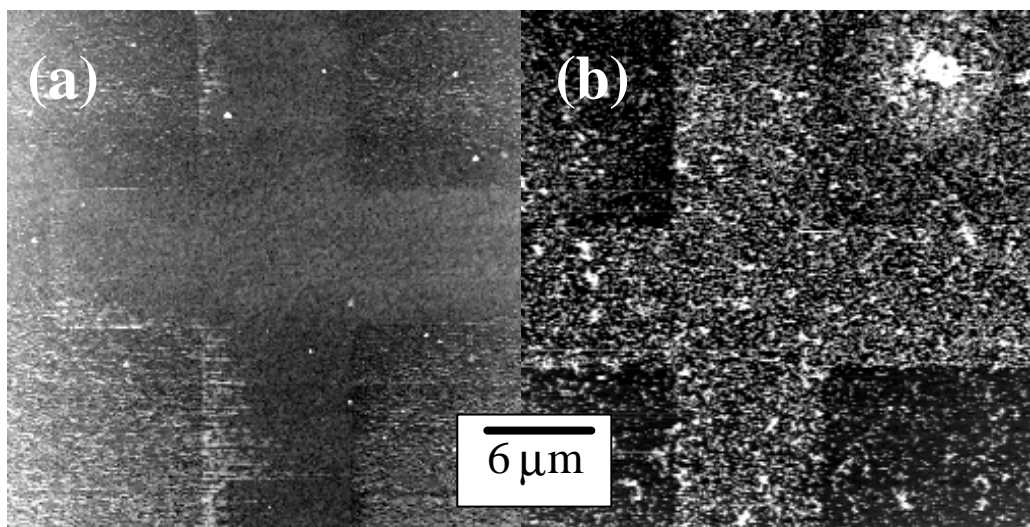


Figure 5.15 Topographic IC-AFM images for (a) printed  $C_{18}H_{37}SH/Au/glass$  patterns and (b) after adsorption of fresh  $CdS/G8NH_2$  nanocomposites.

As shown in Fig. 5.15, a selective adsorption does not occur. In order to guarantee the quality of printed  $CH_3(CH_2)_{17}SH$  passivation layer, we first immerse the printed substrate into air-saturated  $KCN$  aqueous solution for several minutes to etch some  $Au$  away [Delamarche98]. The topographic IC-AFM image in Fig. 5.16a shows no etching of  $Au$  on the printed parts, indicating a good quality of the printed thiol layer. One drop of  $CdS/G8NH_2$  nanocomposites methanolic solution is placed on the substrate for two minutes. Then the substrate is rinsed with ethanol and dried with argon. The topographic IC-AFM image obtained at the same region (see four holes in the middle) is shown in Fig. 5.16b.

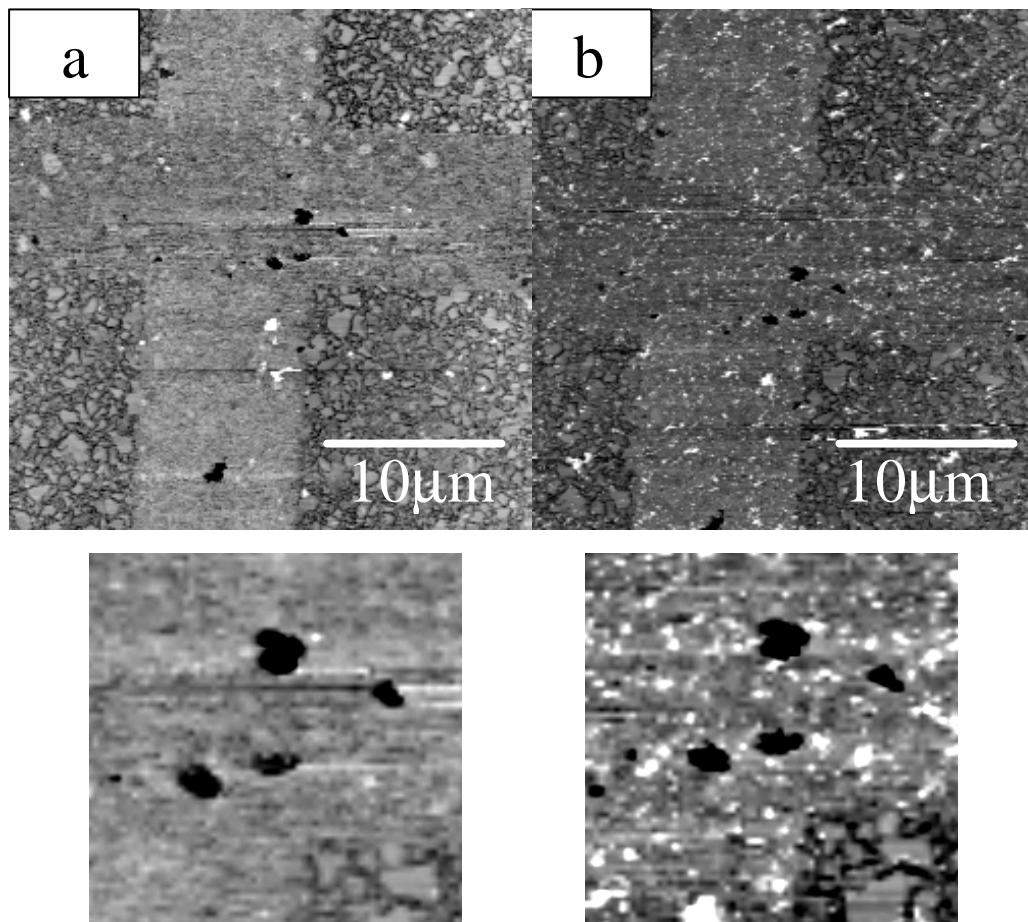


Figure 5.16 Topographic IC-AFM images of printed  $C_{18}H_{37}SH$  single pattern on Au/Cr/Glass substrate after etching of some Au (a) and after adsorption of fresh CdS/G8NH<sub>2</sub> nanocomposites (b).

In Fig. 5.16b, many white dots appear both on printed hydrophobic thiol parts and on unprinted bare Au parts. Zoom-in images at the lower part show this more clearly. We use the four holes at printed thiol parts as marks. Before nanocomposite adsorption, the printed regions are relatively clean. After adsorption, many nanocomposites appear in this region. This indicates that nanocomposites also adsorb on passivation thiol layers. The adsorption of CdS/G8NH<sub>2</sub> nanocomposites on the passivation layer comes from van der Waals forces between nanocomposites and hydrophobic surface. We observe a much

lower adsorption density of nanocomposites on CH<sub>3</sub>-terminated thiol SAMs on Au/mica (solution adsorption) compared to the printed thiols on Au/Cr/glass. The reason might be that the order-degree of printed thiols is worse than that of SAMs via solution adsorption. These experimental results indicate that indirect patterning of this nanocomposite via solution adsorption is problematic.

## 5.9 Conclusion

From the above experimental results, we obtain the following results:

- 1) External type CdS/G8NH<sub>2</sub> nanocomposites show obvious RT growth behavior. It causes morphology changes of the nanocomposites. The changes in morphology further influence the adsorption properties of nanocomposites on the surface.
- 2) Similar to pure dendrimers, these nanocomposites can be directly printed to different surfaces. In addition, due to the combination of nanoparticles with dendrimers, some new morphology features that are different from host dendrimers might appear (here stripe structures). This might provide a new method for spatial organization of both inorganic and organic dendrimers.
- 3) In contrast to direct printing, highly selective adsorption of these nanocomposites to patterned surfaces is problematic.

We have demonstrated the successful direct printing of CdS nanoparticles, protected by dendrimers, on surfaces. As already known, many different nanoparticles have been synthesized using dendrimers as nanoreactors. The printing method we present here therefore suggests a general direct patterning way for those nanocomposites.



## Chapter 6

### Conclusions and Outlook

Apart from solution adsorption, can nanoparticles be patterned on the surface using another simple, general and mild method? Using multi-functionality of poly(amidoamine) (PAMAM) dendrimers in combination with microcontact printing and wet chemical synthesis, our answer is yes. Near-spherical macromolecules, PAMAM dendrimers, are explored here both as chemically selective host molecules and as transfer media. Interactions between metal ions and chemical groups of dendrimers, Pd<sup>2+</sup> and tertiary nitrogen of G4OH and Cd<sup>2+</sup> and primary and tertiary amine groups of G8NH<sub>2</sub>, are exploited here. Two strategies are demonstrated.

In strategy one, pure dendrimers are used as inks and printed on the surface. Metal ions adsorb in dendrimers and are then reduced. In chapter 3 this strategy is explored. OH-terminated generation 4 PAMAM dendrimers (G4OH) are used as inks. Using solution synthesis, Pd/G4OH constitutes a model system because Pd<sup>2+</sup> ions bind to internal tertiary N groups of the G4OH via a strong complexation. One Pd nanoparticle inside one G4OH is thus achieved. On the surface, the binding of Pd<sup>2+</sup> ions to G4OH is similar to the case in the solution; however, the nucleation and growth of Pd nanoparticles are not confined inside one G4OH molecule due to the high density of G4OH molecules on the surface. The size and the morphology of Pd/G4OH nanocomposites synthesized on the surface is different from that prepared in the solution. Despite of this, the Pd nanoparticles directly formed on the surface are catalytically active

and can guide the electroless deposition (ELD) of Co. Sub-micrometer Co patterns with bulk properties (the thickness of Co is over 10 nm) are achieved. The ELD baths need to be further improved in order to obtain better control over the deposition rates.

Due to less effective control of the distribution of dendrimers on the surface by the printing procedure, nanoparticles synthesized on printed dendrimers show a broader size distribution than those synthesized in solution. In order to avoid this, we explore strategy two: first synthesis of nanoparticles in the solution and then printing them on the surface. In addition, instead of synthesis of nanoparticles inside the dendrimer, we synthesize nanoparticles on the surface of the dendrimer. This is explored in chapters 4 and 5.  $\text{NH}_2$ -terminated generation 8 PAMAM dendrimers ( $\text{G8NH}_2$ ) are used. Each synthesized CdS nanoparticle is surrounded by  $\text{G8NH}_2$  molecules. A size-dependent property, here photoluminescence, is demonstrated. Considering the rich chemistry of dendrimers and the achievements in the synthesis of high-quality nanoparticles using wet chemistry, first binding these high-quality nanoparticles onto the surface of dendrimers and then directly printing them on the surface presents a promising way to bring various nanoparticles on the surface. Decreasing the concentration of inks leads to a reduction of the nanocomposite density on the surface. The numbers and the spatial positions of nanoparticles on each pattern are statistically distributed. However, the distribution obtained from direct printing is much more difficult to control compared with the one obtained from solution adsorption. This remains a challenge for this method.

In this thesis, we have demonstrated successful printing of nanocomposites from micrometer to several hundred nanometer using the  $\mu\text{CP}$  technique. Pattern sizes at this range can be relatively easy realized. A big challenge for the  $\mu\text{CP}$  technique is the sub-

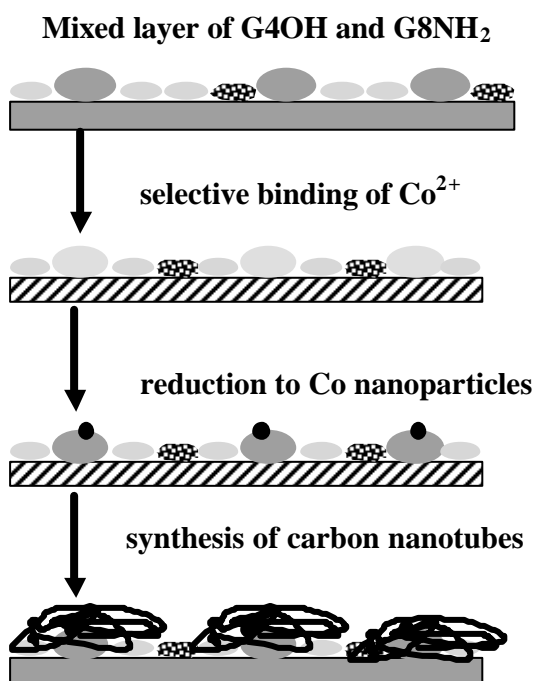


micrometer range. Only a few reports at this range have appeared [Schmid00, Tormen02]. One key issue in this direction is to find suitable stamp materials since often used thermocured siloxane polymer stamp material (Sylgard 184) for  $\mu\text{m}$  range patterns tends to merge or collapse during inking and printing for nm range patterns [Delamarche97].

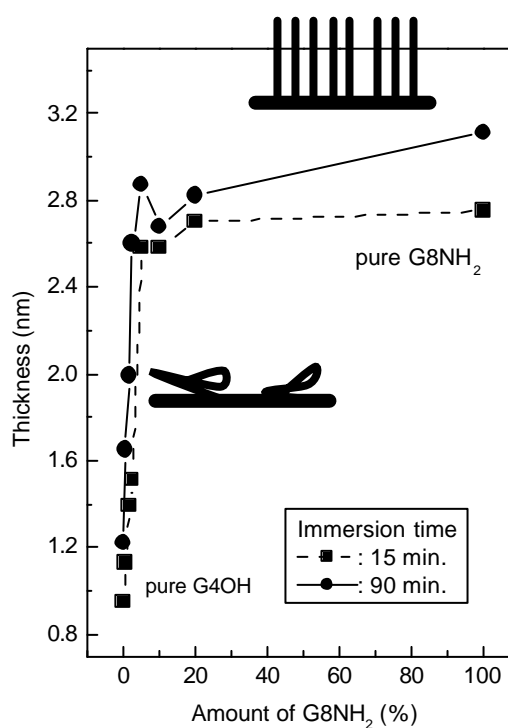
Based on these results, we would like to point out two kinds of perspectives for PAMAM dendrimers. First, we can utilize the difference in binding affinity of chemical groups from dendrimers with metal ions. This can be done via the selection of metal ions, which we will show below, or via a further modification of dendrimer surfaces with highly selective functional groups [Cohen01]. As we know (Fig. 2.13), the binding affinity of tertiary N inside G4OH is much weaker than that of primary N at the surface of  $\text{NH}_2$ -terminated dendrimers. We can therefore use a mixture of G4OH and G4 $\text{NH}_2$  (or G8 $\text{NH}_2$ ) to form mixed layers on surfaces. Co ions will bind selectively to  $\text{NH}_2$ -terminated dendrimers. Co nanoparticles confined within  $\text{NH}_2$ -terminated dendrimers can be obtained and further used as catalyst, for example, for the growth of carbon nanotubes. The process is schematically shown in Fig. 6.1a. In Fig. 6.1b we show the measured variation of ellipsometric thickness of mixed monolayers with the ratio of G4OH to G8 $\text{NH}_2$ . Kind et al. showed that with the change of the concentration of  $\text{Fe}^{3+}$  ions on the surface, the morphology of carbon nanotubes, grown at iron catalyst particles, changes [Kind99]. In the case of dendrimers, this can simply be realized by controlling the relative amount of G8 $\text{NH}_2$  in mixed monolayers, which determines the nucleation sites of Co nanoparticles. At a low density of  $\text{NH}_2$ -terminated dendrimers thus formed nanotubes

might lie flat on the surface, while with pure G4NH<sub>2</sub> or G8NH<sub>2</sub> monolayers the nanotubes might stand up.

The tip convolution with surface features presents a big obstacle to reduce the lateral resolution of AFM. Nanotubes connected with normal tips appear to be a promising way to solve this problem. Copying the growth of carbon nanotubes from flat Si wafers to the apex of a commercial tip might be a simple way to obtain nanotube tips. Due to the simple printing procedure for dendrimers, obtaining nanotubes in a patterned way is also straightforward. Another interesting point is that due to the fixed loading factors of Co<sup>2+</sup> ions to primary N, effects of catalyst size on the growth of nanotubes can be easily traced by changing the dendrimer generation. Nanotubes with narrow size and length distributions might be obtained due to a thus achieved good control of the catalyst size distribution.



(a)



(b)

Figure 6.1a Schematic diagram of the formation of carbon nanotubes via catalysis of Co nanoparticles bound to  $\text{NH}_2$ -terminated dendrimers in a mixed monolayer of G4OH and G8 $\text{NH}_2$ .

Figure 6.1b Ellipsometric thickness of a mixed monolayer of G4OH and G8 $\text{NH}_2$ , obtained at two different adsorption times. The possible morphology of nanotubes is also shown [Wu].

Second, although PAMAM dendrimers are monodisperse, spherical molecules, they are flexible and easily deformed upon attaching to hydrophilic surfaces. This indicates that high-order organization processes by dendrimers themselves cannot be obtained easily. We can classify PAMAM dendrimers as “soft” templates. Some “hard” templates are needed to guide an organization process. Here, we show two ways for the buildup of ordered structures. First, commercially available colloidal spheres can be used as hard templates. They form hexagonal structures on surfaces [Caruso98]. We can copy the formation process of dendrimer multilayers on flat surfaces to the curved surfaces of silica spheres (or modified polystyrene spheres). The desired molecules and nanoparticles are then bound to the dendrimers. The self-assembly properties of hard spheres will lead to the organization of the whole system. Photonic band gap materials with the required refraction index can be achieved. This is shown in Fig. 6.2.

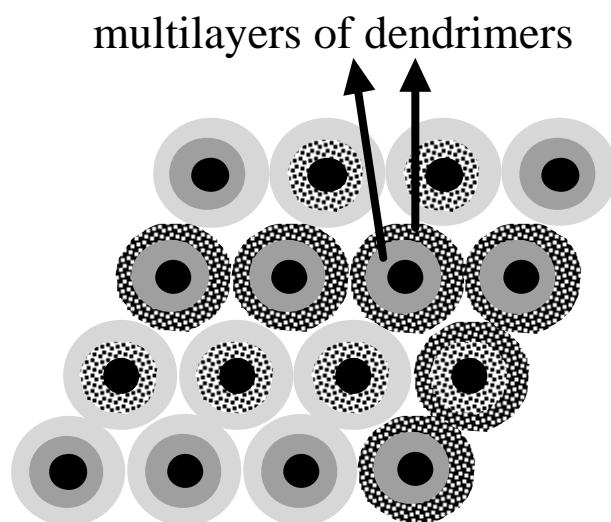


Figure 6.2 Self-assembly of colloidal spheres modified with multilayers of dendrimers

Second, when the interaction between these hard nanoobjects is not strong enough to organize them, guided assembly of high aspect ratio hard objects by external forces such as electromagnetic radiation, electric or magnetic fields can be used. Presently many of such objects, e.g. nanorods (nanowires) [Martin99, LiC02], nanotubes [Muh00], and nanobelts [Law02], have been synthesized, often with a narrow size-distribution (at least in one dimension). Dendrimers can form multilayers, monolayers or adsorb as isolated molecules on these nanorods and nanowires, according to the number of active sites on them, and according to the nature of dendrimers. For example, gold nanowires can be considered as “curved” gold surfaces. Dendrimer multi- and monolayers can form on the surface of these nanowires. With the help of an electric field, these conductive nanowires can align. Patterned electrodes can improve the alignment [Smith00]. This is shown in Fig. 6.3. After alignment, further functional modification on dendrimer parts can be done.

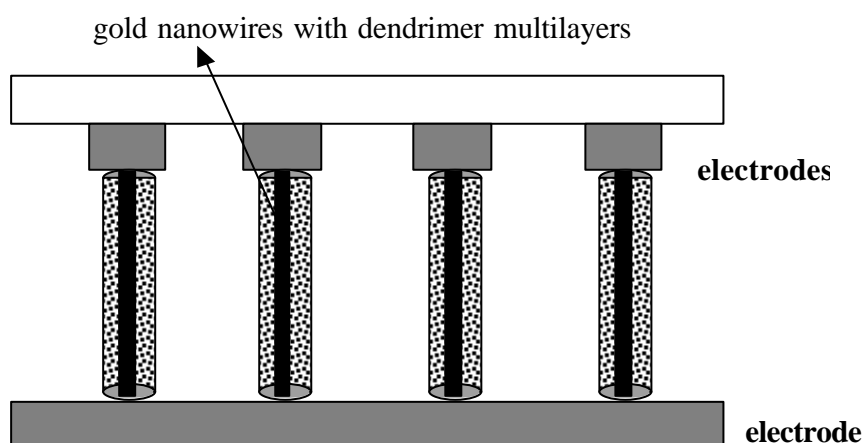


Figure 6.3 Guided alignments of gold nanowires modified with multilayers of dendrimer-based functional materials with the help of an external electric field.

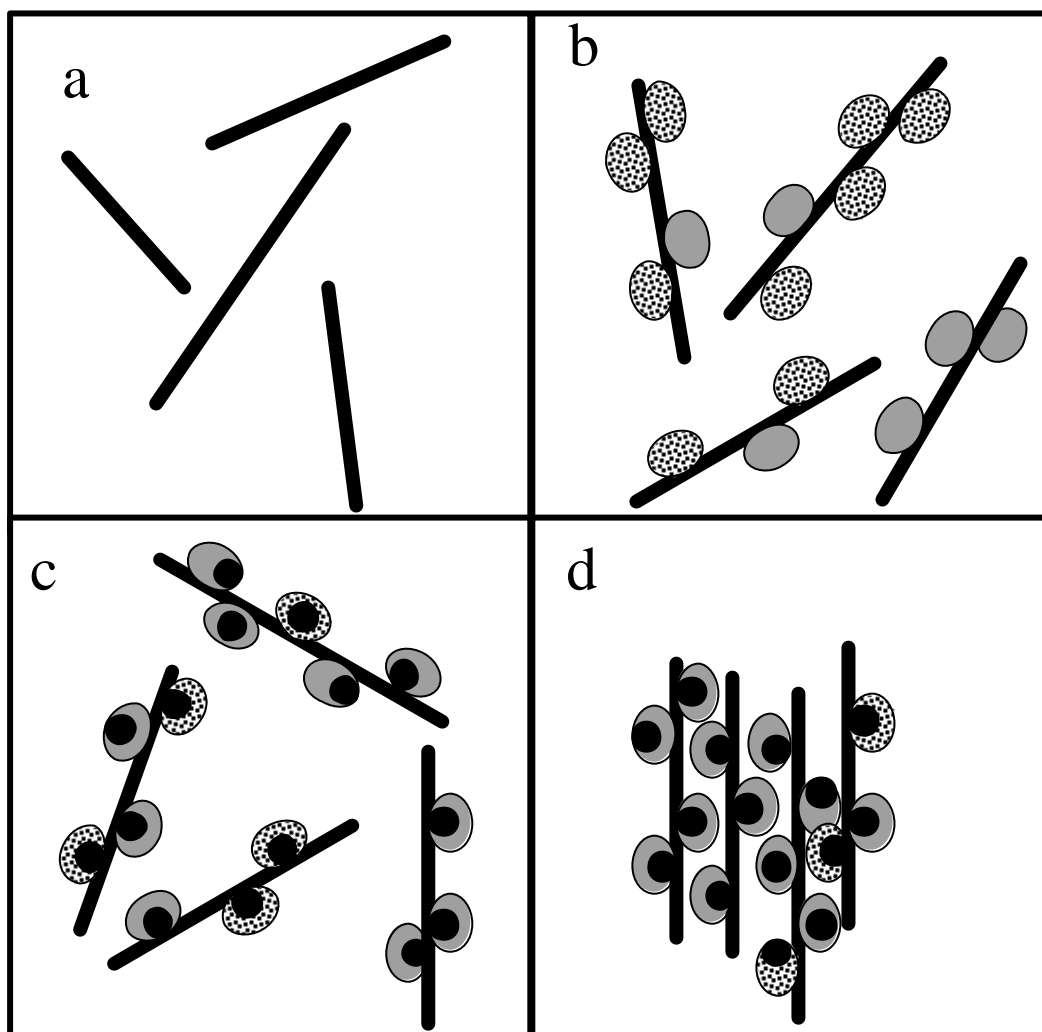


Fig. 6.4 Guided alignment of modified carbon nanotubes with the help of an external field. (a) dispersed carbon nanotube suspension after acid treatment, (b) modification with dendrimers via electrostatic forces or covalent binding, (c) formation of magnetic nanoparticles, (d) alignment of nanotubes on a surface under a magnetic field.

For carbon nanotubes, the numbers of carboxylate groups on the surface can be controlled by the degree of oxidation (e.g. by oxidative acids) [Hirsch02].  $\text{NH}_2$ -

terminated dendrimers can attach to those sites by either electrostatic forces or covalent binding. Introducing magnetic particles will guide the organization of magnetized carbon nanotubes on substrates under the help of an external magnetic field. This process is shown in Fig. 6.4. After the alignment further modification is possible. For example, an oxygen plasma can remove the dendrimers. An acid treatment can remove the magnetic particles without damage of the aligned structures. If the distance between two nanotube neighbors is given by the diameter of the dendrimers, an only several nanometer wide gap will form between two nanotubes. Such structures are e.g. desirable to study electric properties of single molecules.

## References:

- [Allan93] J. R. Allan, P. C. Beaumont, G. H. W. Milburn, I. Wood, *Thermochimica Acta* 214, 243 (1993)
- [Balogh98] L. Balogh, D. A. Tomalia, *J. Am. Chem. Soc.* 120, 7355 (1998)
- [Balogh99] L. Balogh, R. Valluzzi, K. S. Laverdure, S. P. Gido, G. L. Hagnauer, D. A. Tomalia, *J. Nanoparticle Research* 1, 353 (1999)
- [Bawendi90] M. G. Bawendi, M. L. Steigerwald, L. E. Brus. *Annu. Rev. Phys. Chem.* 41, 477 (1990)
- [Bernard00] A. Bernard, J. P. Renault, B. Michel, H. R. Bosshard, E. Delamarche, *Adv. Mater.* 12, 1067 (2000)
- [Betley01] T. A. Betley, M. M. B. Holl, B. G. Orr, D. R. Swanson, D. A. Tomalia, J. R. Baker, Jr. *Langmuir* 17, 2768 (2001)
- [Binnig86] G. Binnig, C. F. Quate, C. Gerber, *Phys. Rev. Lett.* 56, 930 (1986)
- [Bittner02] A. M. Bittner, X. C. Wu, K. Kern, *Adv. Funct. Mater.* 12, 432 (2002)
- [Braun98] E. Braun, Y. Eichen, U. Sivan, G. Ben-Yoseph, *Nature* 391, 775 (1998)
- [Braun01] M. Braun, C. Burda, M. Mohamed, M. El-Sayed, *Phys. Rev. B* 64, 035317 (2001)
- [Brune98] H. Brune, M. Giovannini, K. Bromann, K. Kern, *Nature* 394, 451 (1998)
- [Buhleier78] E. Buhleier, W. Wehner, F. Voegtle, *Synthesis* 78, 155 (1978)
- [Carrot99] G. Carrot, S. M. Scholz, C. J. G. Lummer, J. G. Hilborn, J. L. Hedrick, *Chem. Mater.* 11, 3571 (1999)
- [Caruso98] F. Caruso, R. A. Caruso, H. Moehwald, *Science*, 282, 1111 (1998)

- [Carvalho02] A. Carvalho, M. Geissler, H. Schmid, B. Michel, E. Delamarche, *Langmuir*, 18, 2406 (2002)
- [Chechik99] V. Chechik, M. Q. Zhao, R. M. Crooks, *J. Am. Chem. Soc.* 121, 4910 (1999)
- [Chan02] E. W. L. Chen, L. Yu, *Langmuir*, 18, 311 (2002)
- [Chou96] S. Y. Chou, P. R. Krauss, P. J. Renstrom, *Science* 272, 85 (1996)
- [Cizeron97] J. Cizeron, M. P. Pileni, *J. Phys. Chem. B* 101, 8887 (1997)
- [Cohen01] S. M. Cohen, S. Petoud, K. N. Raymond, *Chem. Eur. J.* 7, 272 (2001)
- [Crooks00] R. M. Crooks, M. Zhao, L. Sun, V. Chechik, L. K. Yeung, *Acc. Chem. Res.*, 34, 181 (2000)
- [Crooks01] R. M. Crooks, B. I. Lemon, L. Sun, L. K. Yeung, M. Zhao, "Dendrimer-Encapsulated Metals and Semiconductors: Synthesis, Characterization, and Applications", *Topics in Current Chemistry*, Vol. 212, Springer-Verlag, Berlin Heidelberg, 2001, pp.81-135.
- [Dai98] H. Dai, J. H. Hafner, A. G. Rinzler, D. T. Colbert, R. E. Smalley, *Nature* 384, 147 (1996)
- [Delamarche97] E. Delamarche, H. Schmid, B. Michel, H. Biebuyck, *Adv. Mater.* 9, 741 (1997)
- [Delamarche98] E. Delamarche, H. Schmid, A. Bietsch, N. B. Larsen, H. Rothuizen, B. Michel, H. Biebuyck, *J. Phys. Chem. B* 102, 3324 (1998)
- [Douglas98] T. Douglas, M. Young, *Nature* 393, 152 (1998)
- [Dressick94] W. J. Dressick, C. S. Dulcey, J. H. Georger, G. S. Calabrese, J. M. Calvert, *J. Electrochem. Soc.* 141, 210 (1994)



- [Duijvenbode98] R. C. van Duijvenbode, M. Borkovec, G. J. M. Koper, *Polymer* 39, 2657 (1998)
- [Erhardt01] M. K. Erhardt, R. G. Nuzzo, *J. Phys. Chem. B* 105, 8776 (2001)
- [Esumi98] K. Esumi, A. Suzuki, N. Aihara, K. Usui, K. Torigoe, *Langmuir* 14, 3157 (1998)
- [Esumi01] K. Esumi, K. Satoh, K. Torigoe, *Langmuir* 17, 6860 (1998)
- [Fail02] C. A. Fail, S. A. Evenson, L. J. Ward, W. C. E. Schofield, J. P. S. Badyal, *Langmuir*, 18, 264 (2002)
- [Finnie00] K. R. Finnie, R. Haasch, R. G. Nuzzo, *Langmuir* 16, 6968 (2000)
- [Finot97] M. O. Finot, M. T. McDermott, *J. Am. Chem. Soc.* 119, 8564 (1997)
- [Fischer99] M. Fischer, F. Voegtle, *Angew. Chem. Int. Ed.* 38, 884 (1999)
- [Fogg97] D. E. Fogg, L. H. Radzilowski, B. O. Dabbousi, R. R. Schrock, E. L. Thomas, M. G. Bawendi, *Macromolecules* 30, 8433 (1997)
- [Gaponenko98] S. V. Gaponenko, *Optical Properties of Semiconductor Nanocrystals*, Cambridge University Press, 1998, Pg. 53.
- [Gaponik02] N. Gaponik, D. V. Talapin, A. L. Rogach, K. Hoppe, E. V. Shevchenko, A. Kornowski, A. Eychmueller, H. Weller, *J. Phys. Chem. B* 106, 7177 (2002)
- [Garcia99] M. E. Garcia, L. A. Baker, R. M. Crooks, *Anal. Chem.* 71, 256 (1999)
- [Geissler00] M. Geissler, A. Bernard, A. Bietsch, H. Schmid, B. Michel, E. Delamarche, *J. Am. Chem. Soc.* 122, 6303 (2000)
- [Gorman97] C. B. Gorman, B. L. Parkhurst, W. Y. Su, K. Y. Chen, *J. Am. Chem. Soc.* 119, 1141 (1997)

- [Groehn00] F. Groehn, B. J. Bauer, Y. A. Akpalu, C. L. Jackson, E. J. Amis, *Macromolecules* 33, 6042 (2000)
- [Gu01] G. Gu, G. Philipp, X. C. Wu, M. Burghard, A. M. Bittner, S. Roth, *Adv. Funct. Mater.* 11, 295 (2001)
- [Guilbault72] G. G. Guilbault, S. M. Billedeau, *J. Inorg. Nucl. Chem.* 34, 1167 (1972)
- [Ha00] K. Ha, Y. Lee, D. Jung, J. Lee, K. Yoon, *Adv. Mater.* 12, 1614 (2000)
- [Haesselbarth93] A. Haesselbarth, A. Eychmueller, R. Eichberger, M. Giersig, A. Mews, H. Weller, *J. Phys. Chem.* 97, 5333 (1993)
- [Harada01] Y. Harada, X. Li, P. W. Bohn, R. G. Nuzzo, R. G. *J. Am. Chem. Soc.* 123, 8709 (2001)
- [He00] H. X. He, H. Zhang, Q. G. Li, T. Zhu, S. F.Y. Li, Z. F. Liu, *Langmuir* 16, 3846 (2000)
- [Henglein88] A. Henglein, *Top. Curr. Chem.* 143, 113 (1988)
- [Hidber96] P. C. Hidber, P. F. Nealey, W. Helbig, G. M. Whitesides, *Langmuir* 12, 5209 (1996)
- [Hierlemann98] A. Hierlemann, J. K. Campbell, L. A. Baker, R. M. Crooks, A. J. Ricco, *J. Am. Chem. Soc.* 120, 5323 (1998)
- [Hirsch02] A. Hirsch, *Angew. Chem. Int. Ed.* 41, 1853 (2002)
- [Hines96] M. A. Hines, P. Guyot-Sionnest, *J. Phys. Chem.* 100, 468 (1996)
- [Huang99] J. M. Huang, K. Sooklal, C. J. Murphy, H. J. Ploehn, *Chem. Mater.* 11, 3595 (1999)
- [Hyun01] J. Hyun, Y. Zhu, A. Liebmann-Vinson, T. P. Beebe, A. Chilkoti, *Langmuir* 17, 6358 (2001)

- [Jeon97] N. L. Jeon, K. Finnie, K. Branshaw, and R. G. Nuzzo, *Langmuir* 13, 3382 (1997)
- [John96] P. M. St. John, H. G. Craighead, *Appl. Phys. Lett.* 68, 1022 (1996)
- [Kern91] K. Kern, H. Niehus, A. Schatz, P. Zeppenfeld, J. George, G. Comsa, *Phys. Rev. Lett.* 67, 855 (1991)
- [Knez02] M. Knez, M. Sumser, A. Bittner, Ch. Wege, H. Jeske, S. Kooi, M. Burghard, K. Kern, *J. of Electroanalyt. Chem.* 522, 70 (2002)
- [Kind98] H. Kind, A. M. Bittner, O. Cavalleri, T. Greber, K. Kern, K. *J. Phys. Chem. B* 102, 7582 (1998)
- [Kind99] H. Kind, J. M. Bonard, C. Emmenegger, L. O. Nilsson, K. Hernadi, E. Maillard-Schaller, L. Schlapbach, L. Forro, K. Kern, *Adv. Mater.* 11,1285 (1999)
- [Kind00a] H. Kind, J. M. Bonard, L. Forro, K. Kern, K. Hernadi, L. O. Nilsson, L. Schlapbach, *Langmuir* 16, 6877 (2000)
- [Kind00b] H. Kind, H. M. Geissler, H. Schmid, B. Michel, K. Kern, E. Delamarque, *Langmuir* 19, 6367 (2000)
- [Koide00] Y. Koide, Q. Wang, J. Cui, D. D. Benson, T. J. Marks, *J. Am. Chem. Soc.* 122, 11266 (2000)
- [Koper97] G. J. M. Koper, M. H. P. van Genderen, C. Elissen-Roman, M. W. P. L. Baars, E. W. Meijer, M. Borkovec, *J. Am. Chem. Soc.* 119, 6512 (1997)
- [Kumar93] A. Kumar, G. M. Whitesides, *Appl. Phys. Lett.* 63, 2002 (1993)
- [Kumar01] A. Kumar, S. Mital, *J. Colloid and Interface Science* 240, 459 (2001)
- [Lackowski99] W. M. Lackowski, J. K. Campbell, G. Edwards, V. Checkik, R. M. Crooks, *Langmuir* 15, 7632 (1999)

- [Lahiri99] J. Lahiri, E. Ostuni, G. M. Whitesides, *Langmuir*, 15, 2055 (1999)
- [Lakowicz99] J. R. Lakowicz, I. Gryczynski, Z. Gryczynski, C. J. Murphy, *J. Phys. Chem. B* 103, 7613 (1999)
- [Law02] M. Law, H. Kind, B. Messer, F. Kim, P. D. Yang, *Angew. Chem. Int. Ed.* 41, 2405 (2002)
- [Legrand01] J. Legrand, A. Ngo, C. Petit, M. Pileni, *Adv. Mater.* 13, 58 (2001)
- [Lemon00] B. I. Lemon, R. M. Crooks, *J. Am. Chem. Soc.* 122, 12886 (2000)
- [Li00] J. Li, T. Piehler, D. Qin, J. R. Baker, D. A. Tomalia, *Langmuir* 16, 5613 (2000)
- [LiC02] C.P. Li, N. Wang, S.P. Wong, C.S. Lee, S.T. Lee, *Adv. Mater.* 14, 218 (2002)
- [LiH02] H. W. Li, D. J. Kang, M. G. Blamire, W. T. S. Huck, *Nano Lett.* 2, 347 (2002)
- [Libiouille99] L. Libiouille, A. Bietsch, H. Schmid, B. Michel and E. Delamarche, *Langmuir*, 15, 300 (1999)
- [Mallory90] *Electroless Plating: Fundamentals & Applications*, G. O. Mallory, J. B. Hajdu, Eds.; American Electroplaters and Surface Finishers Society: Orlando, FL, 1990.
- [Maoz99] R. Maoz, S. R. Cohen, J. Sagiv, *Adv. Mater.* 11, 55 (2000)
- [Maoz00a] R. Maoz, E. Frydman, S. R. Cohen, J. Sagiv, *Adv. Mater.* 12, 424 (2000)
- [Maoz00b] R. Maoz, E. Frydman, S. R. Cohen, J. Sagiv, *Adv. Mater.* 12, 725 (2000)
- [Martin99] B. R. Martin, D. J. Dermody, B. D. Reiss, M. Fang, L. A. Lyon, M. J. Natan, T. E. Mallouk, *Adv. Mater.* 12, 1021 (1999)
- [Markovich99] G. Markovich, C. P. Collier, S. E. Henrichs, F. Remacle, R. D. Levine, J. R. Heath, *Acc. Chem. Res.* 32, 415 (1999)
- [Martin02] J. E. Martin, J. P. Wilcoxon, J. Odinek, P. Provencio, *J. Phys. Chem. B* 106, 971 (2002)

- [Massey01] J. A. Masey, M. A. Winnik, I. Manners, V. Z.-H. Chan, J. M. Ostermann, R. Enchelmaier, J. P. Spatz, M. Moeller, *J. Am. Chem. Soc.* 123, 3147 (2001)
- [Mertig98] M. Mertig, R. Kirsch, W. Pompe, *Appl. Phys. A* 66, S723 (1998)
- [Mews94] A. Mews, A. Eychmueller, M. Giersig, D. Schooss, H. Weller, *J. Phys. Chem.* 98, 934 (1994)
- [Mews96] A. Mews, A. V. Kadavanich, U. Banin, A. P. Alivisatos, *Phys. Rev. B* 53, R13242 (1996)
- [Muhr00] H. Muhr, F. Krumeich, Urs P. Schoenhdzen, F. Bieri, M. Niederberger, L. J. Gaucker, R. Nesper, *Adv. Mater.* 12, 231 (2000)
- [Murakoshi00] K. Murakoshi, Y. Nakato, *Adv. Mater.* 12, 791 (2000)
- [Murray93] C. B. Murray, D. J. Norris, M. G. Bawendi, *J. Am. Chem. Soc.* 115, 8706 (1993)
- [Murray95] C. B. Murray, C. R. Kagan, M. G. Bawendi, *Science* 270,1335 (1995)
- [Murray00] C. B. Murray, C. R. Kagan, M. G. Bawendi, *Annu. Rev. Mater. Sci.* 30, 545 (2000)
- [Nethercot74] A. H. Nethercot, Jr. *Phys. Rev. Lett.* 33, 1088 (1974)
- [Ottaviani97] M. F. Ottaviani, F. Montalti, N. J. Turro, D. A. Tomalia, *J. Phys. Chem. B* 101, 158 (1997)
- [Peng97] X. G. Peng, M. C. Schlamp, A. V. Kadavanich, A. P. Alivisatos, *J. Am. Chem. Soc.* 119, 7019 (1997)
- [Peng98] X. G. Peng, J. Wickham, A. P. Alivisatos, *J. Am. Chem. Soc.* 120, 5343 (1998)
- [PengZ01] Z. A. Peng, X. G. Peng, *J. Am. Chem. Soc.* 123, 183 (2001)
- [PengZ02] Z. A. Peng, X. G. Peng, *J. Am. Chem. Soc.* 124, 3343 (2002)

- [Pileni00] M. P. Pileni, *Catalysis Today*, 58, 151 (2000)
- [Piner99] R. D. Piner, J. Zhu, F. Xu, S. Hong, C. A. Mirkin, *Science* 283, 661 (1999)
- [Pompe99] T. Pompe, A. Fery, S. Herminghaus, A. Kriele, H. Lorenz, J. P. Kotthaus, *Langmuir* 15, 2398 (1999).
- [Putten93] A. M. T. van der Putten, J. W. G. de Bakker, *J. Electrochem. Soc.* 140, 2229 (1993)
- [Qin99] D. Qin, Y. Xia, B. Xu, H. Yang, C. Zhu, G. M. Whitesides, *Adv. Mater.* 11, 1433 (1999)
- [Qu02] L. H. Qu, X. G. Peng, *J. Am. Chem. Soc.* 124, 2049 (2002)
- [Ralph78] J. E. Ralph, *Solid State Commun.* 28, 377 (1978)
- [Reiss51] H. Reiss, *J. Chem. Phys.* 19, 482 (1951)
- [Repain02] V. Repain, G. Baudot, H. Ellmer, S. Rousset, *Europhys. Lett.* 58, 730 (2002)
- [Rogach00] A. L. Rogach, A. S. Susha, F. Caruso, G. B. Sukhorukov, A. Kornowski, S. Kershaw, H. Moehwald, A. Eychmueller, H. Weller, *Adv. Mater.* 12, 333 (2000)
- [Schmelz01] O. Schmelz, A. Mews, T. Basche, A. Herrmann, K. Muellen, *Langmuir* 17, 2861 (2001)
- [Schmid92] G. Schmid, *Chem Rev.* 92, 1709 (1992)
- [Schmid00] H. Schmid, B. Michel, *Macromolecules* 33, 3042 (2000)
- [Schmucki98] P. Schmucki, L. E. Erickson, D. J. Lockwood, *Phys. Rev. Lett.* 80, 4060 (1998)
- [Schoer97] J. K. Schoer, R. M. Crooks, *Langmuir* 13, 2323 (1997)
- [Sheiko96] S. S. Sheiko, G. Eckert, G. Ignat`eva, A. M. Muzafarov, J. Spickermann, H. J. Raeder, M. Moeller, *Macromol. Rapid Commun.* 17, 283 (1996)

- [Shenton98] W. Shenton, D. Pum, U. B. Sleytr, S. Mann, *Nature* 389, 585 (1998)
- [Sirota01] M. Sirota, E. MinKin, E. Lifshitz, V. Hensel, M. Lahav, *J. Phys. Chem. B* 105, 6792 (2001)
- [Smith00] P. A. Simth, C. D. Nordquist, T. N. Jackson, T. S. Mayer, B. R. Martin, J. Mibindyo, T. E. Mallouk, *Appl. Phys. Lett.* 77, 1399 (2000)
- [Sooklal98] K. Sooklal, L. H. Hanus, H. J. Ploehn, C. J. Murphy, *Adv. Mater.* 10, 1083 (1998)
- [Spanhel87] L. Spanhel, M. Hasse, H. Weller, A. Henglein, *J. Am. Chem. Soc.* 109, 5649 (1987)
- [Stiriba02] S. E. Stiriba, H. Frey, R. Haag, *Angew. Chem. Int. Ed.* 41, 1329 (2002)
- [Strable01] E. Strable, J. M. Bulte, B. Moskowitz, K. Vivekanandan, M. Allen, T. Douglas, *Chem. Mater.* 13, 2201 (2001)
- [Sun99] S. Sun, C. B. Murray, *J. Appl. Phys.* 85, 43259 (1999)
- [Takano99] H. Takano, J. R. Kenseth, S. Wong, J. C. O'Brien, M. D. Porter, *Chem. Rev.* 99, 2845 (1999)
- [Tan99] N. C. B. Tan, L. Balogh, S. F. Trevino, D. A. Tomalia, J. S. Lin, *Polymer* 40, 2537 (1999)
- [Tokuhisa98] H. Tokuhisa, M. Q. Zhao, L. A. Baker, V. T. Phan, D. L. Dermody, M. E. Garcia, R. F. Pez, R. M. Crooks, T. M. Mayer, *J. Am. Chem. Soc.* 120, 4492 (1998)
- [Tomoyose96] Y. Tomoyose, D. Jiang, R. Jin, T. Aida, T. Yamashita, K. Horie, E. Yashima, Y. Okamoto, *Macromolecules* 29, 5236 (1996)
- [Torigoe01] K. Torigoe, A. Suzuki, K. Esumi, *J. Colloid and Interface Science* 241, 346 (2001)

- [Tormen02] M. Tormen, T. Borzenko, B. Steffen, G. Schmidt, L. W. Molenkamp, *App. Phys. Lett.* 81, 2094 (2002)
- [Tsukruk97] V. V. Tsukruk, F. Rinderspacher, V. N. Bliznyuk, *Langmuir* 13, 2171 (1997)
- [Tully99] D. C. Tully, K. Wilder, J. M. J. Frechet, A. R. Trimble, C. F. Quate, *Adv. Mater.* 11, 314 (1999)
- [Uppuluri00] S. Uppuluri, D. R. Swanson, L. T. Piehler, J. Li, G. L. Hagnauer, D. A. Tomalia, *Adv. Mater.* 12, 796 (2000)
- [Vettiger00] P. Vettiger, M. Despont, U. Drechsler, U. Buerig, W. Haeberle, M. I. Lutwyche, H. E. Rothuizen, R. Stutz, R. Widmer, G. K. Binnig, *IBM J. Res. Develop.* 44, 323 (2000)
- [Vossmeier94] T. Vossmeier, L. Katsikas, M. Giersig, I. G. Popovic, K. Diesner, A. Chemseddine, A. Eychmueller, H. Weller, *J. Phys. Chem.* 98, 7665 (1994)
- [Vossmeier97] T. Vossmeier, E. DeIonno, J. R. Heath, *Angew. Chem. Int. Ed.* 36, 1080 (1997)
- [Vossmeier98] T. Vossmeier, S. Jia, E. Delono, M. R. Diehl, S. H. Kim, X. Peng, A. P. Alivisatos, J. R. Heath, *J. Appl. Phys.* 84, 3664 (1998)
- [Walheim99] S. Walheim, R. Mueller, M. Sprenger, E. Loser, J. Mlynek, U. Steiner, *Adv. Mater.* 11, 1431(1999)
- [Wang96] D. Wang, S. G. Thomas, K. L. Wang, Y. Xia, G. M. Whitesides, *Appl. Phys. Lett.* 68, 1022 (1996)
- [WangQ02] Q. Wang, T. Lin, L. Tang, J.E. Johnson, M.G. Finn, *Angew.Chem.Int.Ed.* 41, 459 (2002)



- [Wang02] Y. A. Wang, J. J. Li, H. Chen, X. G. Peng, *J. Am. Chem. Soc.* 124, 2293 (2002)
- [Wong98a] S. S. Wong, A. T. Woolley, E. Joselevich, C. L. Cheung, C. M. Lieber, *J. Am. Chem. Soc.* 120, 603 (1998)
- [Wong98b] S. S. Wong, A. T. Woolley, E. Joselevich, C. L. Cheung, C. M. Lieber, *Nature* 394, 52 (1998)
- [Wu02] X. C. Wu, A. M. Bittner, K. Kern, *Langmuir*, 18, 4984 (2002)
- [Xia95] Y. Xia, M. Mrksich, E. Kim and G. M. Whitesides, *J. Am. Chem. Soc.* 117, 9576 (1995)
- [Xia96] Y. Xia, G. M. Whitesides, *J. Am. Chem. Soc.* 117, 3274 (1996)
- [Xia98] Y. Xia, G. M. Whitesides, *Angew. Chem. Int. Ed.* 37, 550 (1998)
- [Yan98] L. Yan, M. Zhao, G. M. Whitesides, *J. Am. Chem. Soc.* 120, 6179 (1998)
- [Yang00] Z. Yang, A. Chilkoti, *Adv. Mater.* 12, 413 (2000)
- [Youn88] H. C. Youn, S. Baral, J. H. Fendler, *J. Phys. Chem.* 92, 6320 (1988).
- [Yu02] W. W. Yu, X. G. Peng, *Angew. Chem. Int. Ed.* 41, 2368 (2002)
- [Zeng97] F. Zeng, S. C. Zimmerman, *Chem. Rev.* 97, 1681 (1997)
- [Zhang02] H. Zhang, P. C. M. Grim, D. Liu, T. Vosch, S. De Feyter, U. M. Wiesler, A. J. Berresheim, K. Muellen, C. V. Haesendock, N. Vandamme, F. C. De Schryver, *Langmuir* 18, 1801 (2002)
- [Zhao98] M. Q. Zhao, S. Sun, R. M. Crooks, *J. Am. Chem. Soc.* 120, 4877 (1998)
- [Zhao99a] M. Q. Zhao, R. M. Crooks, *Angew. Chem. Int. Ed.* 38, 364 (1999)
- [Zhao99b] M. Q. Zhao, R. M. Crooks, *Chem. Mater.* 11, 3379 (1999)
- [Zhao99c] M. Q. Zhao and R. M. Crooks, *Adv. Mater.* 11, 217 (1999)

[ZhaoH01] H. Zhao, E. P. Douglas, B. S. Harrison, K. S. Schanze, *Langmuir*, 17, 8428 (2001)

[Zheng02] J. Zheng, M. S. Stevenson, R. S. Hikida, P. V. van Patten, *J. Phys. Chem. B* 106, 1252 (2002)

[Zhou93] H. S. Zhou, I. Honma, H. Komiyama, J. W. Haus, *J. Phys. Chem.* 97, 895 (1993)

## Publications

Publications related to this thesis is as follows:

- (1) G. Gu, G. Philipp, **X. C. Wu**, M. Burghard, A.M. Bittner, and S. Roth, "Growth of single-walled carbon nanotubes from microcontact-printed catalyst patterns on thin  $\text{Si}_3\text{N}_4$  membranes." *Adv. Funct. Mater.* 11, 295 (2001).
- (2) **X. C. Wu**, A. M. Bittner, K. Kern, " Spatially Selective Electroless Deposition of Cobalt on Oxide Surfaces Directed by Microcontact Printing of Dendrimers." *Langmuir*, 18, 4984 (2002).
- (3) A. M. Bittner, **X. C. Wu**, K. Kern, "Electroless Metallization of Dendrimer-Coated Micropatterns." *Adv. Funct. Mater.* 12, 432 (2002).
- (4) **X. C. Wu**, A. M. Bittner, K. Kern, "Direct Patterning of Photoluminescent CdS/Dendrimer Nanocomposites on Hydroxyl-terminated Oxide Surfaces via Microcontact Printing." in preparation.
- (5) **X. C. Wu**, A. M. Bittner, K. Kern, "Synthesis, Morphology and Patterning of CdS/Dendrimer Nanocomposites." in preparation.
- (6) **X. C. Wu**, A. M. Bittner, K. Kern, "Synthesis and Patterning of Co Nanocomposites." in preparation.

## Merci

First, I would like to thank Prof. Klaus Kern for bringing me to this fascinating research field. It locates at the crosspoint between the basic research and the modern nanotechnology. In addition, due to the wide research field of Prof. Kern, I have also learned many different things during my stay here.

Second, I want to thank Dr. Bittner for a lot of useful discussions, especially for correcting the English of this dissertation. Special thanks also go to Mato Knez, Alpan Bek for many useful communications and help. I also want to thank Andreas Christ for time-resolved photoluminescence measurements. Thanks to Prof. Kuhl for useful discussions about time-resolved photoluminescence measurements. Thanks also to all members of our group. It is like a big warm family.

IBM Zürich and IMS Stuttgart are kindly appreciated for supplying masters. The DFG and the Max-Planck Institut fuer Festkorperforschung are appreciated for financial support. Thanks also to Prof. Habermeier's group for allowing me to use their SEM machine and Au sample preparation, to Dr. Kind for showing me  $\mu$ CP procedures, to Mato Knez and Dr. Z. L. Zhang for TEM measurements of Pd/G4OH nanoparticles and CdS/G8NH<sub>2</sub> nanoparticles, and to Dr. Christina Wege for allowing me to use their luminescence microscope.

At last, I want to thank my family for their love and support. I want to give this dissertation as a special two-year birthday gift for my little son, Xuefei. I owe him so much and he gives me so many happy times.

## Curriculum Vitae

Name: Xiaochun WU

Date of Birth: Feb. 6, 1968

From 1985 to 1989: Chemistry Department, Sichuan University, Chengdu, P. R. China.  
B. S. in Science, July 1989.

From 1989 to 1992: Environmental Science Department, Jilin University, Changchun, P. R. China. M.S. in Science, July 1992.

From 1992 to 1995: Institute of Modern Optics, Nankai University, Tianjin, P. R. China.

From July 1995 to September 1997: Institute of Physics, Chinese Academy of Sciences, Beijing, P. R. China.

From October 1997 to January 1998: Department of Chemistry, National University of Singapore, Singapore.

From January 1998 to August 1999: Institut für Chemie Anorganischer Materialien, Technische Universität München, München, Germany

From September 1999 to 2002: Nanoscale Science Department (Prof. K. Kern), Max-Planck-Institut fuer Festkoerperforschung, Stuttgart, Germany.